Mechanics of cellulose nanopapers

SUBMITTED IN PARTIAL FULFILLMENT OF THE REQUIREMENTS
OF THE DEGREE OF DOCTOR OF PHILOSOPHY

August 2016

Rui Mao

School of Engineering and Materials Science

Queen Mary University of London

Mile End Road, London, E1 4NS

Declaration

I, Rui Mao, confirm that the research included within this thesis is my own work or that where it has been carried out in collaboration with, or supported by others, that this is duly acknowledged below and my contribution indicated. Previously published material is also acknowledged below.

I attest that I have exercised reasonable care to ensure that the work is original, and does not to the best of my knowledge break any UK law, infringe any third party's copyright or other Intellectual Property Right, or contain any confidential material.

I accept that the College has the right to use plagiarism detection software to check the electronic version of the thesis.

I confirm that this thesis has not been previously submitted for the award of a degree by this or any other university.

Signature: Rui Mao

Date: 20/08/2016

Abstract

Cellulose nanopaper is a fibrous network composed of cellulose nanofibres connected by hydrogen bonds, which shows pronounced mechanical and physical properties. This thesis investigates the mechanics of cellulose nanopaper from various aspects.

First, the fracture properties of cellulose nanopaper were investigated using experimental and modelling approaches. It was found that the fracture strength of notched nanopaper is insensitive to notch length. Cohesive zone models were used to describe the fracture behaviour of notched cellulose nanopaper. Fracture energy was extracted from the cohesive zone models and divided into an energy component consumed by damage in materials and a component related to pull-out and bridging of nanofibres between cracked surfaces which is not facilitated by short nanofibres in nanopaper. Strain mapping revealed a small region of highly localized strain ahead of the notch tip with multiple stress concentration sites which are indicative of a stress delocalization mechanism.

Secondly the inelastic deformation mechanisms of cellulose nanopaper were investigated. Results indicate that the inelastic deformation of cellulose nanopaper does not originate from fibre slippage and shearing as often suggested in literature but originates from inelastic deformation in amorphous regions in the cellulose nanofibres itself. It is proposed that this mechanism is associated with segmental motion of cellulose molecules facilitated by the breakage of hydrogen bonds within these amorphous regions.

Thirdly, the effect of preparation methods on the mechanical properties of cellulose nanopaper was investigated. The influence of processing parameters such as compaction

pressure and temperature was investigated and the mechanical properties of these nanopapers were compared with nanopaper prepared by a suspension casting method.

Finally, a micromechanical fibrous network model was used to investigate the parameters that determine the elastic modulus of cellulose nanopaper. The effect of fibre size, waviness and modulus, inter-fibre bond density as well as network density on elastic modulus was investigated.

Acknowledgements

PhD study is like a football match during which is full of ups and downs. All you can do is to make your best and never lose confidence since it is the heart of curiosity that is the motivation of doing research. This thesis is never a personal accomplishment but a product of cooperation from many people.

First, I would like to express my sincere gratitude to my supervisor Professor Ton Peijs for patient guidance in my PhD studies. His profound knowledge, easily understood explanation and scientific expression open the gate of science for me and allow me to grow from a student to a researcher that can think independently and critically.

Second, I would like to acknowledge the China Scholarship Council (CSC) for offering me such an exciting opportunity to gain international experience. Their financial support makes me completely focus on research without worrying about daily expense.

My special thanks will be given to Dr. Stergios Goutianos and Dr. Wei Tu for their continuous guidance and invaluable help. I learnt a lot of experimental and modelling skills from them and benefited a lot from their professional advice. I would also like to thank Prof. Lars Berglund from KTH (Sweden), Prof. Guang Yang from Huazhong University of Science and Technology (China) and Mr. Julien Amadou in Nanocyl S.A. (Belgium) for kindly providing materials in all these years. Dr. Emiliano Bilotti is also sincerely acknowledged for offering kind help. I would also like to thank Dr. Rory Wilson, Dr. Alice Williams and Mr. Roger Nelson for their technique support.

Many thanks to my colleagues Dr. Han Zhang, Dr. Jian Yao, Dr. Olivier Picot, Dr. Charline Sellam, Dr. Fang Mai and Dr. Yiwei Sun as well as the doctors in the near future Yan Li, Yi Liu and Yuqing Gao for their help in any form.

I would like to thank my families and friends for giving me huge support in my stressful and depressed days. A huge thank to my loved girlfriend Nan Meng for her understanding during my PhD life.

My PhD is coming to an end but there are many things worthy of memorizing in my whole life. Looking back to these years, my life was full of feelings of happiness and excitement as well as frustration and depression. But that is a way of life, that is PhD and I like it.

Table of contents

List of notations and abbreviations

a	Crack length
AFM	Atomic-force microscopy
ANBF	Average number of bonds per fibre
B	Specimen thickness
BC	Bacterial cellulose
$\vec{C}_h$	Chiral vector
CS	Cross-sectional
CTE	Coefficient of thermal expansion
CTOD	Critical crack tip opening displacement
CVD	Chemical vapour deposition
DCB	Double cantilever beam
DENT	Double edge notch tensile testing
DIC	Digital image correlation
DP	Degree of polymerization
ds	Length increment along the contour in J-integral
E'	Young's modulus for plane stress
E_c	Elastic modulus of the composite
E_f	Elastic modulus of fibre
E_m	Elastic modulus of matrix
EPRM	Elastic-plastic fracture mechanics
EWF	Essential work of fracture
f	Herman's orientation factors
F	Dimensionless stress intensity solution related to testing configuration
FE	Finite element

G_b	Energy dissipation by pull-out or fibre bridging at the wake of crack tip
G_d	Energy consumed by damage in materials
G_e	Total fracture energy
I	Light beam intensity
I_0	Incident light beam intensity
IFPZ	Inner fracture process zone
IP	In-plane direction
J	J-integral
J_{IC}	Critical value of J-integral at crack initiation
J_R	Fracture resistance
K	Stress intensity factor
K_c	Critical stress intensity factor
K_I	Stress intensity factor for mode I
K_{Ic}	Critical stress intensity factor for mode I
L	Ligament length
LEFM	Linear elastic fracture mechanics
MD	Machine direction
MFA	Microfibril angle
MWCNT	Multi-walled carbon nanotube
NCC	Nanocrystalline cellulose
NFC	Nanofibrillated cellulose
OPDZ	Outer process dissipation zone
P	Applied force
P05T93	Sample hot pressed at 0.5 MPa and 93 °C
P10T37	Sample hot pressed at 10 MPa and 37 °C

P10T93	Sample hot pressed at 10 MPa and 93 °C
P5T93	Sample hot pressed at 5 MPa and 93 °C
POM	Polarized optical microscopy
R	Gas constant
RH	Relative humidity
ROM	Rule-of-mixture
SC	Suspension casting
SEM	Scanning electron microscopy
SWCNT	Single-walled carbon nanotube
T	Absolute temperature
t	Thickness of specimens in EWF testing
T_i	Components of the traction vector in J-integral
u_i	Displacement vector components in J-integral
V	Activation volume
V_f	Volume fraction of fibres
V_m	Volume fraction of matrix
W	Width of specimens
w	Strain energy density in J-integral
w_e	Value of essential work of fracture
w'	Half width of the sample
WAXD	Wide angle X-ray diffraction
W_f	Total work of fracture in EWF testing
w_f	Specific work of fracture in EWF testing
w_p	Energy density dissipated in the neighbouring region in EWF testing
α	Notch sensitivity parameter

β	Shape factor in EWF testing
Γ	Energy to separate unit area at crack
ΔH	Activation energy
δ	Phase difference
δ^*	Normal end opening of the cohesive zone
$\dot{\varepsilon}$	Strain rate
$\dot{\varepsilon}_0$	Constant pre-exponential factor
η_l	Fibre length distribution factor
η_o	Krenchel's efficiency factor
$\sum Aa$	Area under the fitted peak of amorphous region in WAXD data
$\sum Ac$	Area under the fitted peak of crystalline region in WAXD data
σ_0	Strength of an unnotched sample
σ_f	Fracture strength of the notched sample
σ_y	Yield stress
σ_{YS}	Yield strength
Φ	Azimuthal angle
φ	Angle between the optical axis and the polarization axis of the polarizer
χ_c	Crystallinity

List of Tables

List of Figures

Chapter 1

Introduction

1.1 Background

With the rapid increasing population, the environmental issues with respect to the waste of materials like plastics become critical. Eco-friendly materials need to be developed to replace the current synthetic materials which are often difficult to degrade. Cellulose is one of the most abundant and ubiquitous natural materials that exhibit renewability, sustainability and biodegradability [1]. In addition, cellulose shows favourable mechanical properties and has been used as a reinforcement in many composites [2, 3]. One of the most common applications of cellulose is to produce paper where cellulose fibres are isolated during pulping processes followed by a paper-making process. Conventional papers are vulnerable to external forces due to weak inter-fibre connectivity as well as low density of the papers [4].

Cellulose fibres can be further disintegrated, which results in cellulose nanofibres (diameters ranging from several to several tens of nanometres) with numerous hydroxyl groups on their surfaces. Using fairly traditional paper-making processes, cellulose nanopaper can be formed from nanofibres which are connected by large amounts of hydrogen bonds at their intersections. Cellulose nanopapers are dense, strong and flexible films with strengths exceeding 200 MPa and Young's moduli over 10 GPa [4]. They also show good oxygen barrier properties [5], high optical transparency [6] as well as low

thermal expansion [7] and have been investigated for applications, such as packaging materials [8] and substrates for flexible displays [9].

So far, much effort regarding cellulose nanopaper have been made on a) tailoring mechanical properties of cellulose nanopapers using different cellulose sources and preparation methods [4, 10-13]; b) exploiting a combination of mechanical properties and physical properties, such as optical transparency and barrier properties of nanopapers [6, 14, 15]; and c) taking advantage of the mechanical properties of nanopapers in cellulose based nanocomposites [9, 16, 17]. Although the mechanical properties of cellulose nanopapers are important and extensive investigations have been devoted to the tailoring and optimization of mechanical properties, fundamental studies on the mechanics of cellulose nanopaper are rarely reported. Specifically, fundamental knowledge regarding the fracture properties and inelastic deformation mechanisms of cellulose nanopapers still remain unclear.

1.2 Objective of the thesis

The aim of the current work is therefore to： a) investigate the fracture properties and inelastic deformation mechanisms of cellulose nanopaper; and b) investigate structure-property relationships using both experimental and modelling methodologies.

1.3 Scope of the thesis

The structure of the thesis is divided as follows: Chapter 1 briefly introduces the background of cellulose nanopaper and the aim of the thesis. Chapter 2 provides a review of the literature associated with cellulose structure, nanocelluose, cellulose nanopapers, the fracture mechanics of paper materials, the inelastic deformation mechanisms in

cellulose nanopapers and the micromechanical modelling of cellulose nanopaper. In this thesis, the fracture properties of cellulose nanopapers are compared with that of multi-walled carbon nanotubes (MWCNTs) based buckypaper. Therefore, the literature of carbon nanotube and buckypaper are also reviewed. Chapter 3 depicts the preparation of the samples and characterization methods. Chapter 4 investigates the fracture properties of cellulose nanopaper using both experimental and modelling methodologies. The fracture strength, notch sensitivity, cohesive fracture strength and fracture energy are investigated. Strain distribution of notched cellulose nanopapers are also investigated. Chapter 5 investigates the inelastic deformation mechanisms in cellulose nanopaper at different hierarchical levels using characterization techniques such as mechanical testing, digital image correlation, Raman spectra, wide angle X-ray diffraction analysis, polarized optical microscopy and temperature dependent dielectric spectra. Chapter 6 investigates the structure-property relationship of cellulose nanopapers using different preparation methods. Chapter 7 investigates the dependence of elastic modulus of cellulose nanopapers (represented by fibrous network models) on various factors such as fibre dimensions, waviness and modulus, inter-fibre bonding density as well as the density of networks using finite element methods. Chapter 8 summarizes the findings of the project and proposes some future work.

Chapter 2

Literature review

2.1 Cellulose

Materials derived from nature are now considered as promising alternatives to traditional petroleum products due to their renewability, sustainability and environmental friendliness. Natural fibres such as lignocellulose fibres are among the promising alternatives because of their abundance, renewability, biodegradability, lightweight and low cost [3].

The origin of cellulose is diverse - either from plants such as wood, flax, hemp, ramie, cotton or from non-plant sources such as bacteria and tunicates [18]. Cellulose was first given its name by Anselme Payen who also determined the molecular formula of cellulose as $(C_6H_{10}O_5)_n$ [19]. The repeat unit in molecules is composed of two anhydroglucose rings which are linked by β 1-4 glucosidic bonding. Hydroxyl groups that extend from the backbone can provide firm intermolecular bonding when cellulose molecules aggregate (Figure 2.1) [20]. Although the molecular structure is simple, cellulose is one of the most important components in plants. Cellulose chains can aggregate to microfibrils through hydrogen bonding and these microfibrils can bind into microfibrillated cellulose and further cellulose fibres (Figure 2.2) [21].

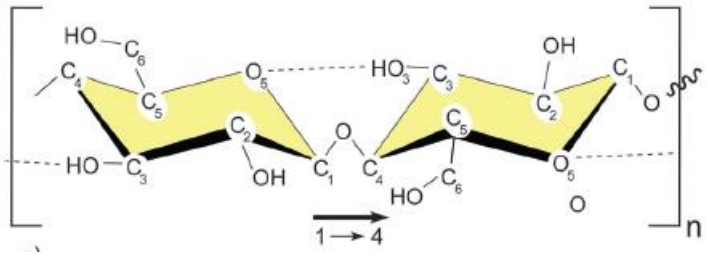

Figure 2.1 Molecular structure of cellulose (dotted lines are hydrogen bonds) [22].

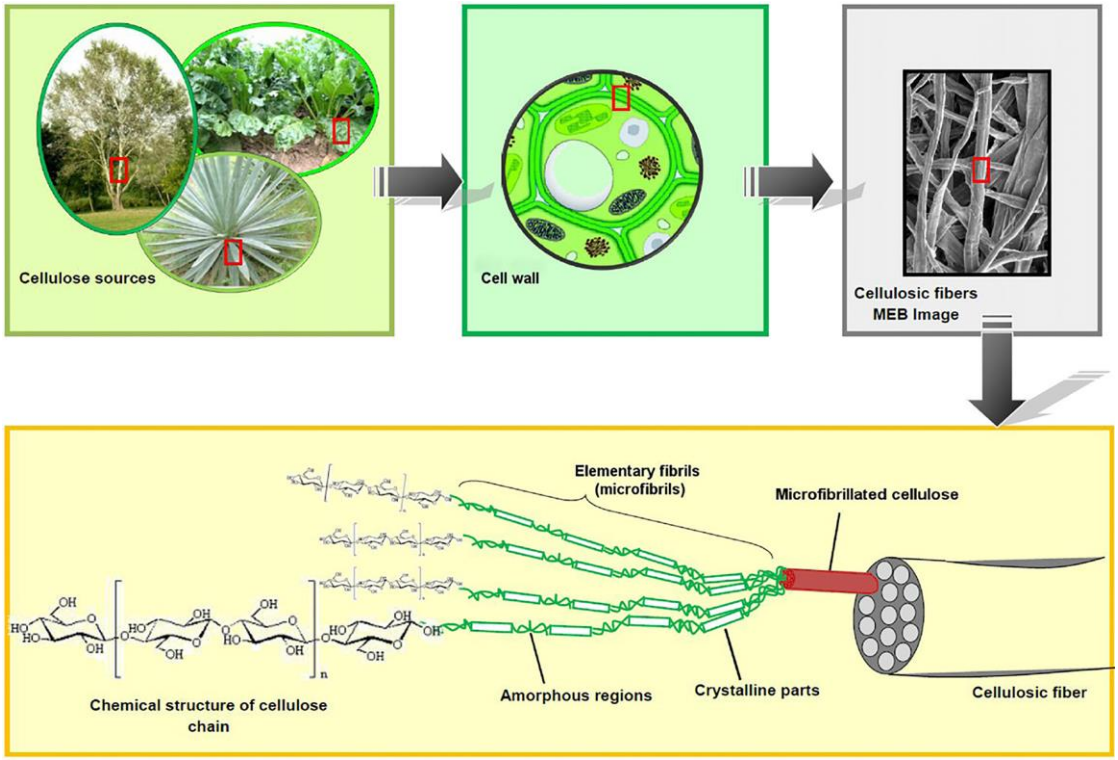

Figure 2.2 Hierachical structure of cellulose [21].

Like semi-crystalline polymers, cellulose microfibrils consist of alternating highly ordered regions (crystalline) which contribute to the stiffness of microfibril and disordered (amorphous) regions which make the microfibril flexible [22, 23]. Four polymorphs have been observed in cellulose: I, II, III and IV, among which only cellulose I is naturally produced. Cellulose I consists of two crystalline structures: cellulose I_α and

I_β, corresponding to triclinic and monoclinic structures, respectively [22]. I_α is metastable and can be converted to I_β by hydrothermal treatment [24]. The ratio of Iα/Iβ depends on the origin of cellulose, which has been investigated using solid-state C-13 NMR [20, 25]. Crystalline cellulose is a promising candidate as a reinforcing phase in polymer composites due to its high elastic modulus which was reported to be as high as 138 GPa [26], a value that is higher than synthetic fibres like Kevlar-29 [27] and comparable to Kevlar-49 [12]. Furthermore, the low density of cellulose (1.5 g/cm^3) imparts itself a high specific modulus (92 $GPaMg^{-1}m^3$) which is 3.5 times stiffer than steel [18]. However, the application of cellulose as an engineering material is still limited since cellulose is moisture sensitive and enzymatically degradable [18].

2.2 Nanocellulose

Nanocellulose refers to isolated cellulosic materials with at least one dimension in the nanometer range [1]. It exhibits nanosize, high aspect ratio, high specific surface area, hydrophilicity and chemical modification capacity. According to the source, structure and preparation route, the most used nanocellulose can be divided into three subcategories: nanofibrillated cellulose (NFC), bacterial cellulose (BC) and nanocrystalline cellulose (NCC). NFC are usually extracted using a top-down method which involves the isolation of NFC from plants. On the contrary, BC are often synthesized by a bottom-up method which involves biosynthesis processes in bacteria and exist in the form of fibrous pellicles. NCC are rod-like particles with high crystallinity and can be produced by acid hydrolysis which diminishes disordered regions in cellulose [1]. The comparison of NFC, BC and NCC is illustrated in Table 2.1. This review will mainly focus on NFC and BC in the following sections since NCC is not used in this thesis.

Table 2.1 Comparison of NFC, BC and NCC

	NFC	BC	NCC
Sources	Wood and plants such as hemp, flax, sugar beet, cotton	Low molecular sugar and alcohols	Wood, plants, tunicin, algae and microcrystalline cellulose
Preparation	Delamination of cell wall	Bacterial synthesis	Acidic hydrolysis [28] or ionic liquid solvolysis [29]
Dimension	Width: 5-100 nm length: several micrometers [30-32]	Ribbon shape width: 30-50 nm thickness: 6-10 nm [33]	Width: 3-28 nm length: 70 nm to 1.6 μm [28, 29]
Crystallinity (%)	44-90 [19, 34, 35]	63 (agitated) and 71 (static) [36]	75-95 [29, 37, 38]
Allomorphs	Iβ prevailing [39]	Iα dominating [39]	-

2.2.1 Nanofibrillated cellulose (NFC)

Nanofibrillated cellulose are either single microfibrils or their nano-size bundles which are usually extracted from plants through mechanical treatment. The hierarchical structure of plants can be exemplified by the tree structure illustrated in Figure 2.3. The cell wall structure in plants is multi-layered and consists of middle lamellae, primary cell wall and secondary cell wall which is further composed of S1, S2 and S3 layers. Cellulose microfibrils align in a tilted angle relative to the longitudinal cell axis (microfibril angle or MFA) in the S2 layer, which is significantly relevant to the mechanical properties of the cell wall [2, 40, 41]. Cellulose microfibrils are never the only component in plant cell walls but are surrounded by other constituents such as hemicellulose and lignin, which act as a matrix. The distribution of cellulose, hemicellulose and lignin are described in Figure 2.4.

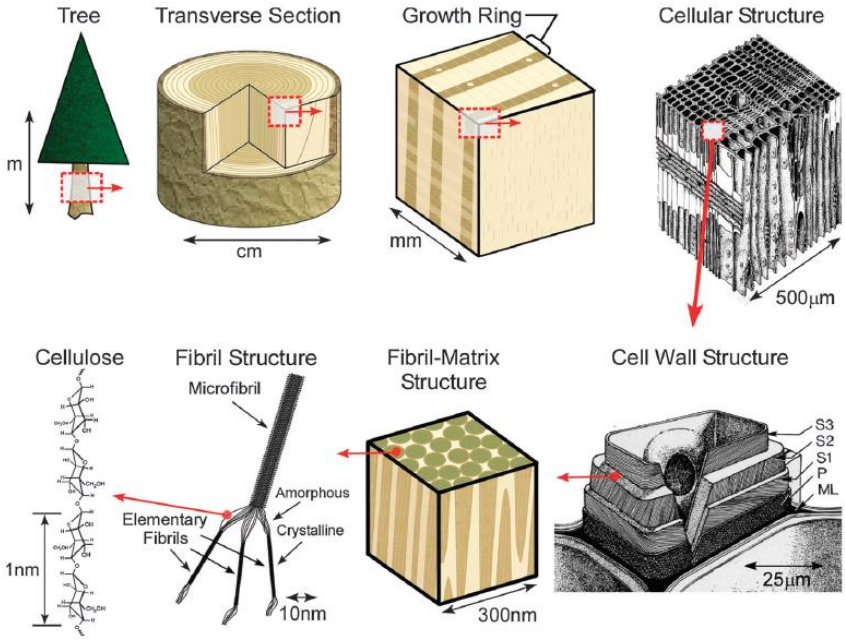

Figure 2.3 Schematic of the hierarchical structure of a tree [42].

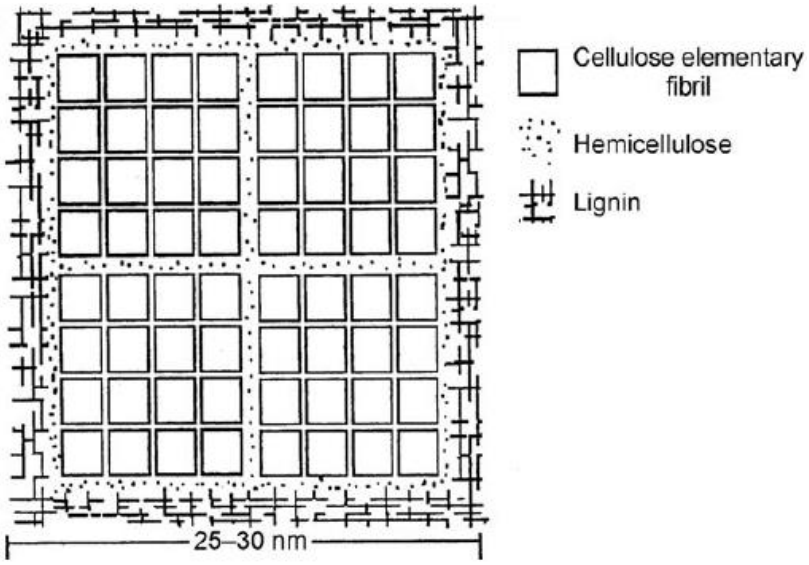

Figure 2.4 Model of the ultrastructure organization of the cell wall components in wood [43].

Cellulose fibres can be extracted from the plant cell wall through a pulping process during which bulk cellulose sources are broken down into constitutive cellulose fibres using mechanical and/or chemical methods [44]. NFC nanofibres can be further isolated from

those cellulosic pulp fibres by mechanical refining methods which were first introduced by Turbak et al. [45] and Herrick et al. [46]. In their methods, the diluted slurries of cellulose fibres were subjected to a high pressure homogenizer for several passes during which cellulose fibres were delaminated into nanofibres with 10-100 nm wide in gel-like form with water. Microfluidizers which provide high shear and impact forces were also used as an alternative to a homogenizer. Cellulose nanofibres with diameters range from 28-100 nm were prepared by 10 passes through the microfluidizer [32]. Other methods such as grinding [47], cryocrushing [48], ultrasonification [49] have all been used for the production of cellulose nanofibres. The disadvantage of purely using mechanical treatments is the high energy consumption during the homogenization process, which has become the main hindrance for large scale processing [50]. To solve this problem, the pretreatment of cellulose fibres before mechanical disintegration has been developed with the aim to weaken the connections between microfibrils.

The pretreatment of cellulose fibres can be generally divided into two approaches: enzymatic and chemical treatment. In nature, the degradation of cellulose involves the synergistic work of three types of cellulases which are endoglucanase, cellobiohydrolase and β-glucosidase. First, endoglucanases randomly hydrolyze β-1, 4-glucosidic bonds of cellulose chains in disordered regions resulting in more chain ends. Then, cellobiohydrolase acts on cellulose chain ends to release soluble cellobiose or glucose. Finally, β-glucosidases hydrolyze cellobiose to glucose [51]. In practice, endoglucanase can be used to facilitate the disintegration of NFC nanofibres with high aspect ratios (width of 15–30 nm and length of several micrometers), during which enzymatic pretreatment assisted the swelling of cellulose pulp fibres while the reduction of length

of nanofibres was limited [31]. Enzymatic pretreatment is an environmentally friendly method and shows great potential for mass production.

An alternative approach to pretreatment cellulose fibres is chemical pretreatment which takes advantage of large amounts of hydroxyl groups as ideal reaction sites at the surfaces of microfibrils. The individualization of cellulose microfibrils through TEMPO-oxidation modification prior to mechanical treatment for various sources was firstly reported by Saito et al. in 2006 [52]. Individual cellulose microfibrils of 3-5 nm wide were obtained from wood pulp and cotton fibres. During the chemical process, the C6 primary hydroxyls of cellulose can be selectively oxidized to carboxylate groups by TEMPO/NaCIO/NaBr oxidation system in alkali environment (Figure 2.5). The resulting carboxylate groups assist the swelling of TEMPO-oxidized cellulose by increasing anionic surface charge [30, 53]. The drawback of this method is that the chemical process will severely reduce the degree of polymerization (DP) by as much as 70% [30, 54]. To avoid the reduction of DP, TEMPO/NaClO/$NaClO_2$ oxidation system has been developed in 2009 where the depolymerization was suppressed [55]. The advantage of this chemical approach is to generate smaller nanofibres of more regular size whereas the chemical reagents are not environmentally friendly. In 2008, carboxymethylation was used as another chemical approach for pretreatment where the hydroxyl groups on microfibril surfaces was substituted by carboxymethyl groups [56]. The lateral dimension of the nanofibres ranges from 5 to 15 nm which fall in between enzymatic and TEMPO pretreated ones.

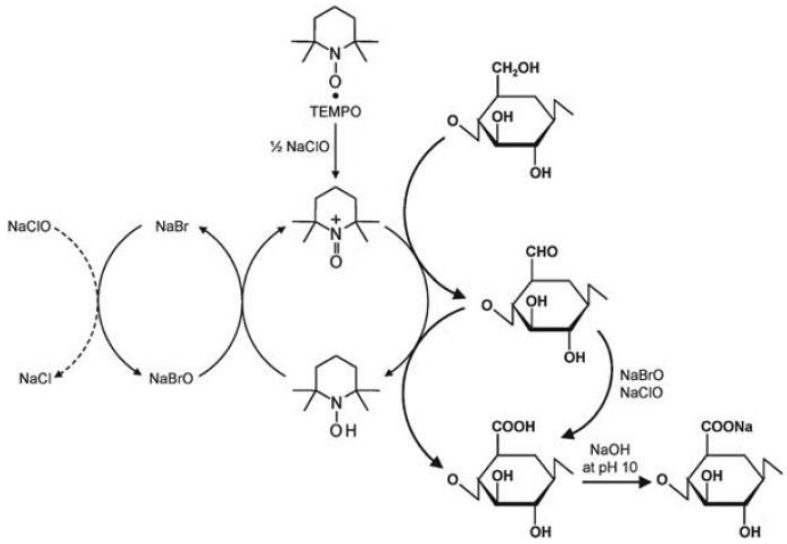

Figure 2.5 Regioselective oxidation of C6 primary hydroxyls of cellulose to C6 carboxylate groups [30].

The mechanical property of NFC have barely been reported since direct tensile measurement on a single cellulose nanofibre is difficult. However, average mechanical properties of NFC are important and measurable by indirect methods. The effective Young's modulus of individual NFC nanofibres was estimated using polarized Raman spectroscopy with value ranging from 29-36 GPa for enzymatic-pretreated cellulose nanofibres [57]. The average strength of single cellulose nanofibres was also reported by Saito et al. who used a model which related tensile strength to aspect ratio and estimated a tensile strength of wood-based TEMPO-pretreated cellulose nanofibres of 1.6 to 3 GPa [58].

The high modulus and strength of NFC nanofibres make them interesting nanofillers for nanocomposites. Enhanced mechanical properties have been reported by the addition of NFC nanofibres into either hydrophilic matrix such as phenol–formaldehyde [59] and melamine-formaldehyde resin [60] or hydrophobic matrix such as PE and PP [61].

Biodegradable matrices such as starch [62], PLA [63] and PVA [17] have also been used to prepare green nanocomposites with NFC nanofibres. The reinforcing efficiency is maximized when the NFC nanofibres can connect and form a stable network in nanocomposites [63].

2.2.2 Bacterial cellulose (BC)

Bacterial cellulose is a product of primary metabolism process of bacteria which was first confirmed by Brown who worked with acetic acid bacteria and identified a gelatinous material in vinegar fermentation [64]. Although BC is able to be synthesized by bacteria from many genera, only the *Acetobacter* species which are Gram-negative, aerobic, rod-like microorganisms and can survive in acidic environments, have the potential for mass production of cellulose [1]. The most investigated BC-producing bacterium is *Acetobacter xylinum* which has been widely observed in places of fermentation of sugar and plant carbohydrates where it converts low molecular sugar into pure cellulose [50].

The biosynthesis of BC nanofibres is an extracellular process. The bacterium secretes on its surface cellulose ribbons which are assembled by various number of cellulose microfibrils [65]. The thickness and width of the BC ribbons were reported to be 3-4 nm and 70-80 nm, respectively by Zaar [65] as well as 2.2-6.2 nm and 98-140 nm by Yamanaka et al. [66]. The ribbons form a dense 3D fibrous network (in the form of gelatinous pellicle) through hydrogen bonds.

The resulting BC pellicles in the culture medium are impure since bacteria and residues are trapped in the pores of the fibrous network. Therefore, suitable purification is required for the isolation of never-dried BC pellicles. Usually, BC pellicles are treated using

diluted sodium hydroxide solutions [67]. It is worth noting that alkali treatment with high concentration solution for long time may cause the polymorphic transformation from cellulose I to cellulose II. A two-step purification of BC pellicles was recently developed by Gea [68]. BC pellicle was treated first by sodium hydroxide followed by sodium hypochlorite. The two-step treated BC pellicle showed clearer profile of BC nanofibres compared with BC pellicle treated by only sodium hydroxide solution where only cloudy aggregates of nanofibres could be identified. This could be attributed to the effectiveness of sodium hypochlorite in removing impurities left after alkali treatment. The purified BC pellicle showed better mechanical properties than untreated BC pellicle when converted to BC dry sheet because the removal of impurities in the pores of the network improved the formation of hydrogen bonds during drying.

The Young's modulus of individual BC nanofibres has been estimated using AFM. It was reported that the Young's modulus could be as high as 78±17 GPa for BC nanofibres with diameters in the range of 35-90 nm [69]. Similar Young's moduli of BC nanofibres (79-88 GPa) with diameters from 50 to 120 nm were also obtained from polarized Raman spectroscopy data [57].

One advantage of BC is that the biosynthesis process is controllable and tailorable. The dependence of ribbon size [66], modulus [66], crystal structure [33] and pore size [70] on additives in culture medium have been reported. The culture condition including pH and oxygen are also important factors. It was reported that the crystallinity, crystallite size and even crystallite phase were different for BC cultivated from either static or agitated culture where oxygen supply methods were different [36]. The ease of shaping of BC hydrogels is another superior property. BC hydrogel can be formed in line with the shape

of reactor. For instance, tubular hollow hydrogels with different sizes have been prepared by placing a template inside the cylindrical reactor [71].

2.3 Cellulose nanopapers

Cellulose nanopaper is a fibrous network analogous to conventional paper but consisting of cellulose nanofibres rather than the fibres in microscale in conventional papers [3]. It shows a combination of profound mechanical and physical properties. The formation of cellulose nanopaper prepared from NFC water suspensions can be divided into two subsequent sub-processes: the formation of hydrogels where nanofibres are entangled followed by the dewatering of the hydrogels until the formation of nanopapers where hydrogen bonding provides strong inter-fibre network connectivity [72]. Approaches such as suspension casting, filtration followed by hot pressing or oven drying as well as Rapid-Köthen are often used to prepare cellulose nanopapers [15]. The simplest but slowest method is suspension casting where cellulose water suspension evaporates under mild conditions which often takes several days. However, other methods involving filtration are much faster and cellulose nanopapers can be obtained within 3 hours. The fastest method to prepare nanopapers with pronounced mechanical properties is Rapid-Köthen where the filtered nanocellulose hydrogel is dried under vacuum and elevated temperatures [15]. During drying, the structure of the hydrogel collapses and capillary forces drag nanofibres close to each other [73]. Consequently, numerous hydrogen bonding can be formed due to surface attraction and a dense structure is formed [73]. BC nanopaper can also be prepared by first blending and homogenizing BC pellicles with water followed by the same preparation methods as for NFC nanopapers [74]. Alternatively, BC pellicle can also be directly dried to nanopaper in air or under pressure [75].

The structure of cellulose nanopaper has been characterized using scanning electron microscope [4]. Cellulose nanofibres and their bundles entangle with each other and are randomly distributed in the plane of the nanopapers (parallel to the nanopaper surface) (Figure 2.6 (a)). In the out-of-plane direction (thickness direction), layered structures can often be observed from cross-section areas of SEM images (Figure 2.6 (b)).

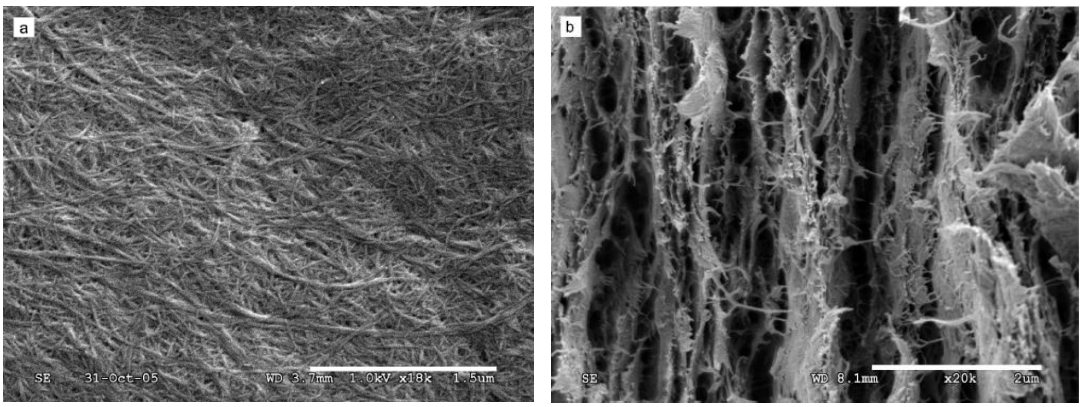

Figure 2.6 SEM images of (a) surface and (b) cross section of a fracture surface of NFC cellulose nanopaper [4].

The physical properties of cellulose nanopaper are attractive. Firstly, cellulose nanopaper is usually transparent or translucent since the size of nanofibres are usually smaller than the wavelength of visible light. The degree of transparency depends on the aggregation of nanofibres, the space between nanofibres and the surface roughness, which could reflect the light and reduce the light transmittance [6]. Secondly, densely compact nanopaper shows prominent gas barrier properties with an oxygen transmission rate of 17 ml m^{-2} day^{-1}. This value is comparable to EVOH which is often used as food package material [76]. Additionally, cellulose nanopaper exhibits a low coefficient of thermal expansion (CTE: 12-28.5 ppm K^{-1}), which is suitable to be used as an ideal substrate for flexible electronic devices [77].

Cellulose nanopaper also shows prominent mechanical properties with high strength (214 MPa) and Young's modulus (13.2 GPa) without compromising their toughness (15.1 MJ/m^3) [4]. The mechanical properties of cellulose nanopaper can be affected by many factors as shown in Table 2.2. The strength and strain-at-break of cellulose nanopaper increase prominently with increasing degree of polymerization [4]. Here, the failure mode was suggested to be related to the fracture of nanofibrils, which is facilitated by the slippage of cellulose chains in individual nanofibres. Drying methods significantly affect the mechanical properties of cellulose nanopaper [15]. Pores in cellulose nanopaper play a pivotal role in mechanical properties. It was reported that yield stress, ultimate tensile strength and modulus increase with decreasing porosity [4]. The influence of porosity was further investigated by producing tough nanopapers of higher porosity and high specific surface area [13]. High strength and modulus were observed with increased density and decreased specific surface area due to decreased segment lengths between inter-fibre bonding sites. The size of nanofibres also affects the mechanical properties of the nanopapers [78]. Cellulose nanopapers made of smaller nanofibres become stronger and tougher due to a reduced defect size and increased number of hydrogen bonds. Wood is one of the most important sources for the production of cellulose. It was reported that the source of wood had no significant influence on the mechanical properties of these nanofibres, which suggested that the inherent characteristics of cellulose nanofibres from different plant sources are similar [79, 80]. The filtrated wet cakes made of cellulose nanofibres and water were unidirectionally drawn prior to drying in order to investigate the effect of orientation of nanofibres on the mechanical properties of nanopaper [72]. The draw ratio was defined as the ratio of the specimen length after drawing to the original length. During drawing, nanofibres reoriented in the drawing direction, which resulted in drastically increasing in the strength and Young's modulus of cellulose nanopapers. Apart

from structure, testing conditions such as humidity also affect the mechanical properties of cellulose nanopaper [10]. It was reported that the strength and modulus decreased from 360 MPa and 20 GPa, to 34 MPa and 1.5 GPa, respectively when humidity increased from 0% RH to 100% RH. This was because water molecules interfered the hydrogen bonding between nanofibres, which weakened the fibre-fibre connections in cellulose nanopapers.

Table 2.2 Factors that influence the mechanical properties of nanopapers

Variables and values		Tensile strength (MPa)	Young's modulus (GPa)	Strain-at-break (%)	References
Degree of polymerization	410	129	13.7	3.3	[4]
	580	159	10.7	6.4	
	820	181	10.4	7.4	
	1100	214	13.2	10.1	
Nanopaper preparation methods	Rapid-Köthen	232	13.4	5.0	[15]
	Filtration + oven	211	12.1	6.6	
	Filtration + hot	178	10.3	6.3	
	Suspension	180	10.3	5.9	
Cellulose sources	Softwood	210	11	-	[79, 80]
	Rice straw	230	11	-	
	Potato pulp	230	11.4	-	
	Hardwood	222	6.2	7.0	
	Softwood	233	6.9	7.6	
Porosity (%)	19	205	14.7	6.9	[4]
	28	114	10.8	5.4	
	38	106	9.3	4.7	
	40	95	7.4	6.2	
Nanofibre diameters (nm)	11	275	-	8.5	[78]
	20	235	-	5.2	
	28	208	-	2.9	
Draw ratio	1	185	10.3	5.3	[72]
	1.2	345	17.3	3.5	
	1.4	428	24.6	4.5	
	1.6	397	33.3	1.8	

2.4 Inelastic deformation mechanisms in cellulose nanopaper

The stress-strain curve of cellulose nanopapers from tensile testing exhibits a short elastic region followed by a long region of inelasticity (Figure 2.7). The toughness of the cellulose nanopapers (defined as the work of fracture and represented by the area under the stress-strain curve) are mostly contributed by the energy consumed in the inelastic deformation. Therefore, the mechanism of inelastic deformation plays a key role in understanding the high toughness of cellulose nanopapers.

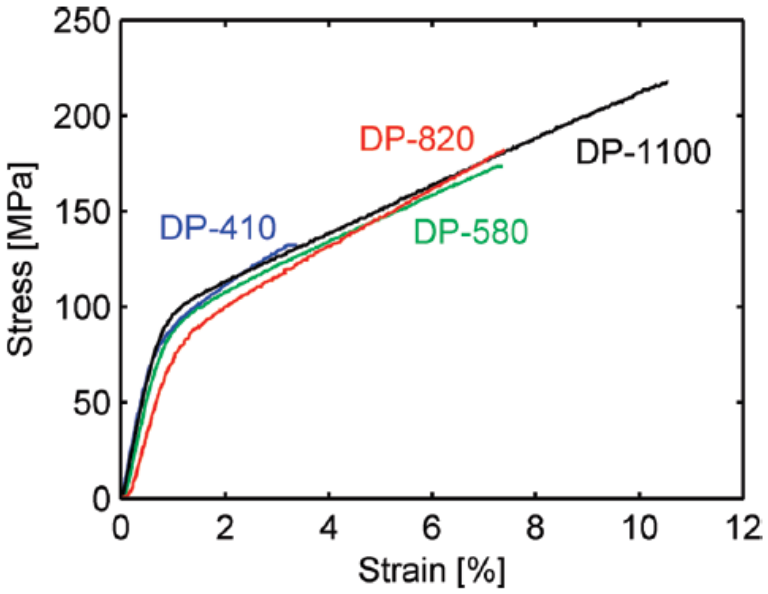

Figure 2.7 Typical stress-strain curves for NFC films prepared from NFC with different degrees of polymerization [4].

2.4.1 Toughening mechanisms

Toughness is important in practical use especially for engineering materials since they are often utilized in places where catastrophic failure is not allowed [81]. A tough material requires not only high strength but also high strain-to-failure where inelastic deformation is often involved. In fact, both strength and toughness need to be considered in the

selection of engineering materials. In many cases, the optimal engineering material often displays a trade-off between strength and toughness [81].

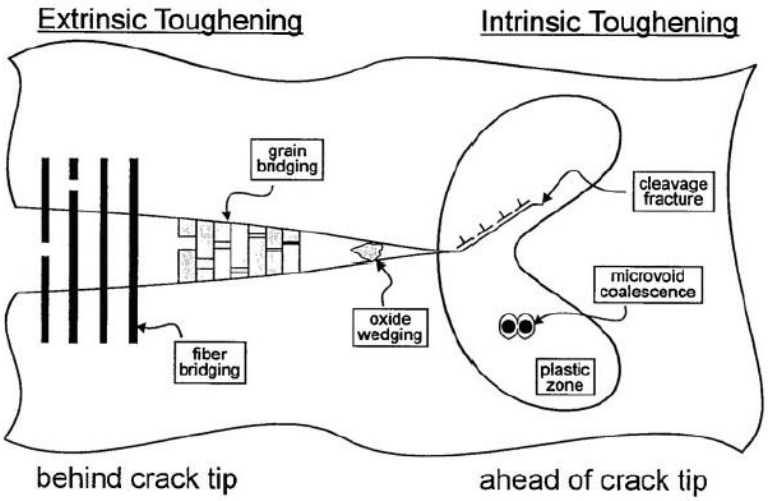

Figure 2.8 General concept of intrinsic and extrinsic toughening mechanisms [82].

Intrinsic and extrinsic toughening mechanisms are two prevalent toughening mechanisms (Figure 2.8) [81]. Intrinsic toughening takes place in front of the crack tip where the resistance to cracking is increased by changing the microstructures of the materials. The intrinsic toughening mechanism often involves plasticity and/or microvoid formed ahead of crack tip. This mechanism is usually observed in ductile materials such as polymers and metals whereas it is not effective in brittle materials such as ceramics where extrinsic toughening mechanism is active [81]. Extrinsic toughening operates primarily behind the crack tip and can be carried out through various approaches, such as crack deflection and meandering, zone shielding which refers to the inelastic or dilated zones surrounding the wake of the crack and contact shielding which refers to physical contact between mating crack surfaces directly or through an medium linking both crack surfaces [81, 83]. Therefore, extrinsic toughening mechanism can only act on crack propagations.

2.4.2 Possible inelastic deformation mechanisms in cellulose nanopapers

Cellulose nanopapers have hierarchical structures so that the inelastic deformation could therefore be related to mechanisms taking place in different structural levels. First, cellulose nanofibres are made of cellulose molecules which connect several crystalline and amorphous regions [84, 85]. These cellulose molecules could act like macromolecules in polymers where yielding is often considered as the primary inelastic deformation mechanism [81]. Therefore, the slippage of cellulose molecules could cause the inelastic deformation. Henriksson et al. proposed that the failure of cellulose nanopapers was due to fracturing of nanofibrils, which was induced by the slippage of extended cellulose molecules within individual nanofibrils [4]. Therefore, it is possible for the molecular chains to slide within individual nanofibres prior to being completely pulled out (failure of nanofibres and cellulose nanopapers).

Secondly, the inelastic deformation in cellulose nanopapers could be related to inter-fibre slippage, which is the prevailing hypothesis used in the literature. Hsieh et al. proposed that the inelastic behaviour was related to the breakdown of the fibrous network such as bond breaking and fibre pull-out or the twisting of individual cellulose fibrils [86]. According to Henriksson et al., the yield stress of cellulose nanopapers decreased with increasing porosity (Figure 2.9). They speculated that inelastic behaviour was associated with the onset of inter-fibre debonding and slippage facilitated by voids [4].

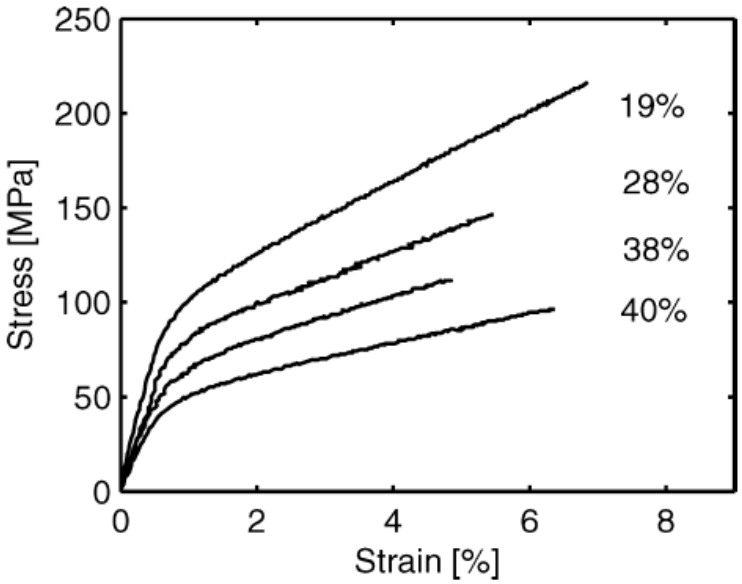

Figure 2.9 Typical stress-strain curves of NFC nanopapers with different porosities [4].

The inelastic deformation in cellulose nanopaper has been reported to depend on humidity [10]. The shape of stress-strain curves displayed huge differences when samples were tested under different relative humidity (RH) (Figure 2.10). There was no apparent inelastic region for nanopapers tested under 0% RH while inelasticity could be observed even at low RH. Inelastic deformation was further promoted (decreasing yield stress and slope of inelastic region) by increasing humidity. Here, the dependence of inelastic behaviour and toughness on RH was explained by inter-fibre debonding and possible sliding facilitated by water molecules. The water molecules in nanopapers at high RH also lower the inter-fibre friction and resulted in reduced strain hardening in the inelastic region.

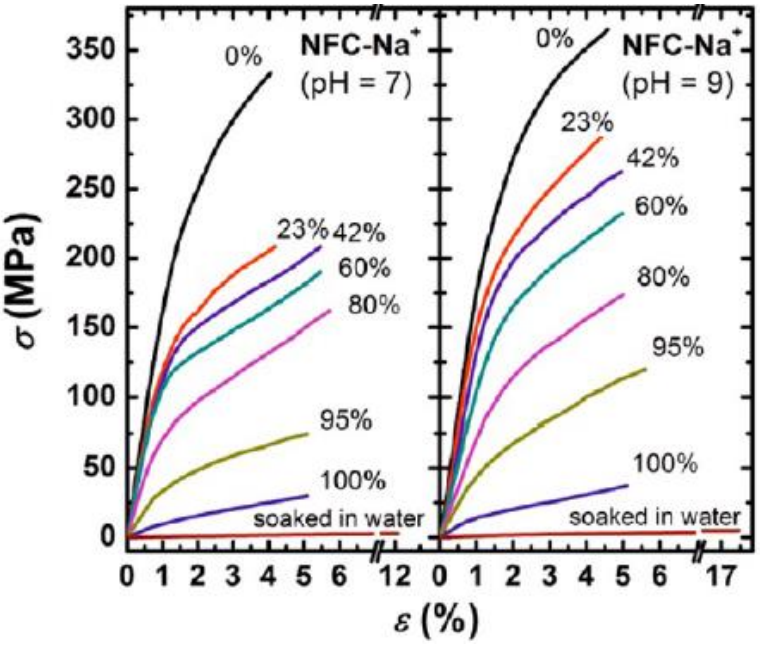

Figure 2.10 Mechanical properties of NFC nanopapers tested under different humidity [10].

Apart from the above mentioned mechanisms, a hypothesis termed 'stick-slip' mechanism was also used to explain the inelastic deformation in natural materials such as cell walls [2] and recently cellulose nanopapers [78]. This mechanism assumed a cascade of breakage and reformation of hydrogen bonds during inelastic deformation (Figure 2.11). The 'stick-slip' hypothesis was supported by atomistic simulations whereas no direct observations have been reported [78].

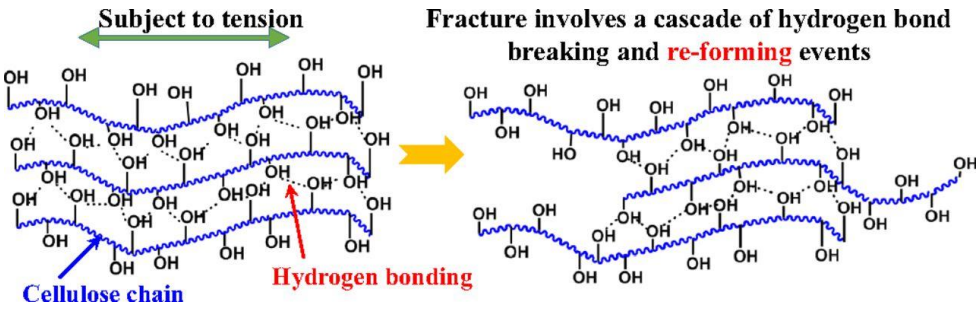

Figure 2.11 Envisioned inelastic deformation mechanism of cellulose nanopaper at molecular-level [78].

In summary, literature tends to attribute the inelastic behaviour of cellulose nanopaper to the breakage of inter-fibre hydrogen bonding and slippage of nanofibres. However, there has been no direct observation of this mechanism and further investigation is essential.

2.5 Fracture properties of notched paper materials

Papers are generally fibrous networks made of cellulose fibres in microscale. In this section, the fracture properties of notched paper materials are reviewed. First, the fracture behaviour of pre-cracked fibrous networks is reviewed, where the contribution of the microstructure to the mechanical behaviour is stressed. Then, the fracture mechanics of pre-cracked paper materials is reviewed, where the methods to determine the fracture toughness is emphasized.

2.5.1 Fracture behaviour of notched fibrous networks

Cracks are commonly observed in engineering materials where high stress is localized at the crack tip, which can lead to crack propagation and failure of the material. The resistance of fibrous network to cracks depends largely on the changes in microstructure of the networks under load. Both brittle and ductile failure of fibrous scaffolds have been observed [87]. Brittle failure takes place when fibres rupture without showing significant fibre realignment in the direction of tensile direction while ductile failure occurs when fibres realign in the tensile direction and a large number of fibre bundles are formed ahead of crack tip, which resists crack propagation. Inverse notch insensitivity has been observed in nonwoven fabrics where the failure stress of notched specimens is comparable or higher than that of unnotched ones [88]. Under tension, the fracture of inter-fibre bonds, crack blunting and re-orientation of fibres are considered as key mechanisms. The notch insensitivity of notched paper material was also observed in

sparse tissue papers with small notches [89]. This is because inhomogeneous mass and thickness distribution resulted in relatively large defects which govern the failure of notched specimens instead of small notches. In addition, the microstructure distributed stress near the crack tip and relieved the degree of stress concentration. The fracture strength of electrospun PA6 fibrous network was reported to be insensitive to the notch size [90]. This phenomenon was ascribed to diffused plastic zones, suggesting a stress delocalization mechanism. The insensitive of fracture strength to notch length with medium sizes was also reported for paper materials [91, 92]. This phenomenon was also ascribed to the spread-distributed stress in notched samples [92].

2.5.2 Basic fracture mechanics theories

It is well known that the material fractures at lower stress when defects such as cracks are introduced compared with unnotched one. Fracture mechanics provides mathematical relations among geometries of notched specimens, the loading configuration and fracture toughness [93]. Given loading configuration and geometry of specimens, fracture toughness can be solved to characterize the stress condition at the crack tip [94]. The measurement of fracture toughness requires specimens meeting specific geometry constraints and loading configurations in order to gain precise and non-geometry dependent values.

The earliest study on fracture mechanics was based on linear elastic materials and was called linear elastic fracture mechanics (LEFM) [94]. In this theory, the critical energy release rate (G_c) which is defined as the rate of potential energy variations per unit crack growth can be used as a measure of fracture toughness. Alternatively, fracture toughness can be represented by a constant value called stress intensity factor which determines the

stress distribution around the crack tip. The critical value of the stress intensity factor (K_c) is geometry independent and can be used as a failure criterion [94]. For mode I testing where loading direction is perpendicular to the crack plane, the critical stress intensity factor under plane strain condition is represented by K_{IC} which can be obtained by solving Equation 2.1 [94]:

$$K_I = \frac{P}{B\sqrt{W}} f\left(\frac{a}{W}\right) \qquad \text{Equation 2.1}$$

where P is the applied force, B is the specimen thickness, a is the crack length, W stands for the width of specimens and $f\left(\frac{a}{W}\right)$ is the dimensionless function related to the configuration of specimens. K_I can be interpreted as fracture toughness when the force at the fracture is used. The size requirements (Equation 2.2) of the specimens need to be met for the application of LEFM to ensure that the plastic zone ahead of crack tip is sufficiently small compared with notch length and ligament length and the materials are under plane strain condition [94]:

$$a, B, (W - a) \geq 2.5\left(\frac{K_{Ic}}{\sigma_{YS}}\right)^2 \qquad \text{Equation 2.2}$$

where σ_{YS} is the yield strength. Corrections dealing with small scale nonlinear material behaviour have been used to extend the validity of LEFM theory in which effective crack length is used instead of original crack length by adding the radius of plastic zone size into initial crack size [93]. In summary, LEFM theory can only be applied when materials show linear elastic or only small scale non-linear fracture behaviour.

LEFM is not applicable to materials where the plastic zone is large compared with notch length and ligament length. Instead, elastic-plastic fracture mechanics (EPRM) was developed for those materials with large scale nonlinear behaviour. One of the most successful approaches to measure the fracture toughness is the J-integral. This integral was designed to characterize the crack tip conditions in nonlinear elastic materials and can be used in elastic-plastic materials as long as the loading is proportional (no unloading). This value can be calculated by a path independent integral as below [94]:

$$J = \int_{\Gamma} \left(wdy - T_i \frac{\partial u_i}{\partial x} ds \right) \qquad \text{Equation 2.3}$$

where w is the strain energy density, T_i is the components of the traction vector, u_i is the displacement vector components and ds is the length increment along the contour Γ which is an arbitrary counterclockwise path around the tip of a crack. The critical value of the J at crack initiation (J_{IC}) is defined as fracture toughness and can be used as a failure criterion when crack propagation is unstable. For stable crack growth, a single value of fracture toughness is not a valid failure criterion since crack resistance depends on crack size. Instead, R-curves are often used to describe the relationship between material resistance against crack growth for a certain configuration [95].

Critical crack tip opening displacement (CTOD) is another useful fracture criterion, which reflects the degree of crack blunting when fracture occurs [94]. The CTOD value can be associated with either stress intensity factor (K_I) or J-integral under linear elastic and elastic plastic condition, respectively. The CTOD reaches a critical value when the stress intensity factor and J-integral also reach their critical values, respectively.

Apart from J-integral and CTOD, the fracture toughness of thin and ductile materials can be determined by the essential work of fracture (EWF) [96]. This approach clearly distinguishes the essential work that breaks the ligament region from the energy dissipated by plastic deformation in neighbouring region. In other words, the total work of fracture is divided into energy dissipated in the inner fracture process zone (IFPZ) and the outer process dissipation zone (OPDZ) (Figure 2.12) [97]. Those two energies are separately represented by the first and second item in Equation 2.4. To obtain the essential work of fracture, the w_f – L data points in Equation 2.5 need to be fitted with a linear function [98]:

$$W_f = w_e Lt + \beta\, w_p L^2 t \qquad \text{Equation 2.4}$$

$$w_f = w_e + \beta\, w_p L \qquad \text{Equation 2.5}$$

where W_f is the total work of fracture, w_f is the specific work of fracture, w_e is the essential work of fracture, w_p is the energy density dissipated in the neighbouring region, L is the ligament length, t is the thickness and β is the shape factor. The interception of the line and the w_f axis defines the essential work of fracture or fracture toughness. The EWF value is valid provided that a) full ligament yielding prior to crack initiation; b) loading-displacement curves for all ligament lengths are similar in shape; c) plane stress condition prevails [97, 99].

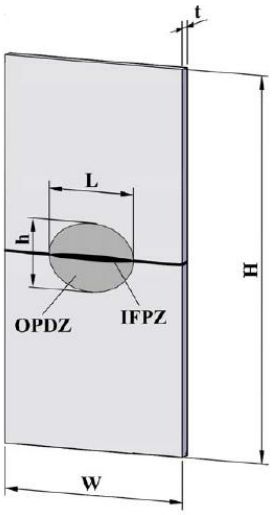

Figure 2.12 Schematic diagram showing the fracture zone containing IFPZ and OPDZ [97].

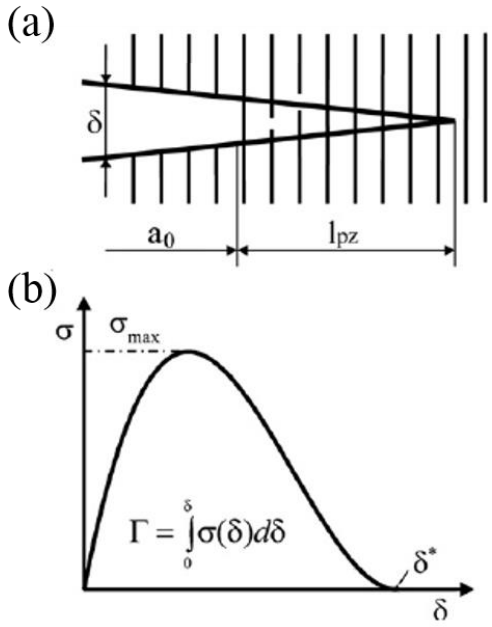

Figure 2.13 Schematic diagrams of (a) process zone (l_{pz}) in fibrous materials ahead of crack tip a_0 and (b) cohesive law [93].

Another generally used fracture mechanics approach is the cohesive zone model which can deal with the situation that material ahead of crack tip damages gradually in which

the condition at the crack tip is ill-defined (Figure 2.13(a)) [93]. In the model, cohesive law defines the relation between the traction and crack opening in the fracture process zone without necessarily taking into account the fracture mechanism (Figure 2.13(b)) [100]. The cohesive zone initiates when the stress reaches a critical value. Then, the stress decreases with respect to the opening until zero, where the opening value is defined as critical opening. The area under the entire cohesive law is the fracture energy [101]. The stress at the crack surface is not necessarily perpendicular to the crack plane since the cohesive law considers the local stress and opening in both normal and tangential directions [100]. In many cases, the determination of cohesive laws is through iterative comparing experimental data with modelling results by tailoring cohesive parameters. This approach is simple since no further experiments are required. However, the shape of traction-separation is arbitrary and the iteration process usually takes long time [102]. The other approach is to directly determine the cohesive law from experiments. For instance, the cohesive law can be derived from the measurement of the J-integral and the crack tip opening [103]. For mode I testing, the cohesive law can be determined by Equation 2.6 [104]:

$$\sigma = \frac{dJ_R}{d\delta^*} \qquad \text{Equation 2.6}$$

where J_R is the fracture resistance and $\delta^*$is the normal end opening of the cohesive zone. The area under the cohesive law is equivalent to the work of separation or fracture energy J_c when the initiation of crack growth occurs [104]. The disadvantage of this method is that the requirement of J-integral has to be met (no unloading of materials) and the loading configuration is complicated.

2.5.3 Application of fracture mechanics to paper materials

The fracture mechanics on paper materials has been extensively investigated. In early studies, linear elastic fracture mechanics (LEFM) was applied to brittle papers where the crack length was corrected by a plastic zone size [105]. The fracture toughness was consistent with the value of work of fracture from a stable quasi-static condition. In order for the LEFM to be valid, large specimen sizes and suitable crack lengths were used to ensure that the plastic zone at notch tip was small compared with the characteristic length of specimen such as ligament length and notch length so that the paper failed in a brittle manner. However, the requirement of large samples and that the size of the sample strongly depends on types of paper make it not suitable to measure fracture toughness in ductile papers with small sizes.

In that case, fracture mechanics approaches such as J-integral and EWF have been used to estimate fracture toughness. The geometry-independent J-integral can be obtained based on a multiple specimen technique which requires many specimens with different crack sizes and subsequent graphical processing [106]. In order to simplify the testing, a modified method where a minimum of two samples were required was developed by Yuhara and Kortschot [107]. The value of fracture toughness from this method was reported to be consistent with results from multiple-specimen method results. An alternative and simplified approach was Liebowitz non-linear technique where fewer specimens were required compared with multiple specimen technique [108]. The problem of J-integral is that the onset of crack growth is difficult to be determined precisely so that the critical value of the J-integral is hard to determine.

Fracture toughness data from the EWF method is independent of crack length and has been widely used for paper materials [98, 109, 110]. In 1995, Seth successfully used this method to measure the fracture toughness of ductile handsheet. He also proposed that the EWF theory was valid for ductile papers but was problematic when applied to brittle papers since for such papers, the ligament was unable to yield fully before final fracture [98, 111]. EWF method was further employed to obtain the fracture toughness of multiple types of papers such as copy paper, plaster linerboard, newsprint paper and filter paper and was proven to be valid for ductile paper materials [109, 110]. To obtain valid fracture toughness data from EWF tests, two requirements need to be noticed: a) the ligament length of the specimens is not too large in order to form an overlapping process zone between crack tips; b) the width of the specimen must be large enough to avoid that yielding spreads outside the specimen [98].

Cohesive zone models have no such limitations as required in EWF theory and have been widely used to obtain the fracture energy of paper materials. Östlund et al. compared the application of LEFM theory and the cohesive zone model for the fracture of copy paper. His results demonstrated that LEFM tended to overestimate the strength and proposed that the strength obtained from cohesive zone models exhibited good agreement with measured failure stress [112]. In their research, plasticity correction was used to modify crack length and the modified value was too large compared with notch length and specimen width, implying that the small scale yielding requirement was not fulfilled. Recently, cohesive zone models suitable for paper materials which exhibited progressive damage prior to failure were developed [113]. These models were achieved by first calibrating elastic-plastic models using tensile testing followed by calibration of cohesive law using stable tensile testing without involving any notched samples. The failure stress

of center cracked tension samples were successfully predicted. This method assumed that the damage was confined to a single straight zone which extended over the entire width, which is difficult to be fully fulfilled in practice. Zechner et al. proposed a method to directly determine the cohesive law for paper where deep notched specimens were used to ensure that the displacement along the ligament was approximately uniform [114]. The resulting cohesive strength and energy were 34.24 MPa and 3.82 kJ/m^2, respectively. The cohesive law was put into a finite element model which predicted well the fracture process for single edge notched tension samples. The cohesive law can also be experimentally derived from the measured J-integral. Goutianos et al. investigated the effect of refining time of cellulose fibres on cohesive laws in all-cellulose panels which were obtained from J-integrals measured by double cantilever beam (DCB) testing [115]. In their study, the shape of the cohesive law consisted of a steep decrease in cohesive stress followed by a gradual decrease in stress. The former one was ascribed to crack tip fracture while the latter was due to pull-out or bridging of fibres at the wake of the fracture surface. It was revealed that long refining time increased the peak cohesive stress but decreased the cohesive stress at bridging zone due to the formation of short fibres.

In summary, the fracture toughness of papers have been investigated using different methods. However, the fracture toughness of cellulose nanopaper was rarely reported. The LEFM theory is only suitable for brittle papers. The J-integral method requires precise measurement of onset of crack growth, which is difficult to achieve for papers due to the difficulty to define the crack tip. EWF method is only suitable for ductile papers. The cohesive zone model is considered to be the most appropriate method to determine the fracture energy of cellulose nanopaper since it has no such limitations as required in other methods.

2.6 Micromechanical modelling of fibrous networks without notch

Micromechanical modelling is particularly useful to investigate the effect of the microstructural properties on the mechanical properties of the nanopaper since the microstructural properties are difficult to determine by experiments. The structure of cellulose nanopaper is a fibrous network made of cellulose nanofibres. Fibrous networks can be modelled by either continuum models or discontinuous models (network models). The continuum micromechanical models require relationships between the mechanical properties of individual fibres and macroscopic network properties [116, 117]. An alternative modelling approach is to use nonlocal theory which links classical continuum formulations with micromechanical models by establishing a relationship between the local state variable with its nonlocal counterpart over a surrounding domain [118]. Nonlocal theory is necessary due to the fact that a) networks have pores that are not captured by classical continuum theory and b) long range interaction occur between fibres located at remote distances. By comparing the strain energy fields predicted from classical continuum theory, nonlocal theory and fibrous network models, Isaksson and Hägglund found that classical continuum theory is only valid for densely bonded networks while the strain energy field derived from nonlocal theory is valid even for networks of low density [119].

In discontinuous model, the fibrous network is built as a model and properties are assigned directly to individual fibres. The macroscopic mechanical properties of the fibrous network model are obtained by finite element analysis while microstructural properties can be tailored. The effect of fibre length, density of crosslinks and density of fibrous network on shear properties has been investigated using two-dimensional (2D) fibrous networks with fibres being discretized by beam elements and connected by rigid

bonds [120]. Results showed that the partially crosslinked networks made of long fibres exhibit the highest toughness. Bronkhorst (in 2003) used 2D random fibrous models to simulate the inelastic deformation of well-bonded paper [121]. In his model, plasticity stemmed from the inelastic deformation of fibres while the bonds were defined to be rigid at each inter-fibre crossing. Both tensile testing and cyclic loading testing were simulated using his model. Although rigid bonds were extensively adopted in the fibrous network model, the effect of the bond properties on the mechanical behaviour of the fibrous network also needs investigating. The relationship between bond fracture and macroscopic stiffness was investigated where bonds were represented by spring elements with stiffness in both translation and rotational directions [122]. The stiffness degradation of the model was found to be proportional to the cumulative number of bond fractures. In 1998, a stick-slip bond fracture model was developed by Heyden and Gustafsson to simulate mechanical behaviour of dry-formed cellulose networks [123]. Here the bonds between fibres could slip and the strength and modulus of the bonds degraded prior to complete failure when the slip reaches a specific value. Using this model, the effect of fibre curl and orientation on the elastic modulus of the model was investigated. Compared with 2D models, more microstructural parameters can be tailored in 3D network models despite of the high computational power required. In Lee's model, fibres were put in a 3D thin box and represented by linear Timoshenko beams with circular cross sections [124]. Bonds at the fibre intersections were considered as rigid. This model was employed to investigate the effect of fibre aspect ratio, fibre orientation and the existence of dangling fibres on the stiffness of the network. In 2012, Kulachenko and Uesaka developed a 3D fibrous network model which considers the contact and friction at fibre intersections where the fibre-fibre interaction model was based on AFM measurements [125]. This model was used to study the effect of fibre length and fibre curl on mechanical

properties. They found that fibre length showed great impact on elastic modulus, strength and strain-to-failure while fibre curl showed no obvious influence on any of the mechanical properties.

Although much effort has been made on the fibrous network models, the research on micromechanical modelling of cellulose nanopapers was barely reported. In 2012, Kulachenko et al. first developed 2D and 3D fibrous network models to investigate the elastic properties of cellulose nanopaper (Figure 2.14) [126]. In the 2D model, the fibres were simulated by beam elements. The fibres were point-wise connected at their intersection with both translational and rotational degrees of freedom at the contact points so that no nodes were shared between fibres. These 2D model was used to investigate the effect of density, non-crystalline regions, residual strains and fibre curvature on elastic modulus. Compared with the 2D model where fibres were intersected, the 3D model allowed fibres to wrap around each other (Figure 2.15). In the 3D-1 model, the fibre was cut upon crossing the other fibre. In the 3D-2 model, the fibres wrapped around the underlying fibres without cutting fibre sections. The effect of bond density and bond stiffness on the elastic modulus of the 3D models was also investigated.

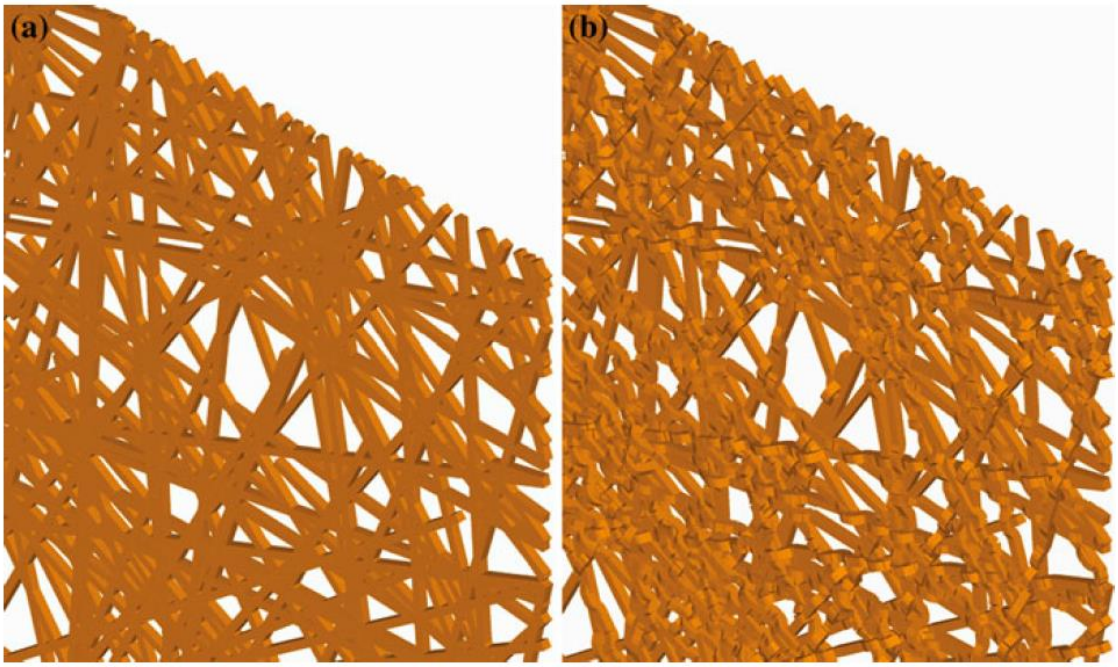

Figure 2.14 (a) 2D and (b) 3D models of cellulose nanopaper [126].

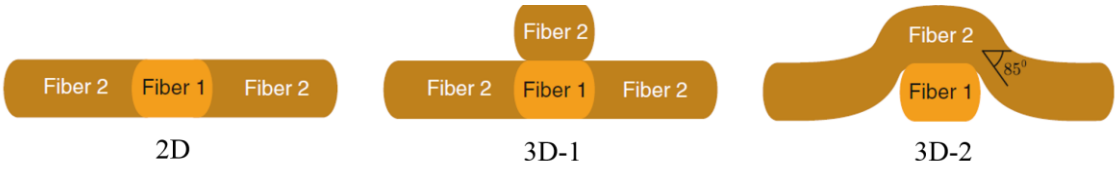

Figure 2.15 Different methods of compacting fibres in the models of cellulose nanopaper [126].

To summary, both 2D and 3D models have been used to simulate the mechanical properties of fibrous networks. However, the simulation of cellulose nanopapers was rarely reported. 2D models were convenient for simulation but the models have fewer parameters to adjust than 3D models. 3D models are more complicated and more micromechanical parameters can be adjusted. However, higher computational power is required in the 3D models.

2.7 Buckypaper

Although this thesis mainly focuses on cellulose nanopapers, the multi-wall carbon nanotube based buckypaper is also worthy of investigation. Because the fibre-fibre connection in buckypaper is van der Waals force which is weaker than the hydrogen bonding in cellulose nanopaper, it is interesting to compare cellulose nanopaper and buckypaper to study the effect of fibre-fibre connection on the mechanical properties. Therefore, the literature of carbon nanotubes and buckypaper is reviewed.

2.7.1 Structure of carbon nanotubes

Carbon nanotubes can be regarded as a rolled up sheet of graphite/graphene with a cap at each end, and wherein carbon atoms are arranged in a hexagonal array [127]. The structure of nanotubes may differ and can be represented by tube chirality which is defined by chiral vector, $\vec{C}_h$ and chiral angle, θ. The vector defines the direction of rolling of the graphite sheet and is composed of two unit vectors and their coefficients as shown in Equation 2.7 [127]:

$$\vec{C}_h = n\vec{a}_1 + m\vec{a}_2 \qquad \text{Equation 2.7}$$

where $\vec{a}_1$ and $\vec{a}_2$ are unit vectors, n and m are the steps along the carbon bonds in the hexagonal array shown in Figure 2.16. The graphene sheet is cut along the dotted lines and rolled to a tube where the tip of the chiral vector connects its tail.

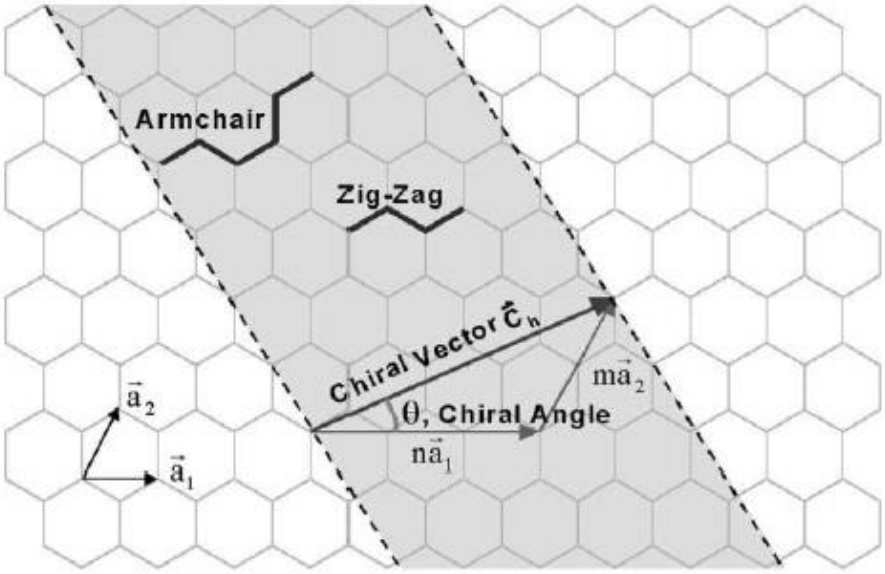

Figure 2.16 Schematic diagram showing the cutting and rolling of graphene sheet to nanotube [127].

The chiral angle determines the rolling direction of the sheet. There exist two special cases when the chiral angles are 0^o (zig-zag) and 30^o (armchair). The atomistic structure of the two nanotubes are illustrated in Figure 2.17. The atomistic structure of these two cases can also be represented in terms of chiral vectors where the coefficients (n, m) are (n, n) and (n, 0) for armchair and zig-zag, respectively [127]. Nanotubes with angles differing from these two special cases are considered as chiral. The dependence of mechanical properties of carbon nanotubes on chirality, tube radius and wall thickness has been analytically investigated by Veedu et al. [128]. It was found that Young's modulus decreases with increasing tube wall thickness and decreasing tube radius while the value of Young's modulus only slightly related to the chirality of the nanotubes.

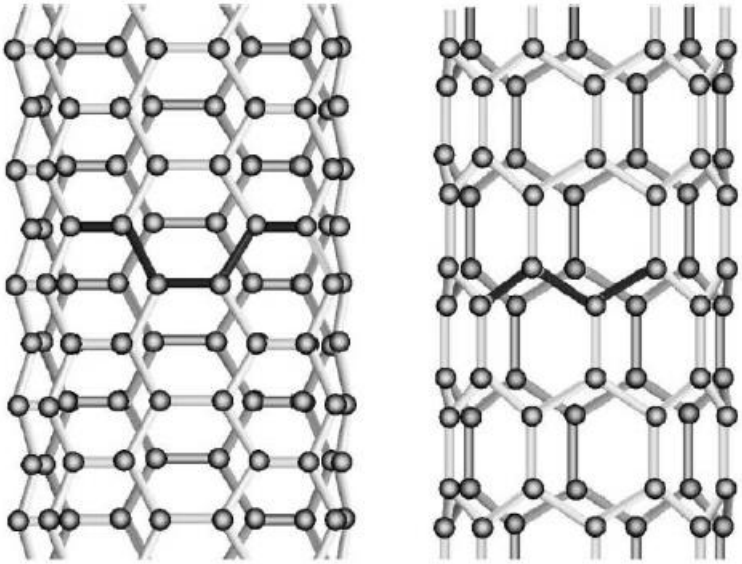

(a) (b)

Figure 2.17 Atomistic structure of the (a) armchair and (b) zig-zag nanotube [127].

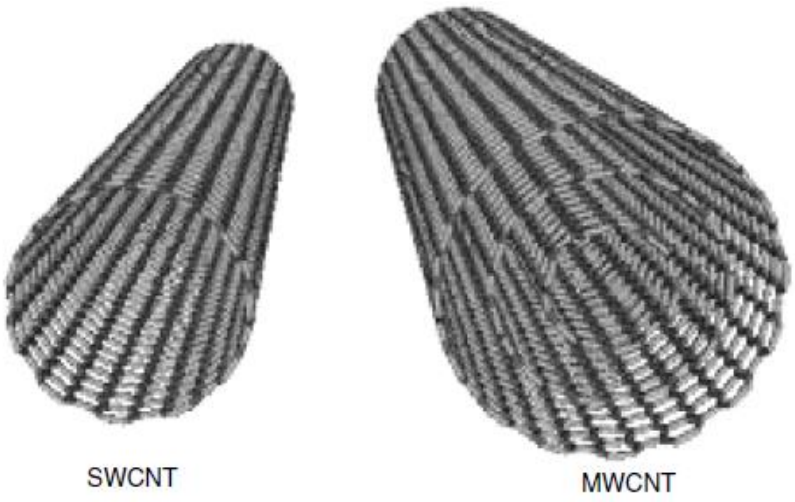

Figure 2.18 Single-walled (SWCNT) and multi-walled (MWCNT) carbon nanotubes [129].

Nanotubes can be categorized as either single-walled (SWCNT) or multi-walled (MWCNT) nanostructures according to the number of layers. Single-walled nanotubes can be visualized as a rolled up single layer of graphene. Multi-walled nanotubes are simply constituted by concentric single-walled nanotubes with different chirality which

are held together by van der Waals forces (Figure 2.18). This weak secondary bonding between layers severely impedes the load on the outer layer to be transferred to the inner layers so that the mechanical properties of MWCNT are inferior to those of SWCNT [130].

2.7.2 Mechanical properties of carbon nanotubes

Unlike bulk materials, it is difficult to precisely measure the mechanical properties of carbon nanotubes due to the difficulty in implementation of classic characterization techniques on such small sized material. However, a number of investigations have been performed on the direct measurement of mechanical properties of carbon nanotubes with the assist of atomic-force microscopy (AFM). Wong et al. was the first to conduct direct measurement of the bending properties on individual arc-MWCNT [131]. The MWCNT was pinned at one end and force was exerted on the unpinned end. The elastic modulus and average bending strength was measured at 1.26 TPa and 14.2 GPa, respectively. Salvetat et al. also measured the elastic modulus of MWCNT by AFM but using a different configuration [132]. An arc-MWCNT was placed over a hole in a TEM grid with both ends fixed and deflected by applying pressure through an AFM tip. The resulting elastic modulus was measured at 810 GPa. SWCNTs tend to self-assemble into close-packed bundles [133]. The measurement of elastic and shear modulus of individual SWCNT rope has also been performed using the bending configuration [133]. The elastic and shear modulus for thin SWCNT bundles was measured at 1 TPa and 1 GPa, respectively. Here the properties of SWCNT bundles decreased with increasing bundle diameter which indicated inter-tube shear slippage as the dominating deformation mode.

Instead of bending, tensile testing has also been performed to directly obtain elastic modulus. Yu et al. performed tensile tests on individual MWCNTs [134] and SWCNT ropes [135]. In their tests, a tensile force was applied by an AFM tip to which one end the nanotube was attached. For MWCNTs, the outermost tube failed while the inner layers were pulled out. The load was assumed to be carried mostly by outermost layer. By this the elastic modulus of the outermost layer was calculated ranging from 270 to 950 GPa with strengths ranging from 11 to 63 GPa. For SWCNT ropes, it was assumed that only nanotubes at the perimeter of the bundle or rope were able to carry load. Using this assumption the resulting tensile strength ranged from 13 to 52 GPa while the elastic modulus ranged from 320 to 1470 GPa. It is worth noting that all the estimations of modulus and strength are based on the assumption that the load transfer is primarily taking place in the outermost layer or tubes. In other words, the interaction between layers or tubes is considered rather weak. This is in line with the Raman data where a shift of the Raman peak corresponds to the strain in a layer [130]. The Raman peak of the inner layer only showed a tiny shift upon loading while the peak of outermost layer shifted massively (Figure 2.19), a clear indication of ineffective load transfer to inner layers.

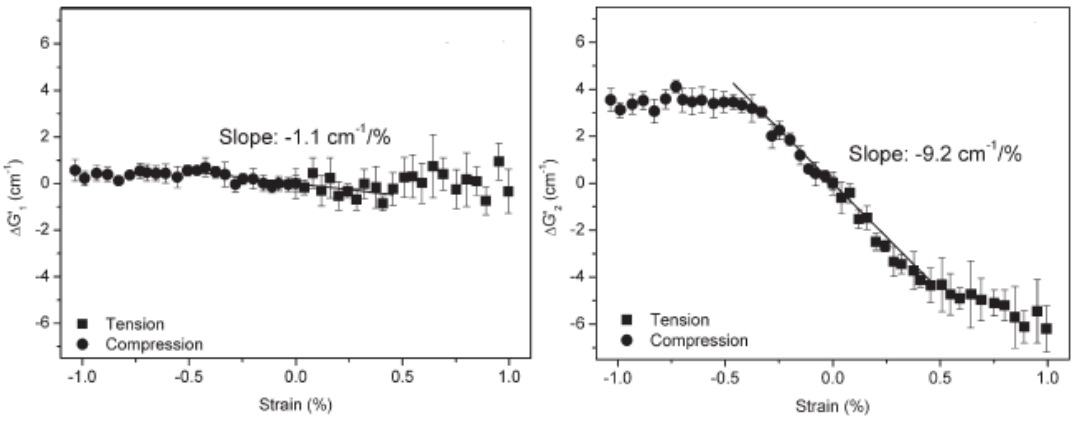

Figure 2.19 Raman peak shift for the inner walls (left) and outer walls (right) of MWCNTs [130].

2.7.3 Buckypaper and its mechanical properties

Buckypapers are fibrous networks consisting of carbon nanotubes which are mechanically entangled and connected by van der Waals forces. Free-standing buckypapers can be prepared by various methods such as chemical vapour deposition (CVD) [136], drop casting [137], spray coating [138] , hydro-entangling [139], vacuum filtration [140] and pressurized filtration [141]. The structure of the buckypaper prepared from filtration method is illustrated in Figure 2.20 where carbon nanotubes are randomly distributed in buckypaper.

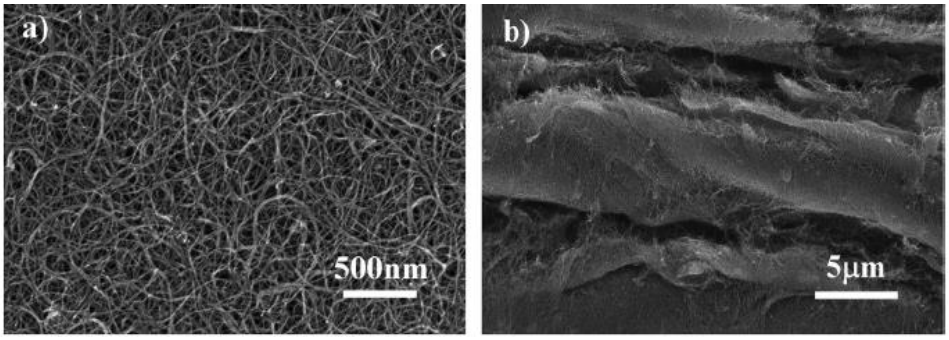

Figure 2.20 SEM images of buckypaper in (a) surface and (b) cross-section directions [140].

The mechanical properties of buckypaper vary in literature even for papers prepared by similar methods. For example, the Young's modulus, strength and strain-at-break of the aforementioned MWCNT buckypaper prepared by a filtration method were 1.37 GPa, 11.58 MPa and 8.89 %, respectively [142]. Buckypaper with similar modulus (1.9 GPa) and strength (12 MPa) but much lower strain-at-break (1 %) was also reported [139]. Extremely low mechanical properties of MWCNT buckypaper with modulus and strength of 0.25 GPa and 2.9 MPa, respectively, have also been reported [141]. Buckypaper made of SWCNT exhibited a modulus, strength and strain-at-break of 2 GPa, 16 MPa and 1.7 %,

respectively [143]. It is worth noting that surfactant is usually added to assist dispersion of nanotubes. Buckypaper prepared from suspensions showed an increase in Young's modulus and strength when surfactant was removed [144]. This is non-trivial as surfactant is expected to further lower the inter-tube interactions of the network. On the other hand, surfactant will improve nanotube dispersion in suspensions, leading to improved networks after casting and drying.

By comparing the mechanical properties of individual carbon nanotubes and buckypaper it can be concluded that buckypaper has significantly inferior mechanical properties compared to individual nanotubes due to the weak van der Waals interactions between the nanotubes, leading to weak networks. Hence, the failure of buckypaper is expected to be related to slippage or shearing of nanotubes rather than the failure of individual nanotubes.

In summary, nanocellulose is considered as a very promising material due to its nanoscale, high aspect ratio, and environmental friendly character. Cellulose nanopapers can be formed by the nanocellulose through hydrogen bonding. The mechanical properties of cellulose nanopaper can be affected by many factors such as degree of polymerization, nanofiber size, processing methods as well as humidity. To date, the fracture properties of conventional papers have been extensively investigated while investigations into the fracture properties of cellulose nanopapers is still lacking. In addition, the inelastic deformation mechanisms in cellulose nanopapers are rather speculative. Micromechanical modelling of the mechanical behaviour of cellulose nanopaper has also been rarely reported. Therefore, it is interesting to investigate the mechanics of cellulose nanopapers from more fundamental aspects. Apart from cellulose nanopapers,

buckypaper is another widely used nanopaper. The connections in buckypaper are van der Waals force which is much weaker than the hydrogen bonding in cellulose nanopapers. Hence, it is interesting to compare the mechanical properties of cellulose nanopaper with buckypaper to study the effect of fibre-fibre connections on mechanical properties.

Chapter 3

Experimental details

3.1 Materials

3.1.1 Printing paper

Printing paper (A4 80 gsm Harvest Copier White DPP) was purchased from Bates Office, UK and used for comparison. Printing paper specimens were tested in the machine direction (MD) which is the direction that the paper was running in the paper machine during manufacturing.

3.1.2 Nanofibrilated cellulose (NFC) nanofibres

NFC nanofibres were kindly provided by KTH, Stockholm (Sweden), and prepared according to a method published previously [31]. The NFC pulp were prepared from softwood pulp provided by Nordic Pulp and Paper (Sweden). First, the pulp was dispersed in water followed by a combination of enzymatic pretreatment and mechanical beating. The pretreated pulp was homogenized with a microfluidizer (M-110EH, Microfluidics Inc., USA). From this an aqueous suspension with a concentration of 1 wt.% NFC was obtained. The resulting NFC suspension was sealed and stored at the temperature of 4 °C.

3.1.3 Bacterial cellulose (BC)

BC pellicles were kindly provided by Huazhong University of Science and Technology (China). Gluconacetobacter xylinum (ATCC53582) was used to synthesize the BC. The BC pellicles were prepared according to the procedures described in [145]. The bacterium was cultured in a Hestrin and Schramm medium, which composed of 2 wt.% glucose, 0.5 wt.% peptone, 0.5 wt.% yeast extract, 0.27 wt.% disodium phosphate and 0.15 wt.% citric acid. Then, the mixture was statically incubated for 6 days at 26 °C and a BC pellicle was obtained. Finally, the BC pellicle was purified by first soaking it into distilled water for 2 days and then keeping it in a 1 wt.% NaOH solution for 30 min. Afterwards, the BC pellicle was washed in distilled water and was stored in distilled water of 4 °C. The resulting BC pellicle had a water content of around 97 wt.%.

3.1.4 Multi-walled carbon nanotubes (MWCNT)

MWCNT (AQUACYL^{TM} 0301) was provided by Nanocyl S.A. (Belgium). It contained about 3.0 wt.% MWCNTs of the Nanocyl® 7000 series. The MWCNTs were dispersed in water with the assistance of anionic surfactant (< 5 wt.% according to the data sheet). The dimensions of the nanotubes were 9.5 nm in average diameter and 1.5 μm in average length [146].

3.2 Preparation of nanopapers

3.2.1 Preparation of NFC nanopapers by suspension casting method (SC)

NFC nanopaper was prepared by mixing 0.2 g dry weight NFC and 40 mL distilled water in a homogeniser (IKA Ultra Turrax mixer D125 Basic, Germany) at a speed of 12000

rpm for 10 min. Then this suspension was degassed under the vacuum of 1 bar for 1hr and poured into a petri-dish and conditioned in an incubator at 37 °C for several days. Silica-gel particles were placed in the incubator to absorb the water vapour. The thickness (measured using a micrometer) of the resulting NFC nanopapers was around 30 μm.

3.2.2 Preparation of NFC nanopapers by hot pressing methods

For samples prepared using the hot pressing method, NFC pulp was first mixed with deionized water using a high speed mixer (IKA Ultra Turrax mixer D125 Basic, Germany) at the speed of 12000 rpm for 10 min to achieve a concentration of 0.2 wt.%. Then the diluted suspension was degassed for 1 hr followed by vacuum filtrated (0.65 μm, DVPP09050, Millipore, USA) until the formation of a wet cellulose cake with a water content of around 96 wt.%. The cake was stacked between filter paper and metal plates prior to hot pressing. Different pressures (0.5, 5 and 10 MPa) and temperatures (93 °C and 37 °C) were used. The samples prepared by the different methods are given names as listed in Table 3.1. The thickness was measured using a micrometer.

Table 3.1 Sample names and corresponding preparation methods

Sample names	**P05T93**	**P5T93**	**P10T93**	**P10T37**
Pressure (MPa)	0.5	5	10	10
Temperature (°C)	93	93	93	37
Thickness (μm)	70	62	58	60

3.2.3 Preparation of BC nanopapers

BC nanopaper was prepared by directly hot pressing the BC pellicle under 2 MPa at 93 ˚C for 5 hrs to obtain a dry film. The thickness (measured using a micrometer) of BC nanopapers ranged from 20-30 μm.

3.2.4 Preparation of buckypapers

Buckypaper was prepared as follows: first, the as received MWCNT suspension of around 0.2 g dry weight was diluted to a concentration of 0.2 wt.% in order to reduce the viscosity, which facilitated the removal of bubbles in the degassing process; then the suspension was degassed under the vacuum of 1 bar for 1 hr followed by vacuum filtrated using a filter membrane (0.1 μm VVLP09050, Millipore, USA) until the formation of a wet cake with a water content of around 80 wt.%; the wet cake was washed with deionized water to remove the surfactant; finally this MWCNT cake was hot pressed at the same conditions as the BC. The thickness (measured using a micrometer) of the buckypapers ranged from 80-100 μm.

3.3 Characterizations

3.3.1 Scanning electron microscopy (SEM)

Specimen surfaces and fracture surfaces were observed using SEM (FEI Inspector-F, the Netherlands). The specimens were coated with gold before imaging. Secondary electron detector was used for capturing images at 5 kV for cellulose nanopaper and buckypaper and 2 kV for printing paper.

3.3.2 Tensile testing

Rectangular specimens of 5 mm in width and 40 mm in length were preconditioned in a controlled environment (temperature of 23 °C and relative humidity (RH) of 50 %) for at least 24 hrs before testing to eliminate the effect of the difference in temperature and moisture content on the mechanical properties of specimens [4]. Tensile tests were then conducted using a universal testing machine (Instron 5586, UK) equipped with either a 1 kN or 100 N load cell. The specimens were gripped by the clamps with the long side of the specimen parallel to the loading direction. The testing distance was 20 mm and the test was performed at a crosshead speed of 2 mm/min. The reported values of mechanical properties were the average over at least six specimens.

3.3.3 Double edge notch tensile (DENT) testing

DENT tests were performed using an Instron 5586 (UK) with a 1 kN load cell at a crosshead speed of 0.2 mm/min. Rectangular specimens with 9 mm in width and with different notch lengths were preconditioned at the 23 °C and 50 % RH for at least 24 hrs before testing [4]. The notches were cut at each edge of the specimen using a surgical scalpel and the notch tip radii were around 50 μm (Figure 3.1). The specimens were gripped by the clamps in the direction where the long side of the specimens aligned in the loading direction and the notches were perpendicular to the loading direction. The reported values of mechanical properties were the average over at least six specimens.

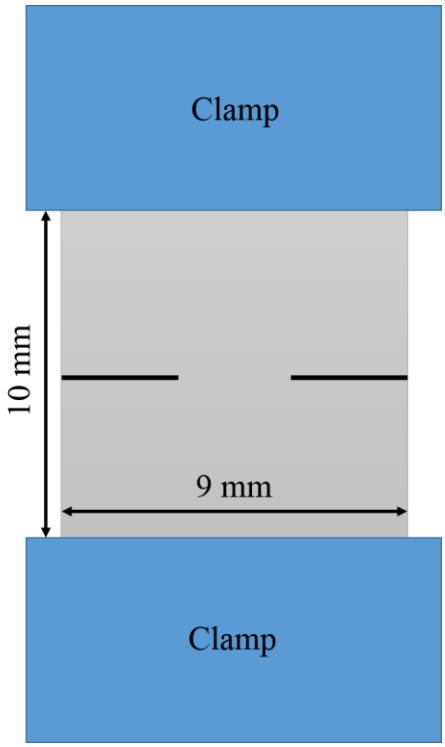

Figure 3.1 Schematic of loading configuration of notched specimens.

3.3.4 Repeated loading-unloading testing

Repeated loading-unloading tests were performed using an Instron 5586 equipped with either 1 kN or 100 N load cell. Dimensions of specimens and test speeds were similar to those for tensile testing. The peak load at each load cycle was increased incrementally, while a fully unloaded state was maintained for several minutes at the end of each cycle to allow strain recovery. Specimens were again conditioned at 23 $^{\circ}$C and 50 % RH for 24 hrs prior to testing [4].

3.3.5 Digital image correlation (DIC)

The 2D DIC technique was used to map the strain distribution in the specimens. In the case of notched specimens used in Chapter 4, the specimens were first spray coated with white paint. Then, graphite particles were used as speckles to achieve high contrast.

Graphite particles were first mixed with acetone followed by sonicated to obtain a homogenous suspension. This suspension was sprayed on the test samples using an airbrush at 30 psi pressure for 1 min with a distance of 10 cm between airbrush and sample surface. The size of the graphite particles was around 20 μm. Images were taken using a digital camera (MicroPublisher 3.3 RTV, QImaging, Canada) connected to an optical microscope at a magnification of 5x. The pixel size for each picture was 3.45 μm x 3.45 μm.

In the case of NFC unnotched specimens used in Chapter 5, the surface of a specimen was first spray coated with white paint as clear background. Then, black speckles of 100 μm were sprayed on the surface of a specimen to achieve good contrast. Images were taken by a CCD camera. The pixel size for each picture was 9.0 μm x 9.0 μm.

Either notched or unnotched specimens were loaded using a micro-tensile tester (Deben, UK) with a 200 N load cell. Length between the clamps was 10 mm while a test speed of 0.2 mm/min was used. The motion of the speckles during tensile testing was analysed by Ncorr, a Matlab programme developed by Justin Blaber from Georgia Institute of Technology (USA) [147]. At least two specimens were measured for either notched or unnotched sample to ensure the reliability of the results.

3.3.6 Wide angle X-ray diffraction (WAXD)

Crystallinity of cellulose nanofibres was determined from one-dimensional wide-angle X-ray diffraction (1D WAXD) patterns which were obtained using a Bragg-Brentano geometry X-ray diffractometer (X'Pert Pro, PANalytical, Netherlands) equipped with Cu/Kα radiation. The obtained spectra were composed of sharp peaks from crystallites

and broad background scattering from amorphous regions. Crystallinity of cellulose nanofibres was calculated using Equation 3.1 where the crystalline ($\sum$ Ac) and amorphous fractions (C) were obtained by multiple peak fitting the spectra into several sharp peaks and a broad band according to [148].

$$\chi_c = \frac{\sum Ac}{\sum Ac + \sum Aa} \times 100\% \qquad \text{Equation 3.1}$$

The crystalline preferred orientation of cellulose nanofibres was examined using two-dimensional wide-angle X-ray diffraction (2D WAXD) ring patterns, which were obtained using a transmission geometry on a single crystal X-ray diffractometer (Kappa ApexII Duo, Bruker AXS GmbH, Germany).

The Herman's orientation factors (*f*) were calculated from azimuthal intensity distribution graphs for the 200 equatorial reflection. The Herman's orientation factor describes the extent of crystallites axis relative to the axis of interest and can be derived from Equation 3.2 [72]:

$$f = \frac{3\langle \cos^2\varphi \rangle - 1}{2} \qquad \text{Equation 3.2}$$

$$\langle \cos^2\varphi \rangle = \frac{\sum_0^{\pi/2} I(\varphi) \sin\varphi \cos^2\varphi}{\sum_0^{\pi/2} I(\varphi) \sin\varphi}$$

where Φ represents the azimuthal angle, $I(\varphi)$ is the intensity along Debye-Scherer ring.

3.3.7 Polarized optical microscopy (POM)

Polarized optical microscopy (POM) was used to qualitatively examine the molecular orientation in the amorphous phase with strain. The examination of molecular anisotropy within the amorphous phase of a polymer placed between two crossed polarizers is based on the fact that a linearly polarized incident light beam travelling through a uniaxially oriented material is split into two orthogonally polarized rays (ordinary and extraordinary rays) with different phase velocity so that a phase difference (δ) can be identified between the rays emerging from the material [149]. If a light beam with intensity of I_0 is incident on an anisotropic material which is placed between two crossed polarizers, the transmitted light intensity I can be given by Equation 3.3 [150]:

$$I = I_0 \sin 2\varphi \sin^2 \frac{\delta}{2} \qquad \text{Equation 3.3}$$

where φ is the angle between the optical axis (assumed to be along straining direction) and the polarization axis of the polarizer. For an isotropic material, the optical image will be dark no matter which direction the sample is oriented. For an anisotropic material, the minimum transmitted light intensity (dark) can be obtained when the straining direction is along the direction of the polarizers (φ=0). Maximum intensity (bright) can be obtained when the angle between straining direction and the polarization direction of each polarizers is 45°.

Specimens were placed between two crossed polarizers where the direction of tension was aligned with one polarization direction (0°). Images were taken at a magnification of 5x. Anisotropy was identified if a specimen placed at an angle of 45° showed a brighter image than at 0°. A schematic of the test configuration is shown in Figure 3.2.

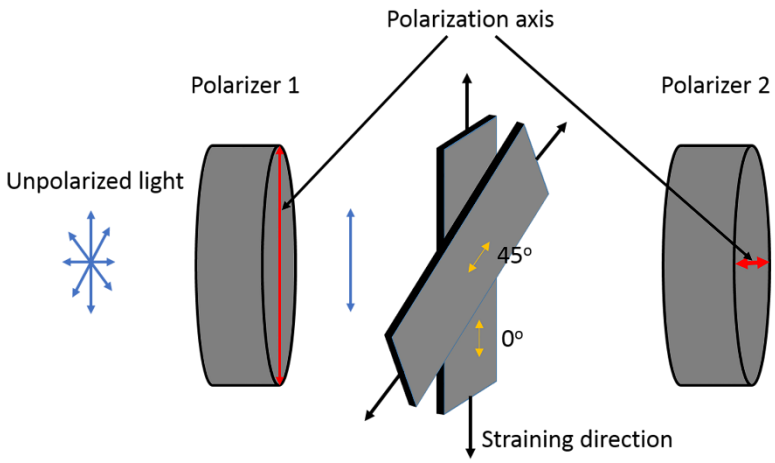

Figure 3.2 Schematic of the experimental test setup for polarized optical microscopy (POM).

3.3.8 In-situ Raman spectroscopy

The relationship between Raman band shifts and applied stresses and strains was investigated by recording Raman spectra using a Renishaw Raman Spectrometer (UK) equipped with a 633 nm Helium-Neon laser with a power of 35 mW during tensile testing. Specimens were mounted on a micro-tensile tester (Deben, UK) equipped with a 200 N load cell and loaded at a speed of 0.2 mm/min. Strain was incremented in 0.2 %, and at each step, specimens were excited by a laser beam. A 50× objective lens was used to focus the laser beam on the surface of the sample, while the spot size of the laser was around 2 μm. The wavenumbers used in the Raman spectra varied from 1050 and 1150 cm^{-1}. The Raman spectra were recorded using an exposure time of 10 s and 3 accumulations. The peak initially at 1095 cm^{-1} was determined by fitting the Raman band by a Lorentzian function.

3.3.9 Temperature dependence of dielectric spectra

For cellulose, the dielectric loss is primarily from overcoming friction during changes of chain conformation under altered applied electric fields. Therefore, a dielectric loss peak represents a state when the chain mobility does not match the alternation of the applied electric field. Hence, the temperature dependent dielectric spectra can be used to detect the relaxation mode of cellulose.

The temperature dependence of the dielectric loss was measured using a LCR meter (4284A, Agilent Technologies, USA) connected to a home-made furnace. The measurements were conducted in a temperature range of -180 to 245 °C at four different frequencies, 100 kHz, 10 kHz, 1000 Hz and 100 Hz.

3.3.10 Porosity

The density of cellulose nanopaper was determined by dividing the weight (air-dry weight, containing moisture) by the area and thickness of samples. Thickness was measured by using a micrometer. Porosity was estimated from Equation 3.4 using the density of nanopaper and density of cellulose which was taken as 1460 kg m^{-3} [13].

$$\text{Porosity} = \left(1 - \frac{\rho_{\text{nanopaper}}}{\rho_{\text{cellulose}}}\right) \text{x}100\ \% \qquad \text{Equation 3.4}$$

Chapter 4

Fracture properties of cellulose nanopapers

4.1 Introduction

To a large extent, the fracture properties of a material depends on its microstructure. Fracture mechanics of conventional paper has been extensively investigated [91-93, 98, 107, 109, 110, 114, 151] while the study on the fracture properties of cellulose nanopapers has been rarely reported.

In this chapter, the fracture properties of cellulose nanopapers are investigated using DENT tests with different notch sizes. Strain distribution in notched specimens at the notch tip before the initiation of cracking is provided. Cohesive zone models are established by iteratively comparing the simulation results with the experimental results and the cohesive parameters are extracted from those models. For comparison, printing paper is also tested and modelled to demonstrate the importance of fibre length. Buckypaper that based on carbon nanotubes connected through van der Waals forces, is also investigated to elaborate on the influence of inter-fibre network interactions.

4.2 Cohesive law

Cohesive law describes the relation between the traction and crack opening. The cohesive law of cellulose nanopaper is difficult to be determined precisely due to unstable crack propagation. Therefore, a general shape of a cohesive law for paper materials [114] is adopted in this study with some modification (Figure 4.1). The current cohesive law is divided into three stages based on the cohesive law shape (black lines in Figure 4.1). Conceptually, the first stage represents the opening of the initial notch tip prior to the appearance of damage in front of the notch tip (Stage 1). Then, a short stage with a small drop in stress (Stage 2) appears, corresponding to damage in the material (such as fibre fracture, fibre-fibre bond fracture and/or fibre slippage) and the formation of a fracture process zone at each notch tip. For further crack opening, the cohesive stress gradually decreases with respect to the crack opening until it approaches a critical value where the cohesive stress becomes zero (Stage 3). This corresponds to the pull-out of fibres or bridging fibres at the wake of the crack tip [115]. The hatched area below Stage 2 stands for the energy consumed by damage (G_d) of material while the one for Stage 3 represents energy dissipation by pull-out or fibre bridging at the wake of crack tip (G_b). The sum of these two energies is then the fracture energy (G_e) [101].

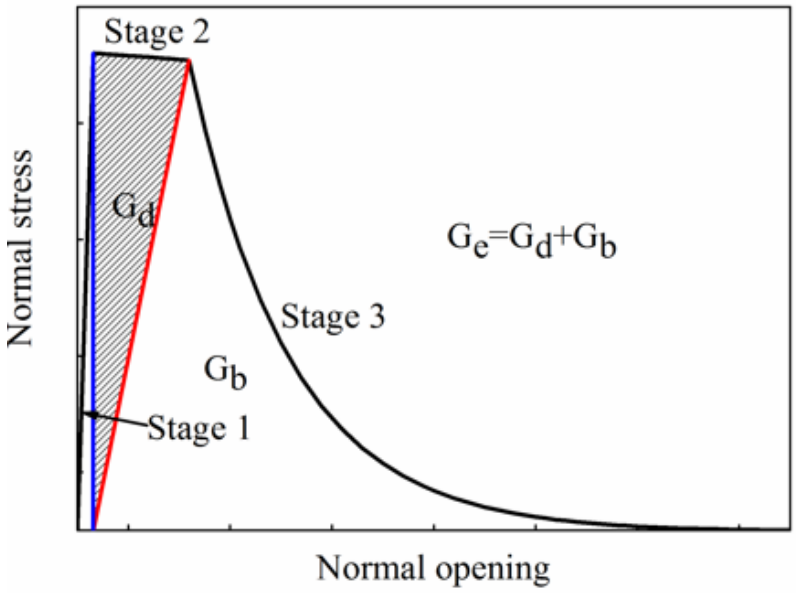

Figure 4.1 Schematic of the cohesive law.

4.3 Modelling the fracture of nanopaper using cohesive law

The fracture process was modelled by the finite element (FE) method using Abaqus software, version 6.11 [152]. The boundary conditions of the model are shown in Figure 4.2. The movement of the whole bottom edge of the specimen in the y direction and the movement of the leftmost point at the bottom edge in the x direction was constrained so that the bottom edge of the specimen could not move. Stretching of the specimen in the y direction was applied using displacement control at the top edge of the specimen. The cohesive zone (red area in Figure 4.2) was assigned to be very thin and was placed between the two notches and was modelled by 4-noded two dimensional cohesive elements while the area outside the cohesive zone (blue area in Figure 4.2) was constituted of 4-noded linear plane stress elements. The model was assumed elastic for NFC nanopaper and elastic-plastic for printing paper and buckypaper for the reason of ductile failure behaviour of the latter two. The plasticity parameters used in these models were obtained from repeated loading-unloading tests. The simulation was performed by a

quasi-static solution using explicit solver since implicit FE method may cause convergence problems [153].

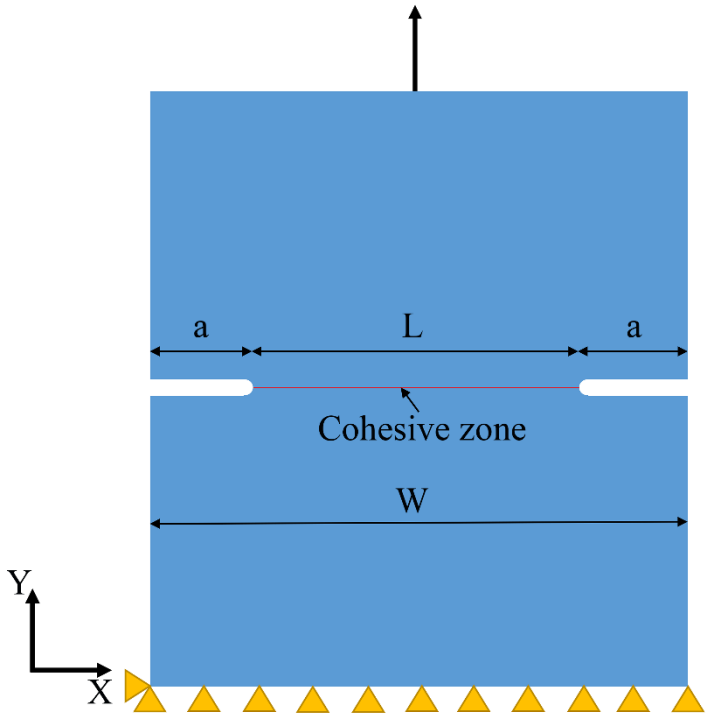

Figure 4.2 Schematic of the boundary conditions of the model.

4.4 Results and discussion

In this chapter, the NFC nanopapers were prepared by suspension casting method as described in Chapter 3. BC nanopaper and buckypaper were prepared as described in Chapter 3.

4.4.1 Microstructure

Figure 4.3 shows the morphology of NFC and BC nanopaper, printing paper and MWCNT buckypaper. NFC nanopaper shows a dense microstructure. The diameter of the NFC nanofibres are only several tens of nanometers. BC nanopaper shows greater porosity and thicker nanofibres than NFC nanopaper. For comparison, the morphologies

of printing paper and buckypaper are also shown. Printing paper shows much thicker fibres than nanofibres in those nanopapers. Buckypaper also shows porous structure. The diameter of the MWCNTs is similar to that of cellulose nanofibres.

Fibre-fibre interactions are also variable among these materials. NFC and BC nanofibres are of nanometer-size which gives them a high specific surface area and a high number of hydroxyl groups at the fibre surface. These nanofibres are connected into a network by numerous hydrogen bonds preventing the slippage of such cellulose nanofibres. In addition, the fibre-fibre interaction in BC nanopaper is speculated to be stronger than that in NFC nanopaper. This is because the ribbon shaped BC nanofibres can generate relative large crossing area at each fibre-fibre intersection while the round shaped NFC nanofibres form relative small crossing area [75]. Printing paper has much bigger fibres which result in a smaller specific surface area, fewer hydroxyl groups, and consequently weaker inter-fibre interactions. MWCNT based buckypaper has no polar groups at the surface, leading to fibre-fibre interactions governed by weak van der Waals force.

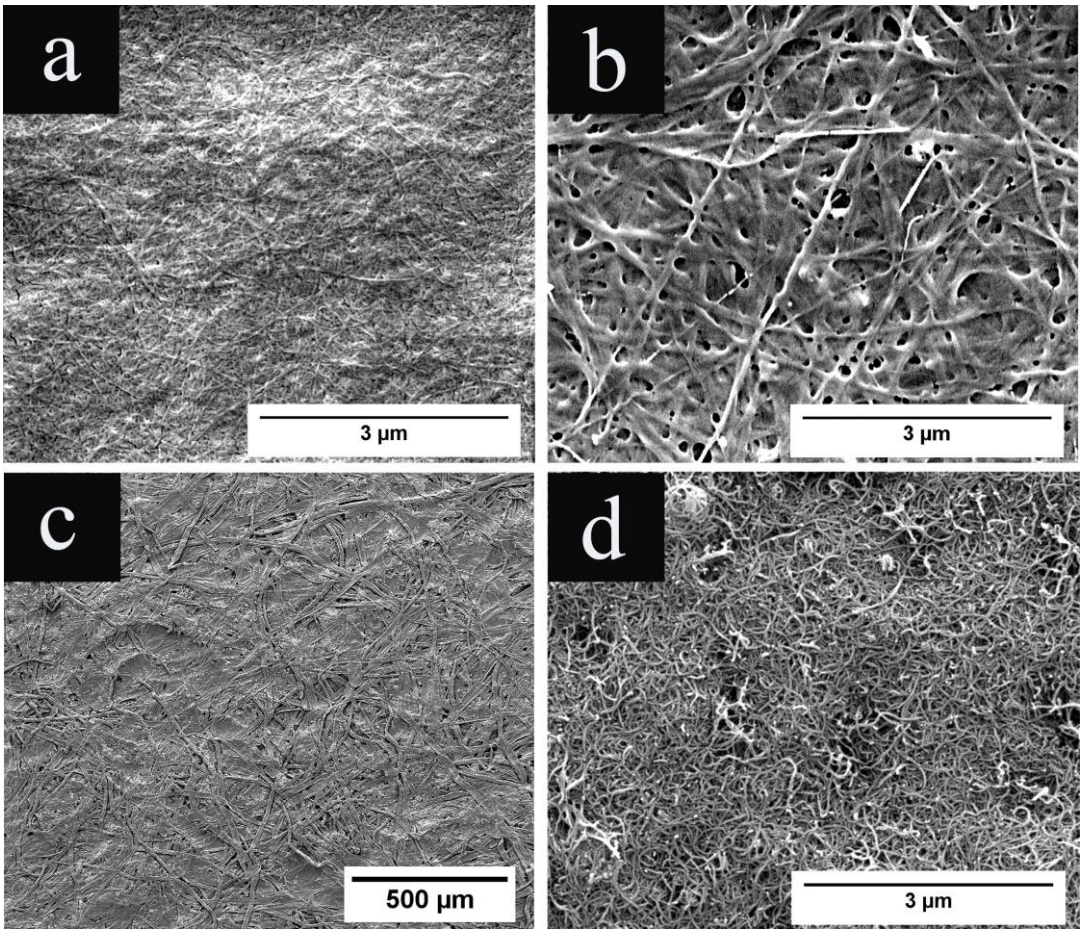

Figure 4.3 Morphology of (a) NFC nanopaper, (b) BC nanopaper, (c) printing paper (please note the difference in magnification) and (d) buckypaper.

4.4.2 Mechanical testing

The mechanical properties obtained from tensile testing on specimens without notches or unnotched specimens are shown in Figure 4.4 and listed in Table 4.1. The stress-strain curves of NFC and BC nanopaper show elastic behaviour followed by an inelastic stage. NFC nanopaper exhibits a high strength (196 ± 22 MPa), elastic modulus (10.4 ± 0.9 GPa) as well as a high strain at peak stress (4.96 ± 0.26 %). BC nanopaper shows similar values of elastic modulus (9.6 ± 1.5 GPa) but a lower tensile strength (151 ± 21 MPa) and strain at peak stress (2.44 ± 0.41 %) than NFC nanopaper due to the higher porosity and the looser structure. Clearly, both NFC and BC nanopaper are much stronger than

conventional paper and buckypaper. This is because the structures of NFC and BC nanopapers are denser than printing paper and buckypaper. In addition, the fibre-fibre connection (hydrogen bonding) in NFC and BC nanopapers are stronger than that in buckypaper (van der Waals force). Compared with printing paper, NFC and BC nanopapers can also form more hydrogen bonds due to the higher specific surface area of the cellulose nanofibres.

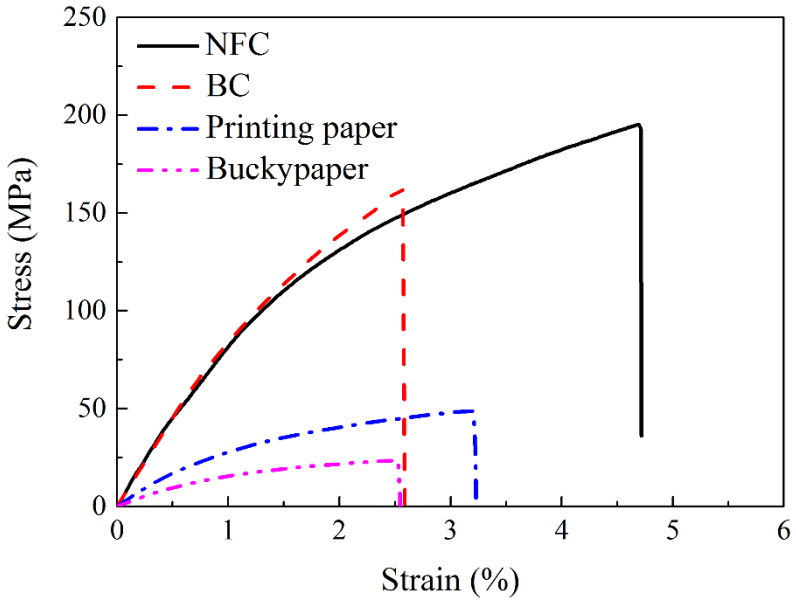

Figure 4.4 Stress-strain curves of unnotched tensile tests of NFC and BC nanopapers, printing paper and buckypaper.

Figure 4.5 shows the DENT test results of NFC and BC nanopaper, printing paper and buckypaper. Here, stress is calculated based on the ligament area which is the reduced area between the two notches. The notched NFC and BC nanopapers still show higher strength than printing paper. Compared with unnotched specimens, strength deteriorates dramatically for NFC nanopaper, BC nanopaper and buckypaper when notches are placed at both edges. It is worth noting that double notched NFC and BC nanopapers show

relative elastic behaviour prior to failure. On the contrary, notched printing paper and buckypaper show apparent inelastic behaviour.

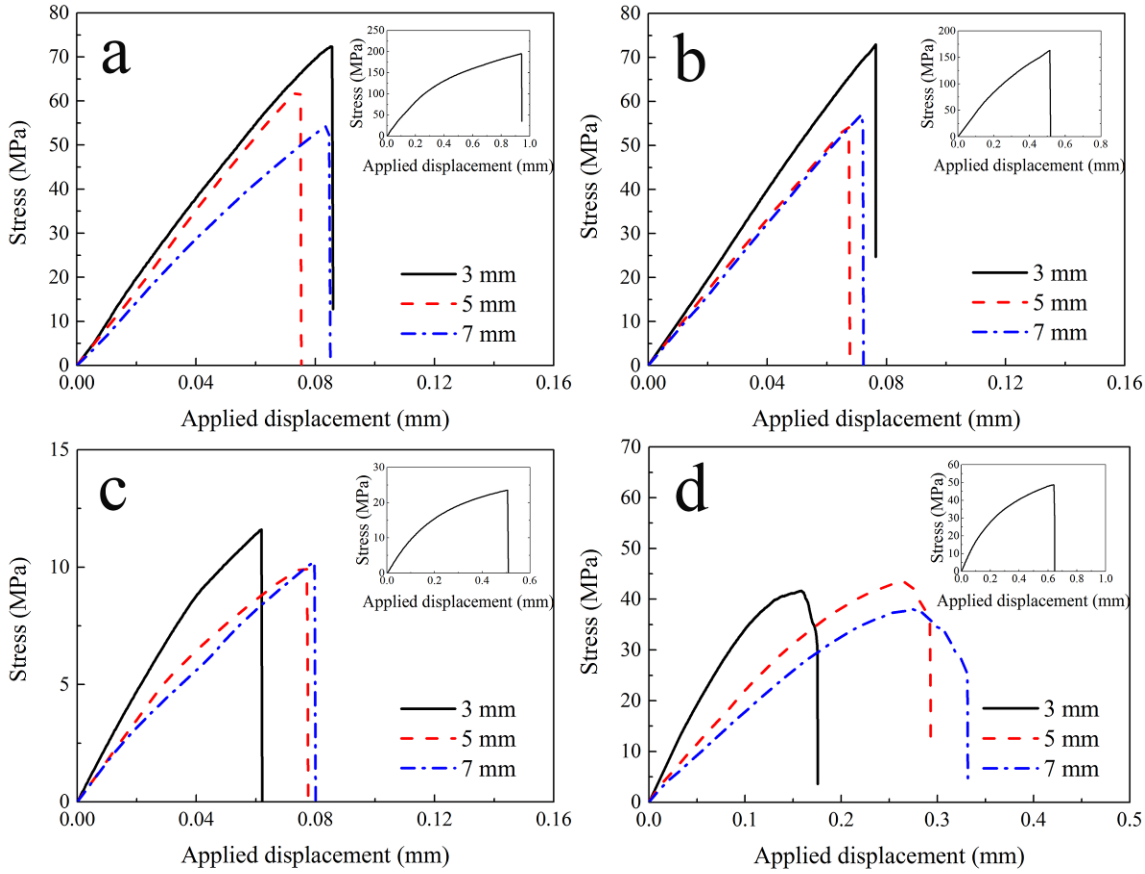

Figure 4.5 Notched stress-applied displacement curves obtained from DENT tests for (a) NFC nanopaper, (b) BC nanopaper, (c) buckypaper and (d) printing paper at different ligament lengths. The inset images show the unnotched stress-applied displacement curves for comparison.

The mechanical properties of NFC and BC nanopaper with different notch sizes are also examined (Figure 4.5 and Table 4.1). Here, the size of the notch is represented by its ligament length. It was found that the strength of NFC and BC nanopaper is not sensitive to ligament length, allowing for the scatter in brittle fracture data. There is no obvious

difference in strength between NFC and BC nanopaper. For printing paper and buckypaper, the strength of the notched samples are also not sensitive to ligament length. The insensitivity of all the materials to the ligament length is due to a stress delocalization mechanism at the notch tip, which is further explained in Section 4.4.4.

Table 4.1 Fracture strength from DENT test as well as tensile test data of unnotched specimens

	Ligament length (mm)	**Fracture strength (MPa)**
NFC	3	65.8 (5.4)
	5	60.0 (6.4)
	7	57.7 (3.5)
	Unnotched	195.6 (22.5)
BC	3	73.8 (9.1)
	5	53.4 (8.3)
	7	61.5 (6.9)
	Unnotched	150.9 (21.1)
Buckypaper	3	11.8 (1.0)
	5	9.7 (0.9)
	7	9.5 (1.4)
	Unnotched	23.3 (1.5)
Printing paper	3	43.5 (2.5)
	5	42.1 (2.2)
	7	39.3 (1.5)
	Unnotched	50.2 (1.8)

Notch sensitivity describes the strength sensitivity of the sample relative to notch length. It reflects the ability of the notched sample to relieve the concentrated stress at the notch tip. The notch sensitivity of notched cellulose nanopapers can be examined using a model developed by Suo et al. [154]:

$$\frac{\sigma_f}{\sigma_0} = [\left(1 - \frac{a}{w'}\right)^{-2} + \pi F^2 \frac{a}{\Gamma E'/\sigma_0^2}]^{-1/2} \qquad \text{Equation 4.1}$$

where σ_f is the fracture strength of the notched sample, σ_0 is the strength of an unnotched sample, a is the notch length, w' is the half width of the sample, F is the dimensionless stress intensity solution related to testing configuration, Γ is the energy to separate unit area at crack and E' is the Young's modulus for plane stress. A dimensionless notch sensitivity parameter can be extract from the second item in Equation 4.1 as shown below [155]:

$$\alpha = \frac{a}{\Gamma E' / \sigma_0^2} \qquad \text{Equation 4.2}$$

The sample can be considered as notch insensitive when α approaches 0 where stress concentrations are completely relieved (notch ductile). On the contrary, the sample is brittle and notch sensitive when α is very large (notch brittle). Figure 4.6 shows the relationship between the normalized strength of notched NFC nanopapers (σ/σ_0) and the relative notch length (a/w) as well as the theoretical predictions for notch sensitive and notch insensitive samples. It can be seen that the normalized strength of NFC nanopapers lies between notch sensitive and insensitive, which indicates that NFC nanopapers can partially relieve the localized stress concentrations at the notch tip.

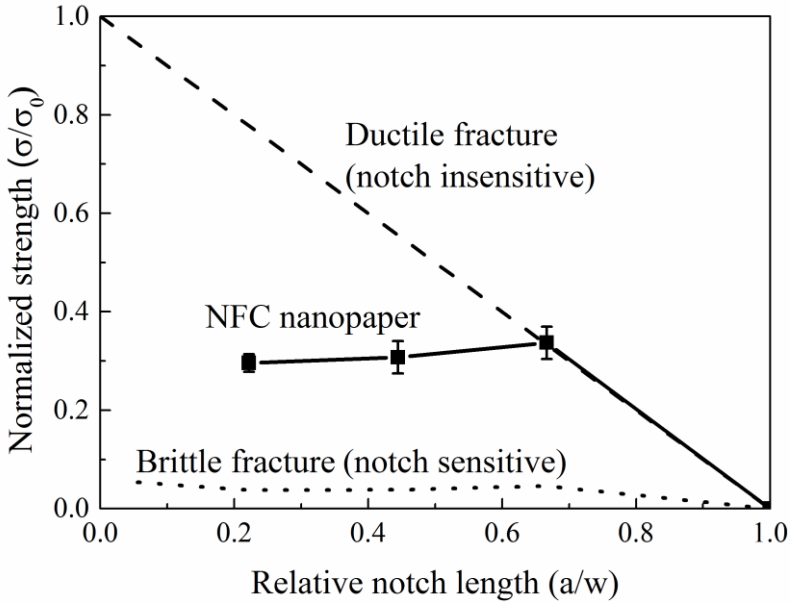

Figure 4.6 Normalized strength of NFC against relative notch length together with the theoretical predictions.

4.4.3 Cohesive zone model

The general shape of the cohesive law used in this thesis stems from the one measured experimentally for conventional paper materials [114]. Cohesive zone parameters such as cohesive strength, critical crack opening and fracture energy can be obtained by iteratively tailoring cohesive parameters and comparing the stress-applied displacement curves derived from simulation and experiment.

Cohesive zone models for NFC nanopaper, printing paper and buckypaper with a ligament length of 3 mm were evaluated. For each material, the experiment data were bounded by the simulation results from the cohesive model with different cohesive parameters. In addition, the average of the experimental data was also simulated and the result is termed ‘best fit’. The simulation data and DENT test curves are plotted in Figure 4.7. It can be seen that the simulated stress-applied displacement relationship for NFC is

linear and elastic while inelasticity appears in the simulation results for printing paper and buckypaper. Plasticity parameters in the models of printing paper and buckypaper were, as mentioned earlier, obtained from repeated loading-unloading tests by measuring the peak stress (or yield stress) and plastic strain for each cycle. The plastic strain is defined as the unrecoverable strain after the samples are unloaded. It can be observed in Figure 4.8 that plastic strain increases approximately exponentially with yield stress. An extra data point (black circle in Figure 4.8) is predicted by fitting the experimental data exponentially for printing paper in order to cover the whole stress range in the model.

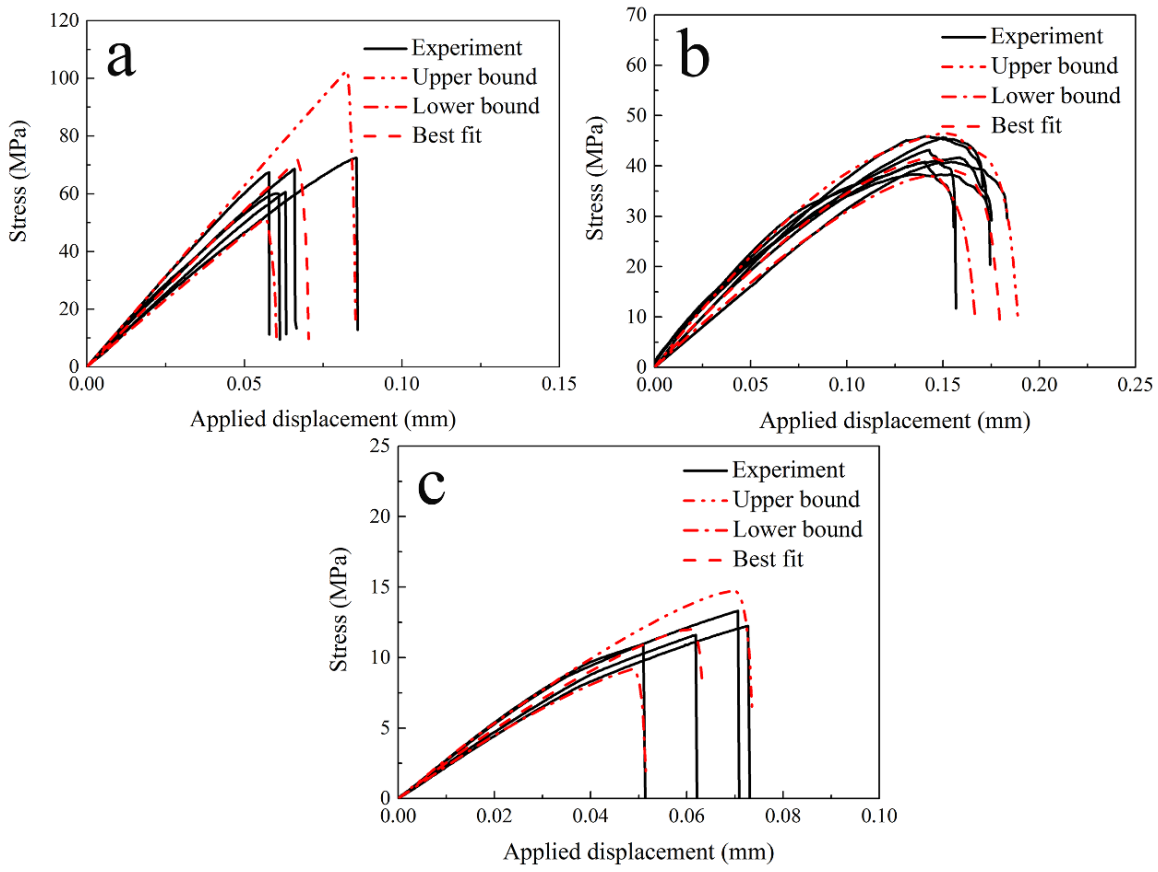

Figure 4.7 Stress-applied displacement curves as obtained from experiments together with simulations for (a) notched NFC nanopaper, (b) printing paper, and (c) MWCNT buckypaper with a ligament length of 3 mm.

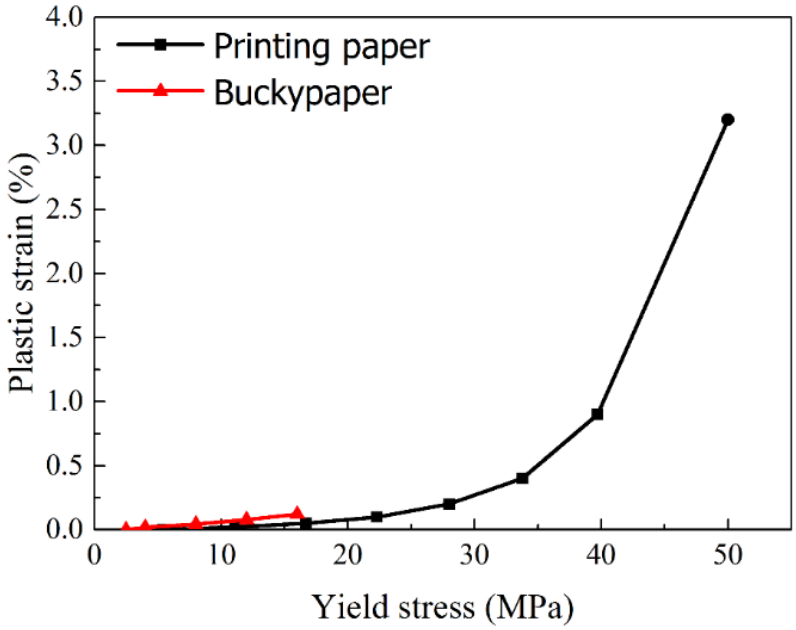

Figure 4.8 Plasticity parameters from repeated loading-unloading tests.

In the cohesive zone model, the cohesive law describes the stress-crack opening relationship in the cohesive zone. The cohesive laws of best fit curves for NFC nanopaper, printing paper and buckypaper are plotted in Figure 4.9 and the corresponding cohesive parameters are listed in Table 4.2. NFC nanopaper has the highest cohesive strength, because of the combination of high mechanical properties of NFC nanofibres and strong fibre-fibre interations. The critical crack opening in the cohesive zone of NFC nanopaper is the lowest of all papers, which indicates unstable failure with small contributions from mechanisms such as fibre bridging and fibre pull-out. This is in agreement with the fact that the observed fracture of NFC nanopaper is relative brittle. The absence of fibre pull-out mechanisms in NFC nanopaper is associated with the short length of NFC nanofibres in combination with strong inter-fibre interactions. Buckypaper has similar fibre dimensions as NFC nanopaper but much weaker inter-fibre interactions which results in a low cohesive strength. It is worth noting that carbon nanotubes are unlikely to fracture under tension since fibre-fibre interactions are far weaker than the intrinsic strength of

nanotubes. Thus, the failure of buckypaper can be completely ascribed to inter-fibre bond fracture, inter-fibre slippage and fibre pull-out. In fact, the lowest cohesive strength for buckypaper indicates that fibre slippage and pull-out mechanisms are already initiated at very low stresses. Printing paper shows a medium peak strength resulting from weaker fibres and less inter-fibre interactions than NFC nanopaper. It is worth noting that printing paper has the largest critical crack opening which indicates large scale fibre pull-out as a result of the long fibres in this material. The fracture energies (G_e) of all the materials are listed in Table 4.2. The fracture energy of NFC nanopaper is only one third of that of printing paper. The difference in fracture energy between printing paper and nanopaper primarily originates from differences in energy consumed by overcoming inter-fibre bonding and friction during fibre pull-out processes (G_b). The difference in failure mechanisms is confirmed by fracture surface images shown in Figure 4.10, with only tiny NFC nanofibres protruding from the fracture surface. These short protruding nanofibres in NFC imply that little energy is consumed by pull-out mechanisms. BC nanopaper and buckypaper also show such short protruding nanofibres, which indicates a smaller contribution to fracture energy from pull-out mechanisms. Printing paper on the other hand shows long protruding fibres suggesting massive fibre pull-out resulting in more energy absorption. The fracture energy of buckypaper is the lowest since here fracture is dominated by slippage of short MWCNTs overcoming weak van der Waals interactions.

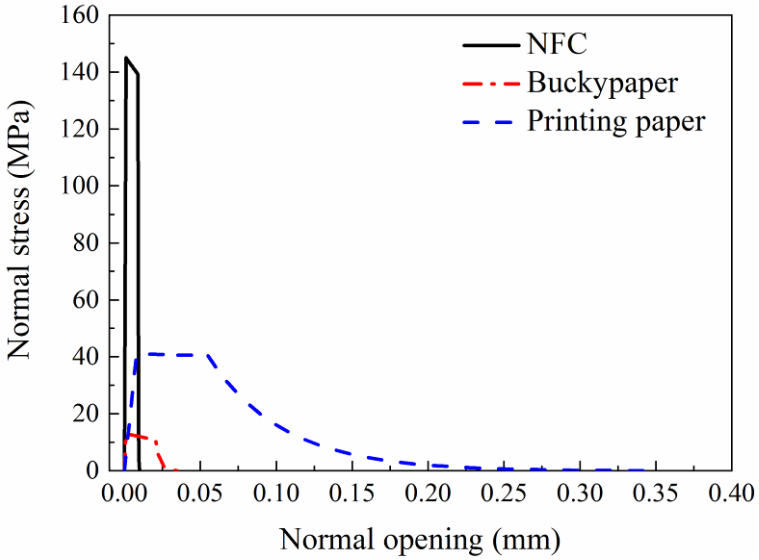

Figure 4.9 Cohesive laws extracted from cohesive zone models for NFC nanopaper, printing paper and buckypaper.

Table 4.2 Cohesive parameters for NFC nanopaper, printing paper and buckypaper

		G_d (kJ/m^2)	G_b (kJ/m^2)	G_e (kJ/m^2)	Cohesive strength (MPa)	Critical crack opening (mm)
NFC nanopaper	Lower bound	0.35	0.36	0.71	100	0.045
	Upper bound	0.84	0.95	1.79	280	0.010
	Best fit	0.58	0.57	1.15	145	0.010
Printing paper	Lower bound	0.63	2.53	3.16	38	0.350
	Upper bound	1.13	3.26	4.38	46	1.000
	Best fit	0.96	2.91	3.87	41	0.350
Bucky paper	Lower bound	0.07	0.07	0.14	10	0.041
	Upper bound	0.18	0.28	0.46	16	0.057
	Best fit	0.13	0.13	0.26	13	0.055

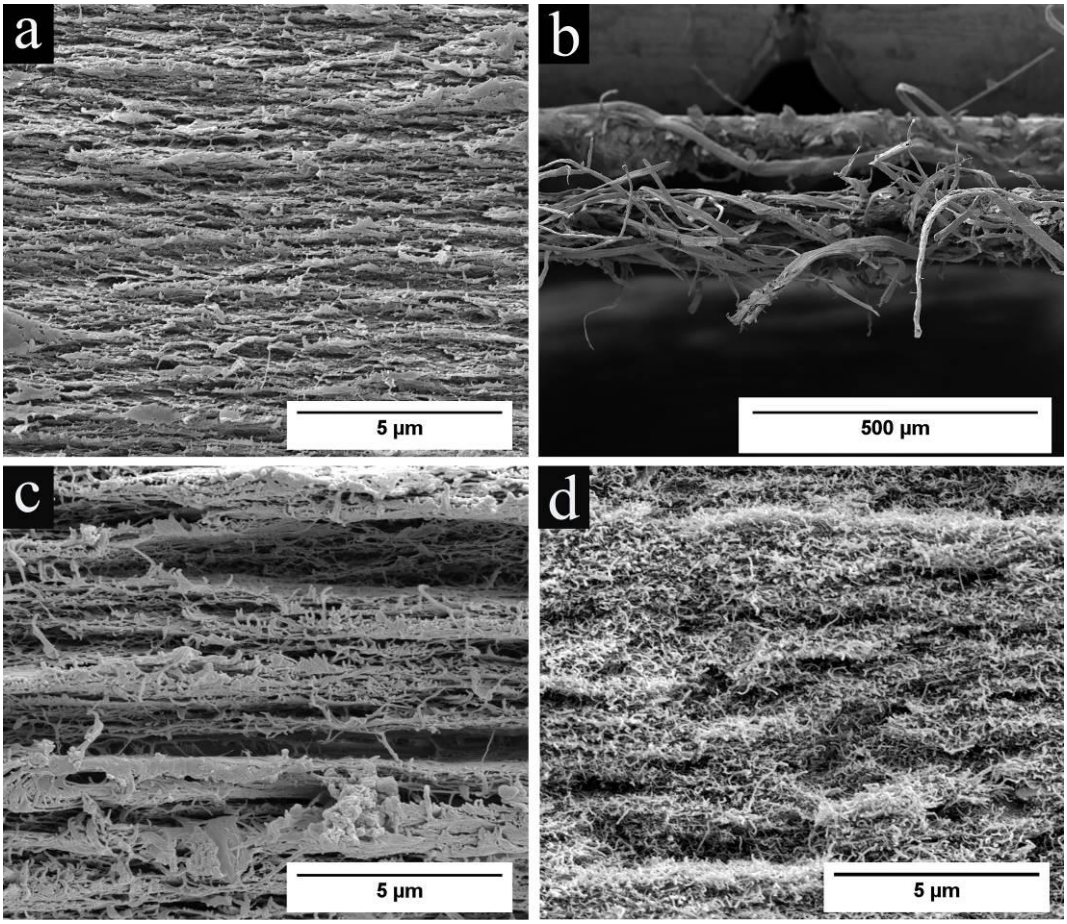

Figure 4.10 Fracture surfaces of (a) notched NFC nanopaper, (b) printing paper, (c) BC nanopaper and (d) buckypaper.

The above cohesive parameters of NFC nanopaper with a ligament length of 3 mm are used to predict the stress-applied displacement curves of notched NFC nanopaper with a ligament length of 5 mm. Figure 4.11 shows that the stress-applied displacement curve from simulation fits well with the experimental data for notched NFC nanopaper with a ligament length of 5 mm. The simulated strength is 58 MPa which is close to the corresponding average value in the experiment. This gives confidence on the extracted cohesive law parameters. The fracture process lengths in cohesive zone models between samples with different ligament lengths are compared. Figure 4.12 presents the relation between crack extension and applied displacement. It can be seen that damage initiation

is earlier in the model with a ligament length of 3 mm than in the model with a ligament length of 5 mm, indicating that deeper notches will cause higher stress concentration, resulting in early damage at the notch tip. The displacement from the initiation of damage to the initiation of crack propagation shows a higher value in the model with ligament length of 5 mm. This indicates that samples with longer ligaments can tolerate progressive damage (without the initiation of crack propagation) in a larger deformation range. Figure 4.13 shows that stress decreases with crack extension (crosses mean that catastrophic failure takes place). The model with a ligament length of 3 mm shows higher stresses both at the initiation of crack propagation and at unstable crack propagation than the model with a ligament length of 5 mm. The lower stress at the initiation of crack propagation means that longer ligament lengths are more capable of tolerating progressive damage since the more progressive damage before crack propagation, the lower the stress at the initiation of crack propagation. The lower stress at unstable fracture and longer crack extension before catastrophic failure demonstrate that longer ligament lengths tend to allow more stable crack propagation.

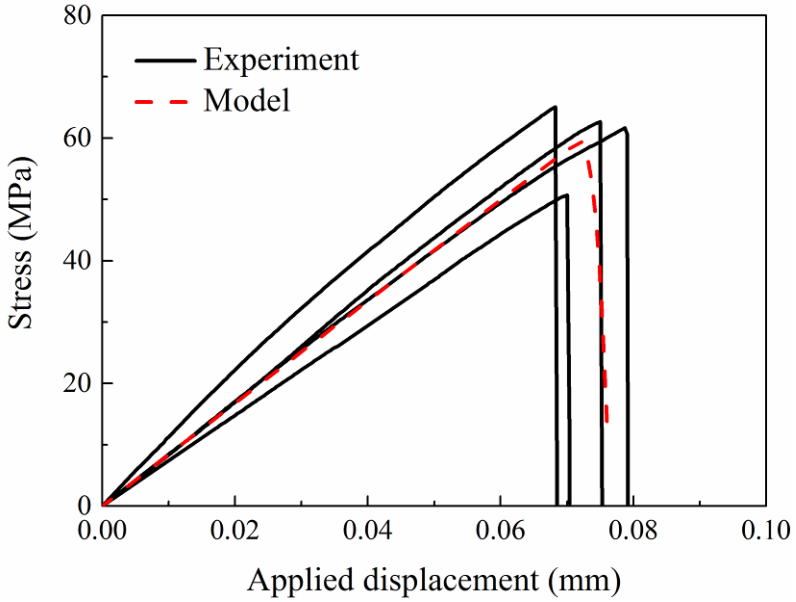

Figure 4.11 Stress-applied displacement curves as obtained from experiments together with simulations for notched NFC nanopaper with a ligament length of 5 mm.

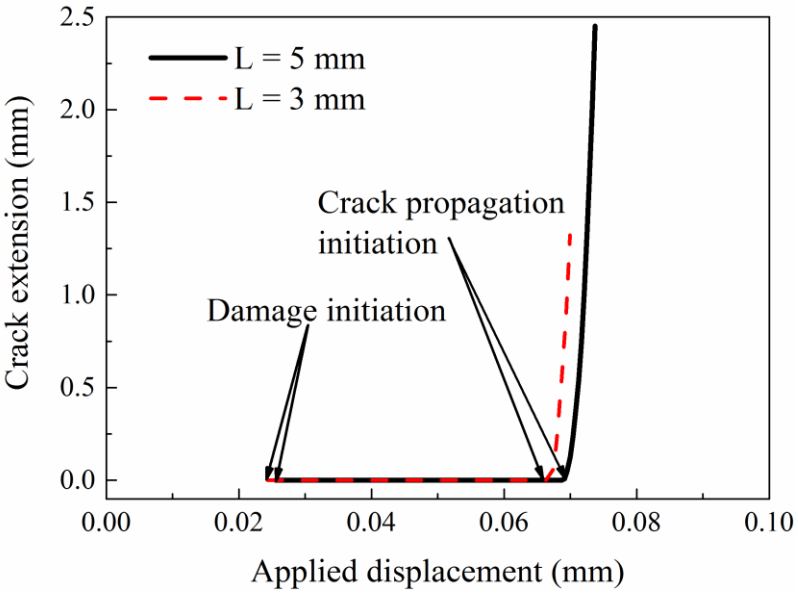

Figure 4.12 Crack extension against applied displacement in cohesive zone models with ligament lengths of 3 and 5 mm.

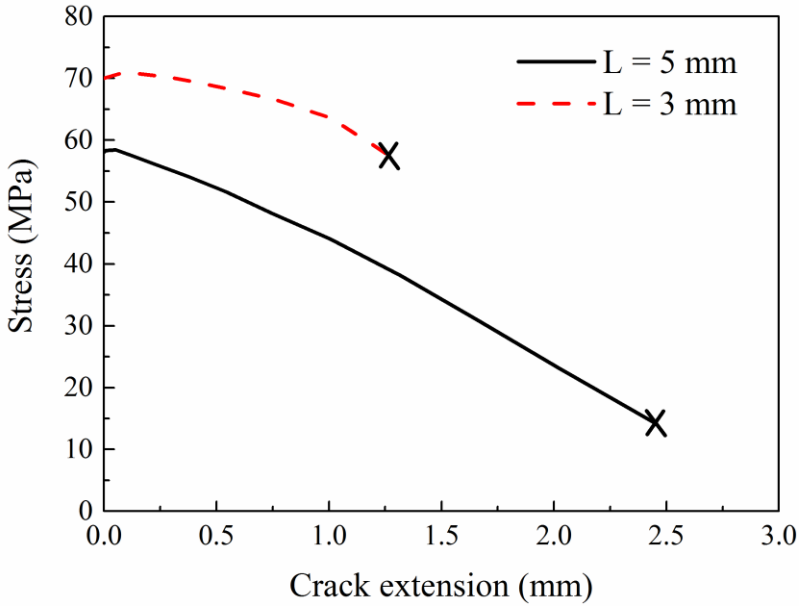

Figure 4.13 Stress in the cohesive zone against crack extension for models with ligament lengths of 3 and 5 mm.

4.4.4 Strain mapping at the notch tip

Since the strength of the DENT cellulose nanopaper samples is insensitive to notch length, it is necessary to examine the stress field in these DENT samples which can be represented by a strain field. The strain distribution of the cellulose nanopaper can be obtained by taking advantage of 2D digital image correlation (DIC) techniques by which the motion of localized particles at the surface of a specimen can be tracked. As a result, the strain distribution can be determined by the ensemble of this localized motion.

The strain distribution in notched NFC nanopaper close to its failure strain (0.6 %) is shown in Figure 4.14(a). It shows only a small strain concentration region at the notch tip. It is worth noting that more than one place of stress localization can be observed in notched cellulose nanopaper (multiple strain concentration centers are shown in Figure 4.14(a)), which is indicative of a stress delocalization mechanism. In cellulose nanopaper,

extended nanofibres can carry load along their length like wires in tension and transfer the load between nanofibres through inter-fibre connections. The extended nanofibres are located in different regions and can be distant from the notch tip. As a result, concentrated stress can be transferred away from the notch tip through extended nanofibres and inter-fibre connections so that stress is distributed along these nanofibres instead of concentrated around the notch tip. The strength of DENT samples with different notch sizes depends on the amount of cellulose nanofibres sharing the load in the network. This stress delocalization mechanism is most apparent in printing paper (Figure 4.15(b)) where multiple strain concentration centers (dark red regions) are seen far away from the notch tip. For comparison, the strain distribution in NFC nanopaper originating from the cohesive zone model for the same strain is shown in Figure 4.14(b). It represents the strain distribution predicted from the viewpoint of a homogeneous material and shows a large strain concentration region radiating out to the opposing notch. Apparently, this prediction overestimates the size of the strain concentration region. The stress delocalization phenomena in fibrous networks corroborates the numerical analysis where a diffused plastic zone was observed in the network model [118]. Hence, the cohesive zone model is not valid in terms of the evaluation of the strain distribution in fibrous networks.

Figure 4.15(b) shows the strain field of printing paper close to final failure, revealing a large strain concentration region. Printing paper has long fibres that can cross the ligament area ahead of the notch and connect with fibres far from the notch tip. These fibres can transfer the concentrated stress at the crack tip to a far field not just by inter-fibre connections but also by the long fibres themselves, which results in a large strain concentration region.

The influence of inter-fibre interactions on strain concentrations is investigated by comparing cellulose nanopaper with buckypaper. Figure 4.15(c) shows the strain field in notched buckypaper close to final failure. Strain concentrations near the notch tips are barely visible in buckypaper due to the weak van der Waals interactions between MWCNTs.

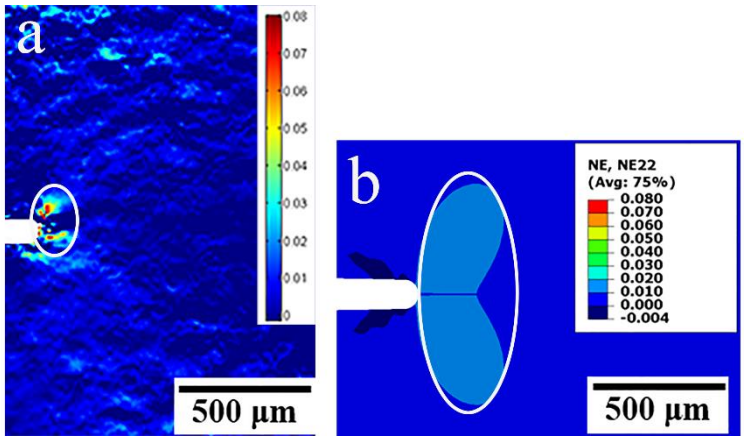

Figure 4.14 Strain distribution in NFC nanopaper (a) from 2D DIC experiments and (b) from cohesive zone modelling. Strain concentration regions are marked by white circles.

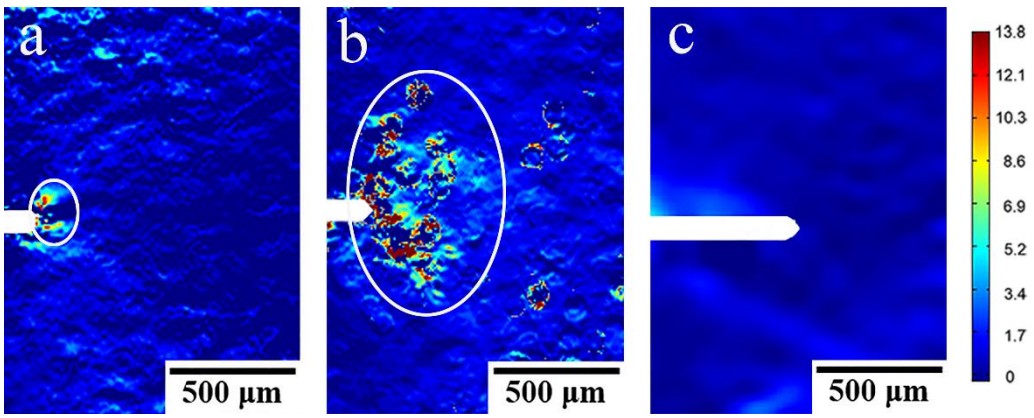

Figure 4.15 Strain distribution in (a) NFC nanopaper, (b) printing paper and (c) buckypaper. The numbers in the far right bar represent the degree of strain concentration.

4.5 Conclusions

The fracture properties of cellulose nanopaper were investigated in terms of notch dependence, cohesive law parameters (cohesive strength, critical crack opening and fracture energy) as well as strain distribution at the notch tip. For comparison, printing paper and MWCNT based buckypaper were used to investigate the influence of fibre length and inter-fibre interactions on fracture properties, respectively. The DENT test results showed that the strengths of cellulose nanopaper, printing paper and buckypaper were not sensitive to notch length. Notch sensitivity results showed that NFC nanopapers displayed between completely notch sensitive and insensitive conditions and that the concentrated stress at the notch tip could be partially relieved by the network structure. The fracture processes of cellulose nanopaper and printing paper were simulated by cohesive zone models where results showed that cellulose nanopaper had a lower fracture energy than printing paper due to the near absence of fibre pull-out mechanisms. These cohesive zone models are valid for samples with different ligament lengths and were used to compare the fracture processes between samples with different ligament lengths. Longer ligaments led to progressive damage and facilitated stable crack propagation. The strain field at the notch tip in cellulose nanopaper indicated a stress delocalization mechanism which results in a low notch sensitivity for different notch lengths. By comparing the strain field of cellulose nanopaper as measured by 2D DIC with printing paper and buckypaper, it is suggested that fibre length and fibre-fibre interactions are important to such stress delocalization mechanism.

Chapter 5

Inelastic deformation mechanisms in cellulose nanopapers

5.1 Introduction

Typical stress-strain curves of cellulose nanopaper show an elastic region followed by a long inelastic region where the toughness primarily originates from. Therefore, the exploration of toughening mechanisms in cellulose nanopaper should focus on mechanisms of inelasticity in such nanopapers. The majority of the proposed mechanisms are pointing towards inter-fibre interactions, while only few reports consider properties of the individual cellulose nanofibre. Cellulose nanofibres are composed of long molecules, which are organized in crystalline and amorphous regions [84, 85]. Therefore there is a distinct possibility that the inelastic behaviour in these materials is related to the same phenomena that promote inelastic behaviour in semi-crystalline polymers. This chapter will therefore focus on mechanisms of inelasticity in cellulose nanopaper at different length scales. First, the strain distribution in cellulose nanopaper was characterized using a 2-dimensional digital image correlation (2D DIC) technique. Next, the possibility of inter-fibre slippage between individual cellulose nanofibres and subsequent reorientation of nanofibres during the inelastic stage were examined. Finally,

the relationship between local mobility of cellulose chain segments and the inelastic behaviour was investigated.

5.2 Results and discussion

Cellulose nanopapers used in this chapter were prepared by suspension casting method described in Chapter 3. Figure 5.1 shows a typical stress-strain curve of cellulose nanopaper. It can be seen that cellulose nanopaper deforms elastically until a strain of around 1 %, after which a long inelastic region occurs until final failure. The strain distribution in the nanopaper as measured by 2D DIC at different loading stages are shown as insets. The strain distribution image in the elastic region shows a relative uniform distribution of strain in the nanopaper plane, while a less uniform strain distribution exists in the inelastic region. At the latter stage, some nanofibres are less loaded than others with strain values at every position in the nanopaper exceeding the value at the transition from elastic to inelastic region (the inset at the strain of around 3 % in Figure 5.1). This indicates that inelasticity takes place throughout the whole cellulose nanopaper when the specimen was loaded beyond the strain of around 3 %.

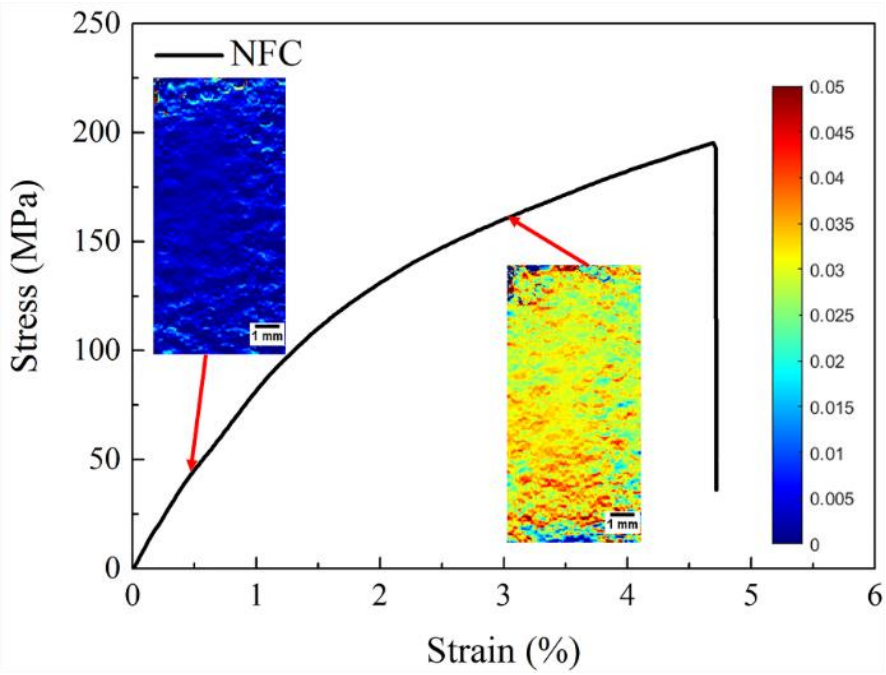

Figure 5.1 Stress-strain curve of cellulose nanopaper. The insets are 2D DIC strain distribution plots at different levels of strain. The degree of strain is indicated by the far right bar in the graph.

Repeated loading-unloading testing was carried out to investigate the effect of inelastic loading history on Young's modulus and yield stress (Figure 5.2(a)). Here, the words 'plastic deformation' and 'yield stress' are used only based on phenomenological interpretation since the mechanisms of inelastic deformation remain unclear. The sample was first strained in the elastic region in order to obtain the initial Young's modulus. Loading cycles 1 and 2 were performed in the elastic range and the development of Young's modulus with number of cycles is shown in Figure 5.2(b). The Young's modulus at cycle 1 and 2 is around 10 GPa. Subsequent loading cycles were performed in the inelastic region and it is shown that the Young's modulus remains constant for all cycles. Furthermore, the values of Young's modulus are similar in both the elastic and inelastic regions. The values of yield stress (determined from 0.2 % offset yield point) of the cellulose nanopaper against loading cycles are plotted in Figure 5.2(c). Also yield stress

is fairly independent of loading cycle and did not show any trend. The results of these repeated loading-unloading tests indicate that inelastic deformation has no apparent effect on Young's modulus and yield stress. Therefore, the occurrence of large scale nanofibre reorientation in the inelastic region is not very plausible as this would affect these properties.

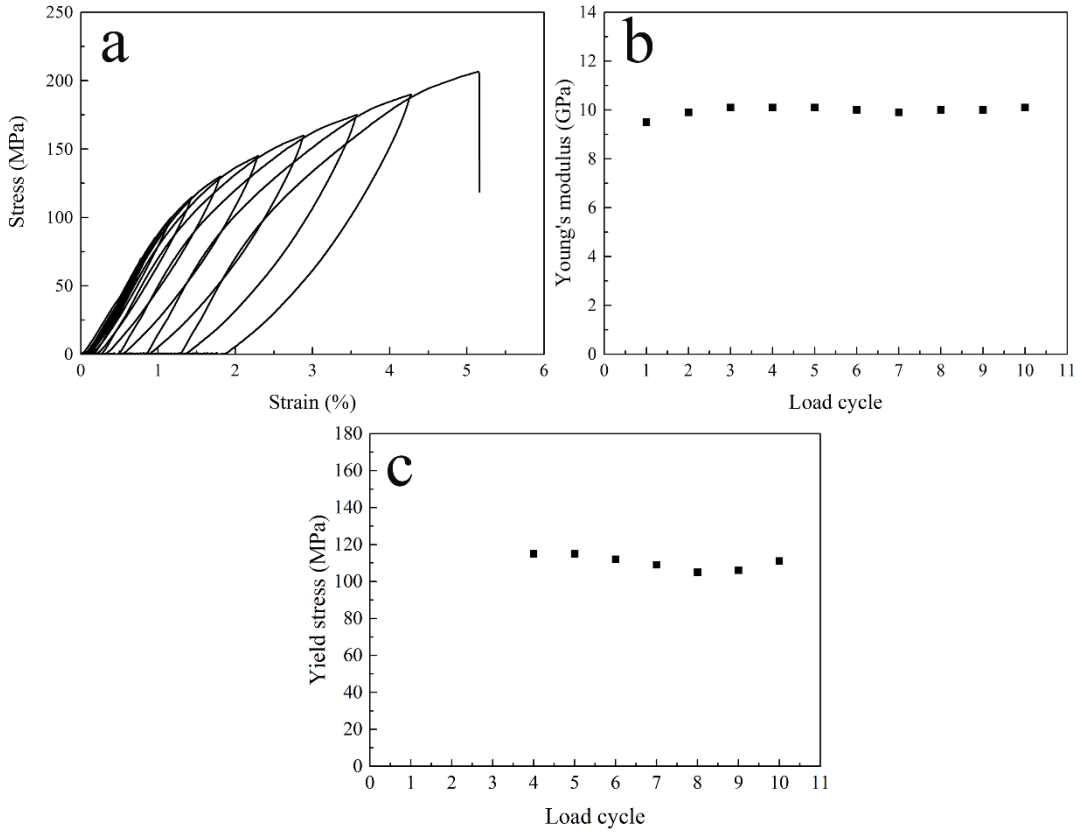

Figure 5.2 (a) Repeated loading-unloading testing curve, (b) Young's modulus at each loading cycle and (c) Yield stress at each loading cycle.

Raman spectroscopy was used to examine the micromechanics of cellulose nanopaper in both the elastic and inelastic region. Figure 5.3(a) shows the Raman spectra of cellulose nanopaper at different levels of strain where a peak initially at around 1095 cm^{-1}, which corresponds to the C-O and C-C stretching mode in the cellulose backbone, can be observed for an undeformed sample [156-158]. This peak shifts to lower wavenumbers

when the cellulose nanopaper is stretched. This shift can be ascribed to molecular straining of the cellulose molecules [159]. The shift of the Raman peak positions are plotted against applied stress and strain in Figure 5.3(b) and (c), respectively with the data fitted by linear functions with high correlation. This indicates that all cellulose molecules are effectively stressed proportional with the applied stress and/or strain. As the Raman band shift reflects the extent of molecular straining, the band shift rate (slope of Raman band shift against stress) will change if the contribution of the applied stress to the molecular deformation changes [160, 161]. Therefore, it can be concluded that no apparent change in molecular straining was detected by Raman spectroscopy. One can imagine that if the inelasticity is dominated by large scale inter-fibre slippage, the contribution of the applied stress to the molecular deformation will change. However, Raman spectra shows that such a change cannot be detected, meaning that inelasticity is not dominated by large scale inter-fibre slippage. Instead, the origin of inelasticity is likely to originate from a lower hierarchical level. It is worth noting that the Raman band shift here cannot be used to calculate the Young's modulus of cellulose nanopaper since the used Raman laser beam was not polarized. According to Tanpichai's et al. [57], a polarized laser beam is required to calculate the intrinsic Young's modulus since the Raman band shift rate changes with the angle between polarization direction of the beam and the strain direction. Therefore, the Raman band shift results can only be used for qualitative analysis.

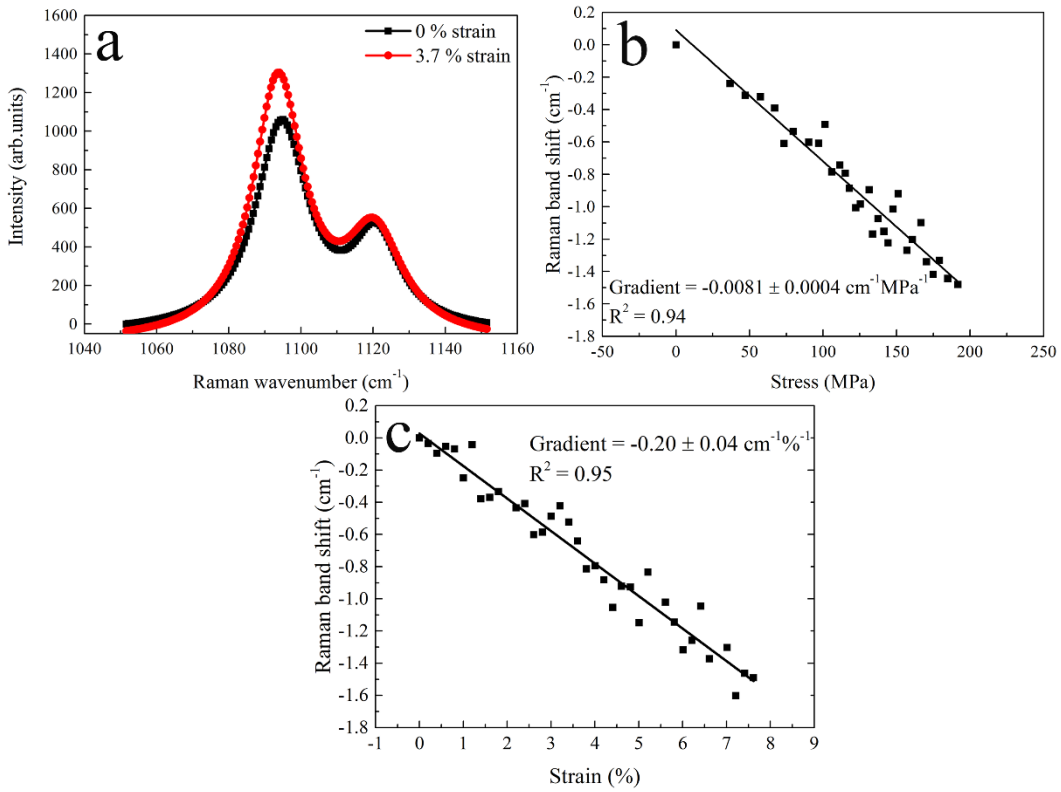

Figure 5.3 (a) Raman band shift with strain, (b) Stress dependent Raman band shifts for 1095 cm^{-1} peaks and (c) Strain dependent Raman band shifts for 1095 cm^{-1} peaks.

Figure 5.4 shows the X-ray diffraction pattern of cellulose. It can be seen that the diffraction peaks are located at 2θ angles of 15.1°, 16.4°, 22.4°, 34.4°, which are typical native cellulose peaks. The calculated crystallinity of the nanocellulose is 44.4 %, which means that cellulose is composed of approximate the same amount of crystalline and amorphous regions. Therefore, both the crystalline and amorphous phase need to be examined with respect to their contribution to the inelastic behaviour of cellulose nanopaper.

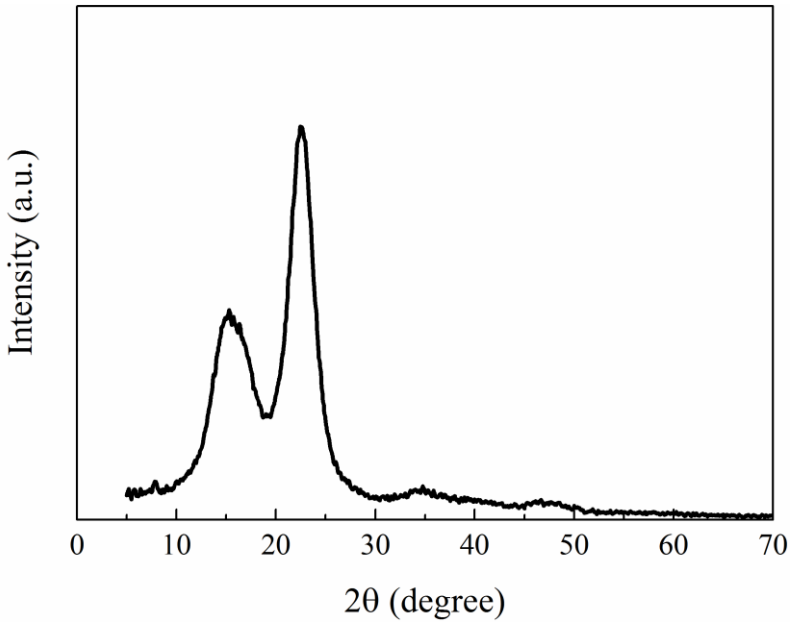

Figure 5.4 X-ray diffraction spectra of cellulose nanopaper.

The orientation of cellulose nanofibres and crystalline regions in nanofibres can be examined using 2D WAXD. The reorientation of nanofibres has been reported for samples that being drawn at wet state prior to drying [72]. These nanofibres could reorient because the hydrogen bonding was interfered by water molecules which also acted as plasticizer between nanofibres. Therefore, nanofibres were able to move and align themselves in the direction of the external force. Figure 5.5 shows the 2D WAXD data perpendicular to the nanopaper surface. Tests were conducted on nanopapers before and after straining to failure (relatively dry state). In-plane orientation of the nanocellulose in the paper is completely random before straining. Interestingly, this random orientation remained even when the sample was stretched into the inelastic region and up to ultimate failure. Crystalline regions in the cellulose nanofibres did not reorient along the straining direction, confirming the earlier hypothesis that cellulose nanofibres do not reorient in the inelastic region since the c-axis of cellulose crystals align with the nanofibres axis [56].

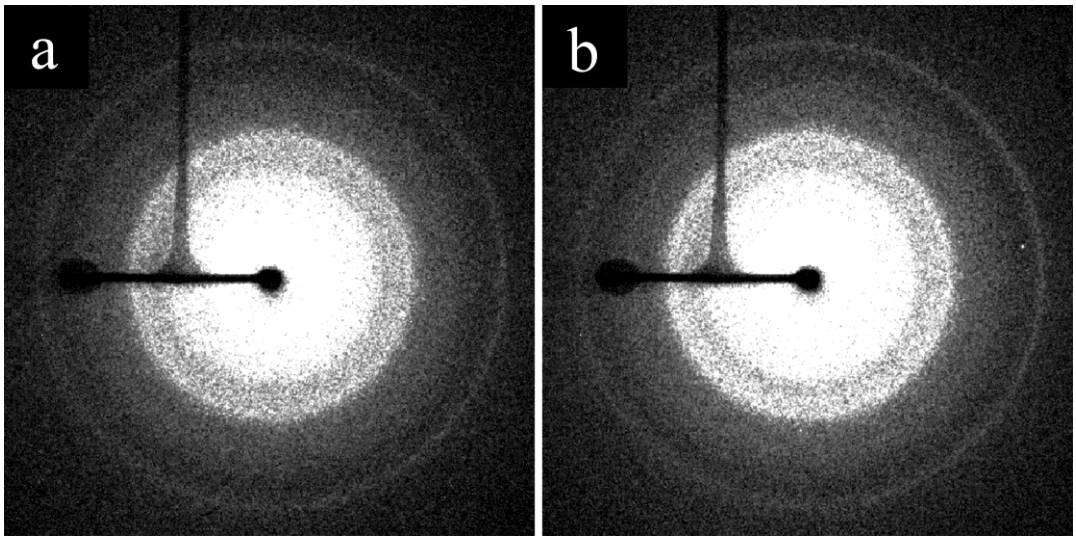

Figure 5.5 2D WAXD patterns with the X-ray beam perpendicular to the cellulose nanopaper surface: (a) before straining and (b) after ultimate failure.

From above observations, it can be hypothesized that inelasticity in cellulose nanopaper is not the result of reorientation of cellulose nanofibres or crystalline regions in cellulose nanofibres. Hence, it is of interest to examine more closely the contribution of the amorphous regions in cellulose nanofibres to the inelastic deformation behaviour. Figure 5.6 shows the images taken by POM with the nanopaper placed between crossed polarizers. Figure 5.6(a) and (b) show the optical images before straining, with the sample being positioned at the angles of 0° and 45° relative to the polarization axis. Images for both angles appear dark, indicating an isotropic structure of the cellulose nanopaper. Figure 5.6(c) and (d) show the optical images of samples after failure at angles of 0° and 45° with the polarization axis. The image at 0° is dark while the image at 45° appears bright. This indicates that this sample exhibits some anisotropy upon straining in the inelastic region. Furthermore, it can be deduced that this anisotropy originates from amorphous regions.

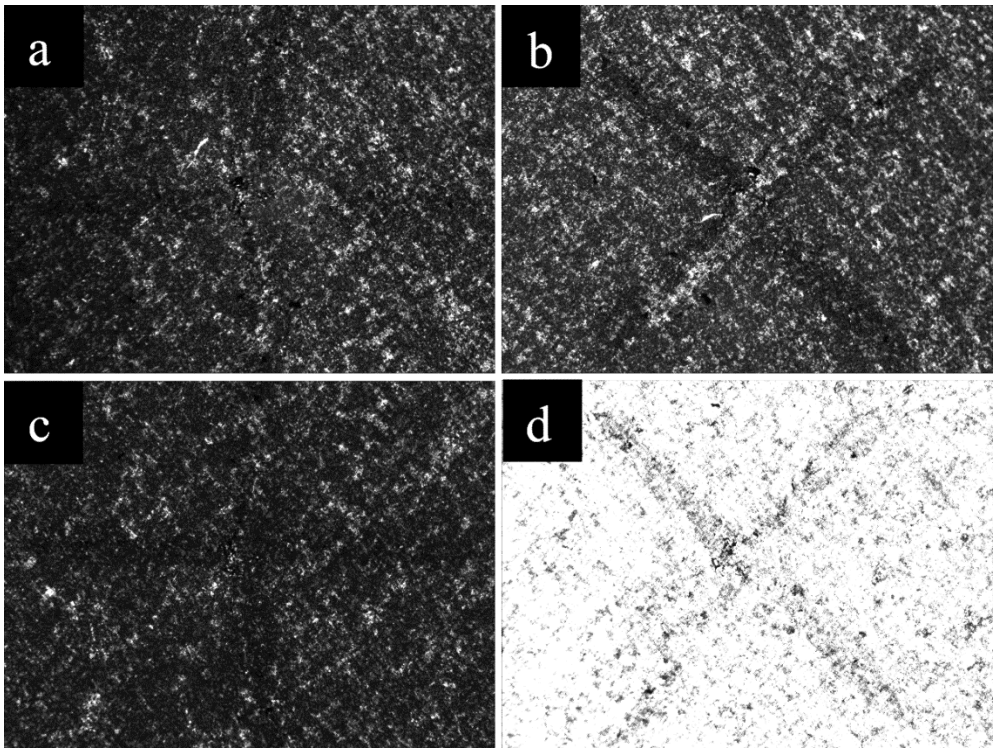

Figure 5.6 POM images of cellulose nanopaper (pre-conditioned at 23 °C and 50 % RH) at different angles between straining direction and polarization direction: (a) before straining, 0° angle, (b) before straining, 45° angle, (c) after ultimate failure, 0° angle and (d) after ultimate failure, 45° angle. The black cross is a marker to locate the imaging region before and after straining.

Yielding in polymers is often attributed to the changes of chain conformation in amorphous regions, which depends on the chain mobility. Yielding takes place when the molecular plastic strain rate resulting from chain mobility matches the applied strain rate. At high temperature, chain mobility increases so that molecular strain rate is easier to match the applied strain rate resulting in yielding at lower stress. Similarly, lower applied strain rates will result in a lower yield stress [162-166]. The relationship between yield stress and temperature and applied strain rate can be described by the Eyring equation [167].

$$\dot{\varepsilon} = \dot{\varepsilon}_0 \exp(-\frac{\Delta H}{RT}) \sinh\left(\frac{V\sigma_y}{RT}\right) \qquad \text{Equation 5.1}$$

where $\dot{\varepsilon}$ is the strain rate, σ_y is the yield stress, $\dot{\varepsilon}_0$ is the constant pre-exponential factor, ΔH is the activation energy, V is the activation volume, R is the gas constant and T is the absolute temperature. Equation 5.1 can be expressed as following:

$$\frac{\sigma_y}{T} = \frac{R}{V} \sinh^{-1}\left(\frac{\dot{\varepsilon}}{\dot{\varepsilon}_0} \exp\left(\frac{\Delta H}{RT}\right)\right) \qquad \text{Equation 5.2}$$

For large yield stress, Equation 5.2 can reduce to:

$$\frac{\sigma_y}{T} = \frac{R}{V} (\ln\left(\frac{2\dot{\varepsilon}}{\dot{\varepsilon}_0}\right) + \frac{\Delta H}{RT}) \qquad \text{Equation 5.3}$$

To achieve the temperature dependence of yield stress, specimens were pre-conditioned under i) a temperature of 23 °C and RH of 50 % and ii) a temperature of 50 °C and RH of 50 % respectively, prior to tensile testing. Figure 5.7 shows the strain rate and temperature dependence of the yield stress for cellulose nanopaper where temperature-normalized yield stress is plotted against logarithmic strain rate for samples pre-conditioned at different temperatures. Here the 0.2 % offset yield point is used since there is no maximum stress at yield in the stress-strain curve. It can be seen that the normalized yield stress increases with strain rate but decreases with temperature. This indicates that lower strain rates and higher temperatures facilitate the mobility of cellulose molecules. Equation 5.3 was used to fit the data of yield stress versus strain rate at different temperatures. It can be seen that yield stress increases linearly with the logarithm of strain

rate and the fitted lines at different temperatures are parallel, which indicates that one thermally activated process can be used to describe the yield behaviour under these conditions. The values of the activation parameters, ΔH and V, are shown in Figure 5.7. The activation volume is 0.8 nm^3, which is defined as the product of cross-sectional area of the moving unit and its moving distance [168]. The activation energy which is defined as the energy barrier for the molecular process [168] is 157 kJ/mol. This value is much higher than the dissociation energy of hydrogen bonds which ranges from 20 to 50 kJ/mol [169] but lower than the dissociation energy of C-C and C-O covalent bonds ranging from 300 to 500 kJ/mol [167, 170], suggesting that hydrogen bonds were broken when cellulose nanopaper was loaded in the inelastic region. Therefore, this data suggests that the inelastic behaviour of cellulose nanopaper originates from molecular mobility facilitated by breakage of hydrogen bonds.

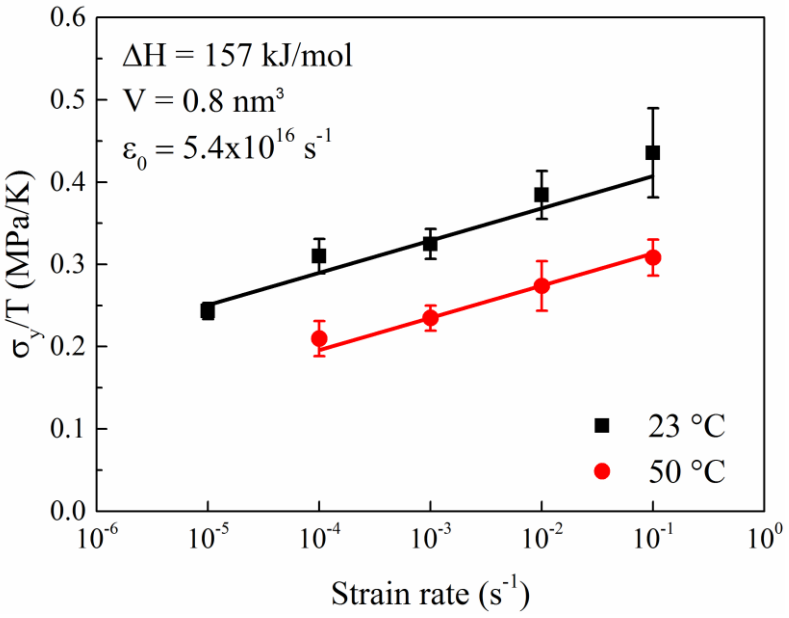

Figure 5.7 Strain rate and temperature dependence of the normalized yield stress of cellulose nanopaper.

Figure 5.7 demonstrates that under normal tensile test conditions (23 °C and 50 % RH), the inelastic behaviour of cellulose nanopaper is dominated by a single molecular process originating from the amorphous phase. In order to study these molecular processes in more detail, possible relaxation processes in nanocellulose were examined using dielectric spectroscopy. Figure 5.8 shows the temperature dependence of the dielectric loss at different frequencies. Two dielectric loss peaks can be identified at a frequency of 100 Hz. Dielectric properties of cellulose have been investigated previously [171-173]. The peak of the dielectric loss at low temperatures is usually assigned to secondary relaxation while the one at higher temperatures is attributed to primary relaxation and has been proposed as the dielectric manifestation of the glass transition [173]. It is worth noting that dielectric loss peaks move to higher temperature for higher frequencies of applied electric field. This behaviour is consistent with the strain rate and temperature dependence of the yield stress. Since the strain rate and temperature dependence of the yield stress is associated with a single molecular process, one may assume that the inelastic behaviour of cellulose nanopaper is dominated by segmental motion of the cellulose main chain.

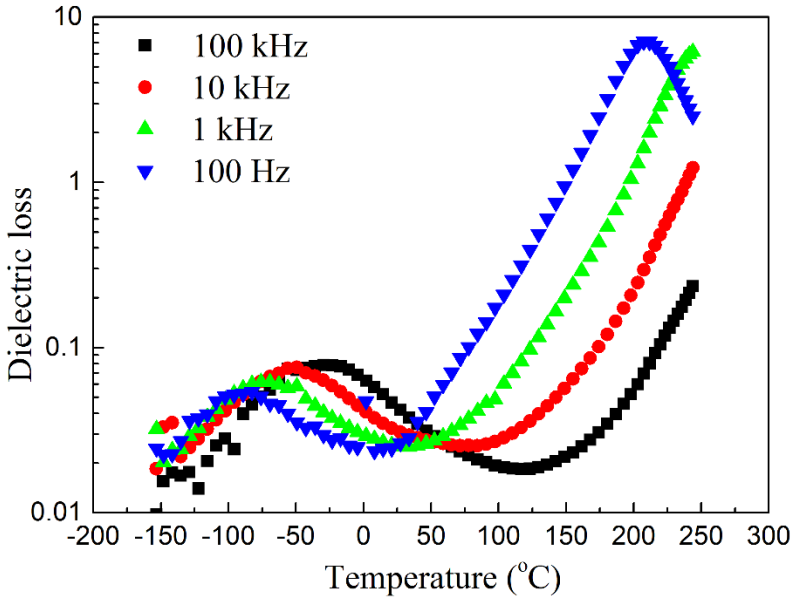

Figure 5.8 Dielectric loss versus temperature at different frequencies for cellulose nanopaper.

5.3 Conclusions

Cellulose nanopaper is composed of hydrogen bonded cellulose nanofibres. Upon loading, it shows significant inelastic behaviour which results in its high toughness. Previous research suggested that the inelasticity originated from the inter-fibre slippage while the current work hints the segment motion of cellulose molecules as the prime cause for the inelastic behaviour of cellulose nanopaper. To be specific, strain mapping revealed that inelasticity occured all over the sample. Mechanical testing and Raman spectroscopy indicated that inelasticity is not the result of large scale reorientation of cellulose nanofibres. 2D WAXD patterns suggested that also molecular reorientation in crystalline regions is not responsible for the inelastic behaviour. On the other hand, POM images revealed a transition from an isotropic amorphous structure to an anisotropic structure after straining. Finally, the inelastic behaviour of cellulose nanopaper was proven to be dominated by a single molecular process during which the activation energy is sufficient

to break hydrogen bonds but not enough to break covalent bond. The temperature dependence of the dielectric loss showed that inelasticity occurred in a temperature range where primary relaxation dominates.

Chapter 6

Mechanical properties of cellulose nanopapers prepared using different methods

6.1 Introduction

The mechanical properties of cellulose nanopaper can be tailored through different preparation methods. In this chapter, different methods were used to tailor the microstructure of cellulose nanopaper and their effect on the mechanical properties of cellulose nanopapers were studied. First, cellulose nanopapers are prepared by a hot pressing method varying pressure and temperature as described in Chapter 3. In addition the mechanical properties of cellulose nanopaper prepared by a suspension casting method are evaluated and compared. In this chapter, BC nanopaper is not used as this chapter focusses on the effect of processing conditions of NFC based nanopaper and its effect on mechanical properties.

6.2 Results and discussion

6.2.1 Orientation of nanofibres in cellulose nanopaper

The 2D WAXD measurements were carried out perpendicular and parallel to the surface of nanopaper in order to investigate the degree of orientation of the nanofibres in the directions parallel to the nanopaper surface plane and to the cross sectional plane, respectively. Because the c-axis of cellulose (200) crystalline plane align with the nanofibres axis, the orientation of the nanofibres can be represented by the orientation of cellulose crystallites [174]. Figure 6.1(A)-(D) exhibits the ring patterns when the beam is perpendicular to the nanopaper surface (referred to as IP), showing that nanofibres are randomly oriented in the direction parallel to the surface plane of the nanopaper. On the contrary, the ring patterns obtained when the beam is parallel to the nanopaper surface (referred to as CS) show the preferential orientation of the nanofibres in the direction parallel to the cross sectional plane (Figure 6.1(a)-(d)). Herman's orientation factors are provided in those figures. It can be found that the degrees of orientation in the direction parallel to the cross sectional plane are similar for all preparation methods indicating limited influence of preparation routes on orientation of nanofibres.

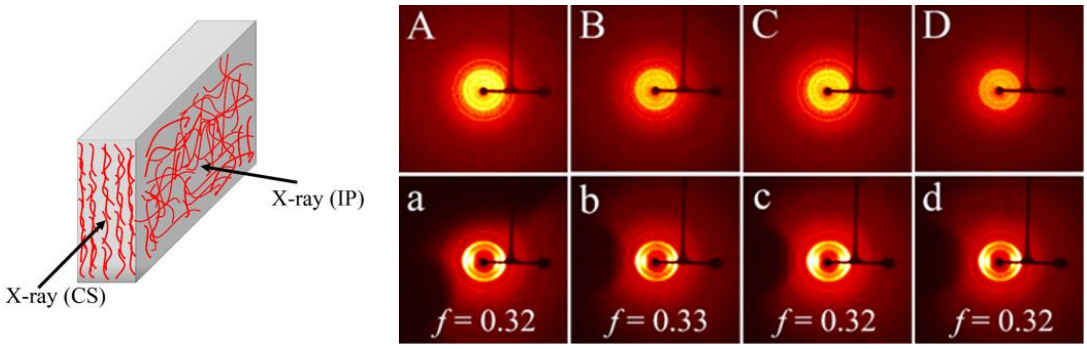

Figure 6.1 2D WAXD patterns representing in-plane direction (IP) and cross sectional (CS) orientation of cellulose nanofibres: (A) P05T93, IP, (B) P10T93, IP, (C) P10T37, IP, (D) SC, IP, (a) P05T93, CS, (b) P10T93, CS, (c) P10T37, CS and (d) SC, CS. The Herman's orientation factors in CS direction factor are shown at the bottom of the figures.

6.2.2 Mechanical properties

The apparent mechanical properties of cellulose nanopaper prepared at different hot compaction pressures are shown in Figure 6.2 and listed in Table 6.1. It can be seen that Young's modulus, strength and yield stress increase from 3.5 GPa, 95 MPa and 47 MPa for P05T93 sample to 5.0 GPa, 110 MPa and 67 MPa for P10T93 sample, respectively. The increase in Young's modulus and yield stress at higher compaction pressures is speculated to be associated with a denser structure and the formation of more hydrogen bonds. Such a denser network structure at higher compaction pressures is confirmed from porosity data which decreases from 46 % to 36 % when pressure increases from 0.5 MPa to 10 MPa (Table 6.1). Therefore, it seems plausible that mechanical properties increase significantly with hot compaction pressure. However, cellulose nanopaper has a layered structure in cross-section direction (Figure 6.3). The distances between these layers are clearly different for samples prepared at different pressures. As a result, the measured stress would be lower than the actual stress sustained by the layers in the nanopaper since

the inter-layers do not fully bear the load. Therefore, in order to investigate the intrinsic load carrying capability of the layers, the distance between layers needs to be minimized.

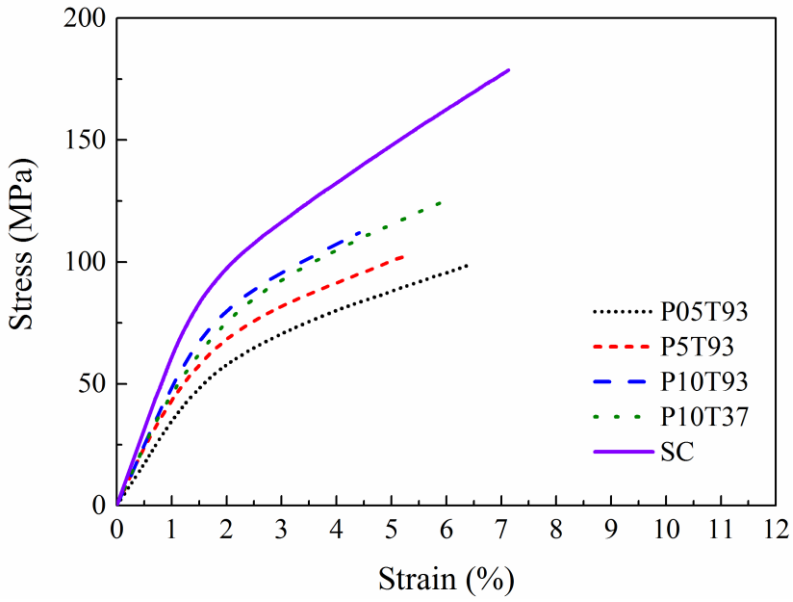

Figure 6.2 Stress-strain curves of cellulose nanopapers prepared from different methods.

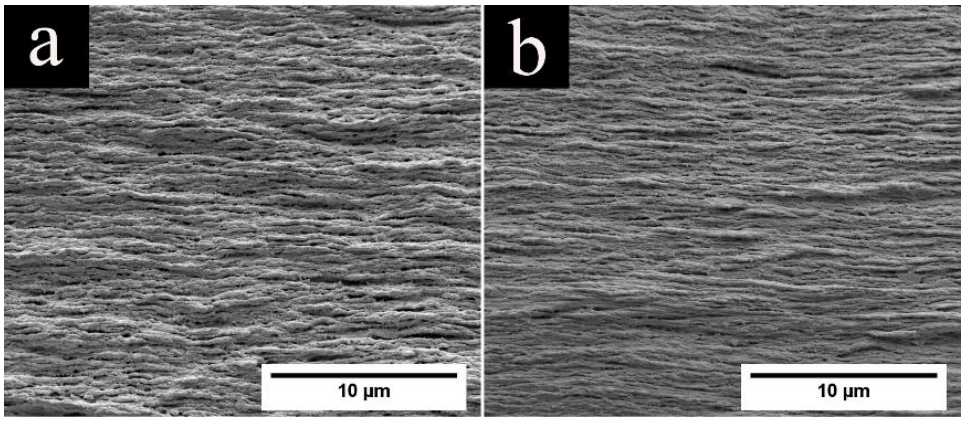

Figure 6.3 Cryogenic fracture surface of (a) P05T93 and (b) P10T93 samples.

To exclude the effect of inter-layers, the specific mechanical properties were considered where thickness was replaced by values of weight per unit surface area for the calculation of the cross-sectional area. The values of specific Young's modulus, strength and yield stress are shown in Figure 6.4 and listed in Table 6.1, showing that the specific Young's

modulus and specific yield stress increase with compaction pressure, while the specific tensile strength is independent of pressure. Henriksson et al. proposed that the failure of nanopaper is associated with fracturing of nanofibres [4]. This implies that the specific strength of nanopaper is primarily controlled by fibre properties which are not affected by hot compaction pressure.

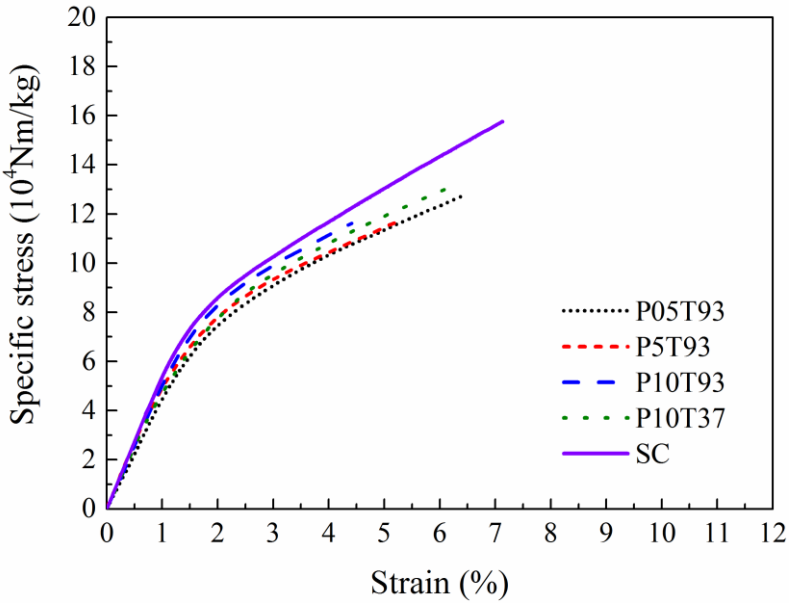

Figure 6.4 Specific stress-strain curves of cellulose nanopapers prepared by different conditions and methods.

The effect of hot pressing temperature on apparent mechanical properties of cellulose nanopaper was also studied. Table 6.1 displays that the Young's modulus and yield stress of P10T37 samples are similar to P10T93. In addition, the strength and strain-at-break of P10T37 are slightly higher than those of P10T93. The specific mechanical properties show the same trend as their counterparts. Therefore, temperature is considered not to significantly affect mechanical properties.

Table 6.1 Young's moduli, yield stress, ultimate tensile strength and their specific counterparts as well as strain-at-break and porosity of samples prepared from different methods

	P05T93	P5T93	P10T93	P10T37	SC
Porosity (%)	46 (6)	38 (4)	36 (2)	32 (7)	22 (3)
Young's modulus (GPa)	3.5 (0.1)	4.2 (0.5)	5.0 (0.3)	5.1 (0.6)	7.3 (0.9)
Yield stress (MPa)	47.1 (3.7)	59.9 (5.3)	66.8 (2.9)	66.4 (9.1)	83.4 (4.3)
Ultimate tensile strength (MPa)	95.4 (9.6)	106.4 (6.2)	110.4 (8.2)	129.8 (9.0)	177.1 (10.5)
Specific Young's modulus (10^6Nm/kg)	4.5 (0.4)	4.7 (0.4)	5.3 (0.2)	5.2 (0.6)	6.4 (0.8)
Specific yield stress (10^4Nm/kg)	6.1 (0.8)	6.7 (0.7)	7.3 (0.3)	7.1 (0.6)	7.3 (0.3)
Specific strength (10^4Nm/kg)	12.8 (1.8)	12.1 (0.8)	11.9 (0.7)	13.0 (1.4)	15.6 (1.3)
Strain-at-break (%)	7.0 (0.9)	5.9 (0.9)	4.7 (0.5)	5.7 (0.8)	6.7 (1.5)

The apparent mechanical properties of cellulose nanopapers prepared by hot pressing and suspension casting methods are compared. From Table 6.1, it can be seen that the Young's modulus, yield stress and ultimate tensile strength of SC sample are higher than all the hot pressed samples. The specific mechanical properties of SC samples also show the same trend except the specific yield stress which is similar to the highest value for the hot pressed samples. The superior Young's modulus and strength values of SC sample is associated with its low porosity (22 %) where a denser microstructure with a higher fibre

content and increased number of hydrogen bonds can be formed. The dense structure in SC sample is speculated to be related to the slow evaporation of cellulose suspension during which strong capillary forces dragged cellulose nanofibres together and resulted in a dense structure. During hot pressing, the wet cake made of cellulose nanofibres and water was stacked between filter papers and the water in the wet cake was quickly absorbed by the filter papers, leaving behind cellulose nanofibres that were not all that closely assembled. Hence, a looser structure with fewer hydrogen bonds than the SC sample was obtained after the wet cake was completely dried to a nanopaper.

The values of Young's modulus and their specific counterparts are plotted against porosity (Figure 6.5). Both Young's modulus and its specific modulus value decrease with increasing porosity. Indeed, lower porosity indicates a denser fibrous network which results in the formation of more connections between nanofibres and better inter-fibre stress transfer, leading to higher values of Young's modulus. The data of Young's modulus can be fitted using the linear function shown in Figure 6.5 indicating that Young's modulus decreases linearly with increasing porosity in the range from 22 % to 46 %.

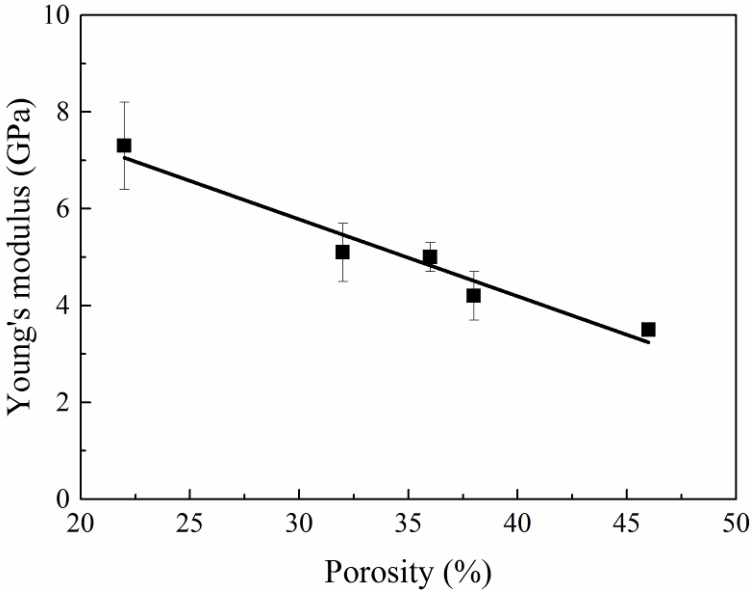

Figure 6.5 Relationship between porosity and Young's modulus.

To summarize, the apparent mechanical properties of cellulose nanopaper can be tailored to a great extent using different preparation methods. However, the differences in specific mechanical properties are much smaller than the differences in apparent mechanical properties since specific values reflect more the intrinsic load bearing properties that less affected by preparation method. Higher porosity is detrimental to the mechanical properties of nanopaper due to the formation of more voids which act as defects. This trend is consistent with the results from Arévalo and Peijs where the flexural strength and modulus were inverse to porosity [175].

6.2.3 Reorientation in cellulose nanopaper after straining

The changes in microstructure in cellulose nanopaper during deformation can be characterized by POM. In the case of P05T93, POM results (Figure 6.6) show an initial isotropic structure after preparation while some preferential orientation was observed after the deformation up to failure. On the contrary, P10T93 shows an isotropic structure both before and after deformation (Figure 6.7). The different results of POM can be

explained in combination with their mechanical behaviour where the P05T93 sample shows a lower yield stress as well as a higher value of strain-at-break than the P10T93 sample. It can be deduced that the reorientation of cellulose chain segments in amorphous regions in individual nanofibres takes place after yielding according to the mechanism described in Chapter 5 and becomes noticeable in POM measurement when strain at least exceeds the strain-at-break of P10T93.

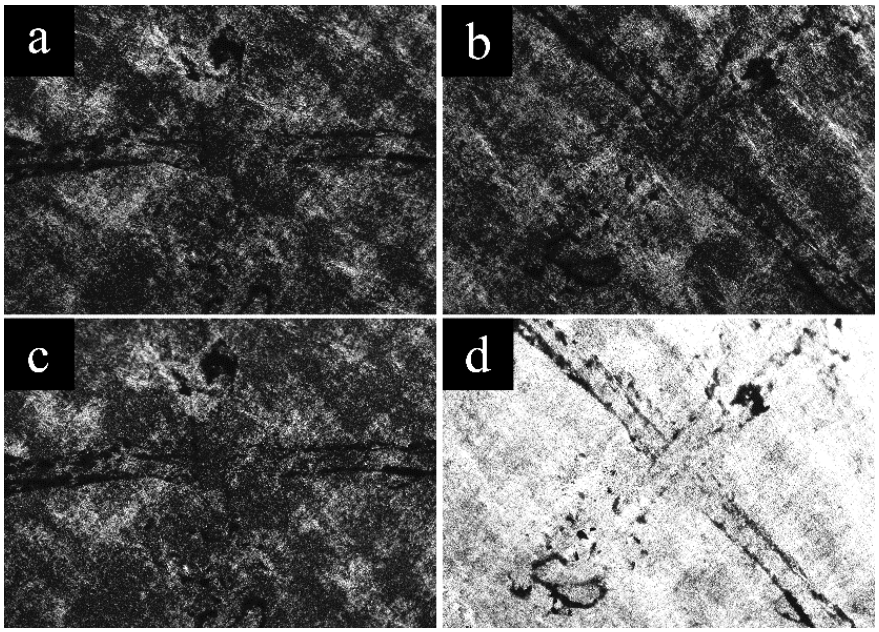

Figure 6.6 POM images of P05T93: (a) 0°, before deformation, (b) 45°, before deformation, (c) 0°, after deformation and (d) 45°, after deformation.

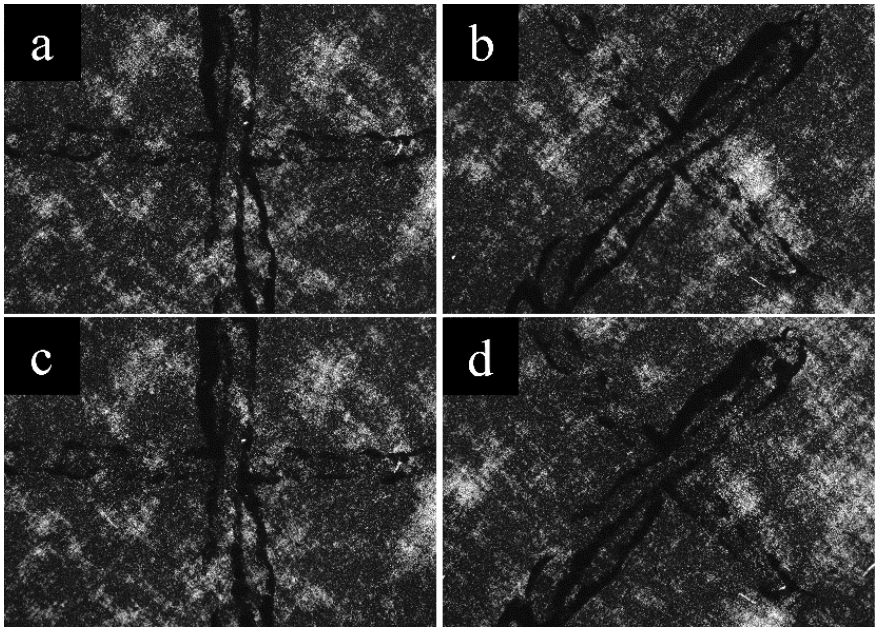

Figure 6.7 POM images of for P10: (a) 0°, before deformation, (b) 45°, before deformation, (c) 0°, after deformation and (d) 45°, after deformation.

6.3 Conclusions

Cellulose nanopapers were prepared using different methods. Cellulose nanopaper prepared by a suspension casting method showed superior mechanical properties compared with all the hot pressed samples due to its lower porosity and denser structure, which resulted in fewer defects and more fibre-fibre connections. The dense structure of SC sample is speculated to be related to the slow evaporation process during which the capillary force dragged cellulose nanofibres together. For hot pressing samples, the water in the wet cake was quickly absorbed by the filter papers, leaving behind cellulose nanofibres that were less closely assembled. Hence, a looser structure with fewer hydrogen bonds than the SC sample was obtained after the wet cake was hot pressed to a nanopaper. High hot compaction pressure leads to enhanced Young's modulus, yield stress and a reduction of strain-at-break due to the formation of denser and more compact microstructure. The specific mechanical properties as calculated from load over the

production of weight per unit area and width of the specimen reflect better the intrinsic loading carrying properties since the effect of the inter-layer space between the nanocellulose layers is excluded. The specific strength is independent of the compaction pressures since the mechanical properties of nanofibres are independent of pressure. The compaction temperature showed no significant influence on mechanical properties. For all the samples, porosity showed an adverse effect on Young's modulus. POM results showed that reorientation of cellulose chain segments in amorphous regions in individual nanofibres for nanopapers compacted at low pressures took place after yielding and became noticeable when inelastic deformation was significant.

Chapter 7

Modelling the elastic properties of cellulose nanopapers

7.1 Introduction

Materials based on cellulose have great potential to be used as sustainable engineering materials [3, 175]. In most cases, engineering materials are designed to be served within their elastic limit. Therefore, elastic properties such as the Young's modulus of a material are important design parameters. Conceptually, the elastic modulus of cellulose nanopaper could depend on a number of factors such as intrinsic fibre properties, inter-fibre connectivity, fibre orientation and density of the nanopaper. In this chapter, 2D fibrous network models were developed to simulate the elastic modulus of cellulose nanopaper. The dependence of the elastic modulus on fibre dimensions, fibre elastic modulus, fibre waviness, bond density as well as density of the nanopaper was investigated.

7.2 Fibrous network models

7.2.1 Generation of 2D fibrous network

First, the centre points of the fibres were uniformly distributed in a 2D box. Then, fibres grew from those centres generally along either the x- or y-axis (growing axis). As fibres grew, new fibre nodes were added one by one in both positive and negative direction of the growing axis. The added new nodes were not placed exactly along the growing axis but slightly shifted from this axis in order to generate bend fibres [176]. The amount of shift can be represented by a parameter called waviness. Afterwards, the fibres were rotated at random angles to achieve a randomly distributed network. Finally, the segments of fibres that extended outside the box boundary were cut off. The size of the network was limited to 10 x 8 μm according to limitations in computer power. Fibres in the middle of the network (area of 8 x 8 μm) could move freely while movement of the remaining fibres followed the boundary conditions described in Section 7.2.3.

7.2.2 Fibre properties and their bonding

The fibres were discretized with elastic Timoshenko beam elements. Bonds between fibres were found at their intersections and one node was placed on each fibre as bonding site. The bonding sites were point-wise connected in both translational and rotational degrees of freedom so that the bonds could not slide or separate under straining. It is worth noting that short elements could be generated due to the nodes at bonding sites, which would cause errors in the models due to excessive distortion of elements and high element deformation speed. In this models, those nodes were not generated at bonding sites.

7.2.3 Boundary conditions

The boundary conditions of the 2D fibrous networks are shown in Figure 7.1. The fibres at the bottom of the 2D fibrous network were fixed while the fibres at the top were stretched along the y-axis under displacement control. Periodic boundary conditions were applied so that the left and right edges of the network moved synchronously. The calculations were carried out using the finite element program (Abaqus, version 6.11) [152].

7.2.4 Parametric study

In this study, parameters were varied to investigate their effect on the elastic modulus of cellulose nanopaper. Here, the effect of individual fibre properties such as length, diameter, waviness and elastic modulus were investigated. The inter-fibre bond density and density of the cellulose nanopaper were also varied to investigate their effect on the elastic modulus.

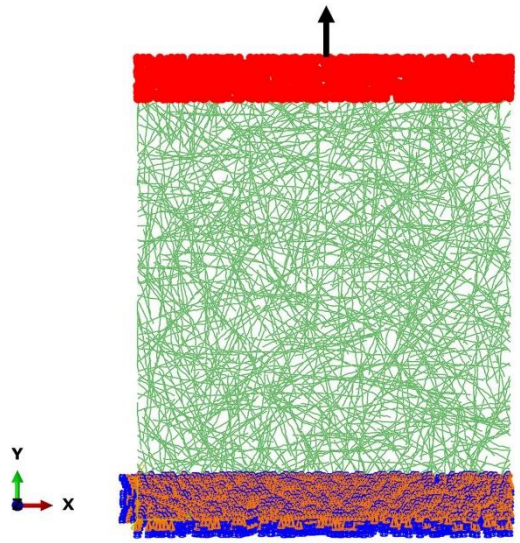

Figure 7.1 Illustration of a fibrous network model.

7.3 Results and discussion

7.3.1 Modelling of the cellulose nanopaper

The elastic modulus of cellulose nanopaper can be predicted using 2D fibrous network models. The length and diameter of cellulose nanofibres were assumed to be 2 μm and 40 nm, respectively, according to the model size which is limited by computational power. The modulus of the nanofibres was set at 100 GPa which is slightly below the theoretical modulus of cellulose crystals [18]. The relative density of the model was set at 0.9, which indicated a dense nanopaper. The resulting model showed that the average density of the nanofibres (number of nanofibres per unit area) was 15.2 μm^{-2} while the bond density (number of bonds per unit area) was 78 μm^{-2}. The calculated elastic modulus of the model of cellulose nanopaper was 12 GPa which is within the range of the experimental results for these type of materials [4]. The deformed shape of the model at a strain of 1 % is shown in Figure 7.2 where only part of the nanofibres were loaded since only extended fibre segments can transfer the load.

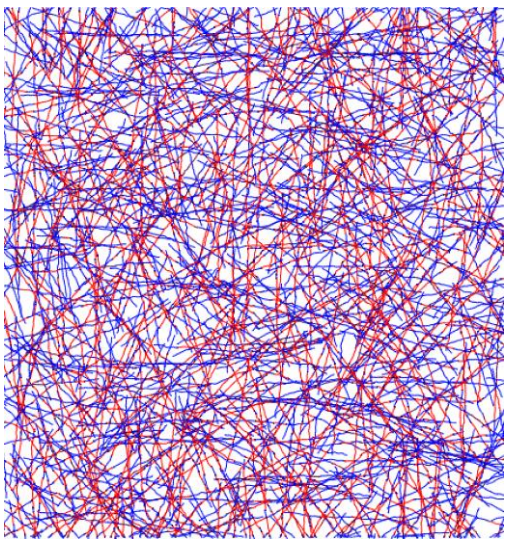

Figure 7.2 The deformed shape of the model at a strain of 1 %. Blue colour means low stress while other colours represent fibre areas that carry load.

7.3.2 Parametric study

The elastic properties of cellulose nanopaper are affected by factors that can be divided into intrinsic fibre properties, inter-fibre bonding as well as the density of the cellulose nanopaper. All these factors were implemented in this model in order to have a better understanding of structure-property relationships of cellulose nanopaper.

Figure 7.3 shows that the elastic modulus of the model increases with increasing fibre length from 1 to 3 μm. The elastic modulus strongly depends on the load transfer ability. Long fibres facilitate the formation of more inter-fibre bonds on each fibre so that the load transfer capability is enhanced. This can be demonstrated by the values of average number of bonds per fibre (ANBF) as also shown in Figure 7.3. This value increases with increasing fibre length, indicating that more fibre segments can transfer the load, resulting in a higher elastic modulus of the cellulose nanopaper. Figure 7.4 exhibits the stress state in models based on fibres of different lengths. It can be seen that only part of the fibres can transfer the load. The model made of longer fibres can transfer the load more efficiently leading to an increase in elastic modulus.

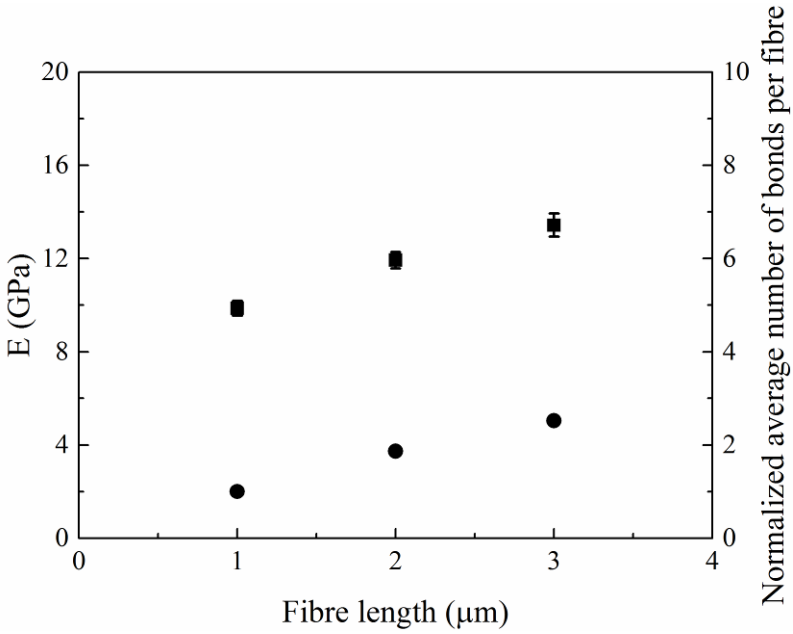

Figure 7.3 The elastic modulus of the model (square) and the normalized number of bonds per fibre (circle) increases with increasing fibre length.

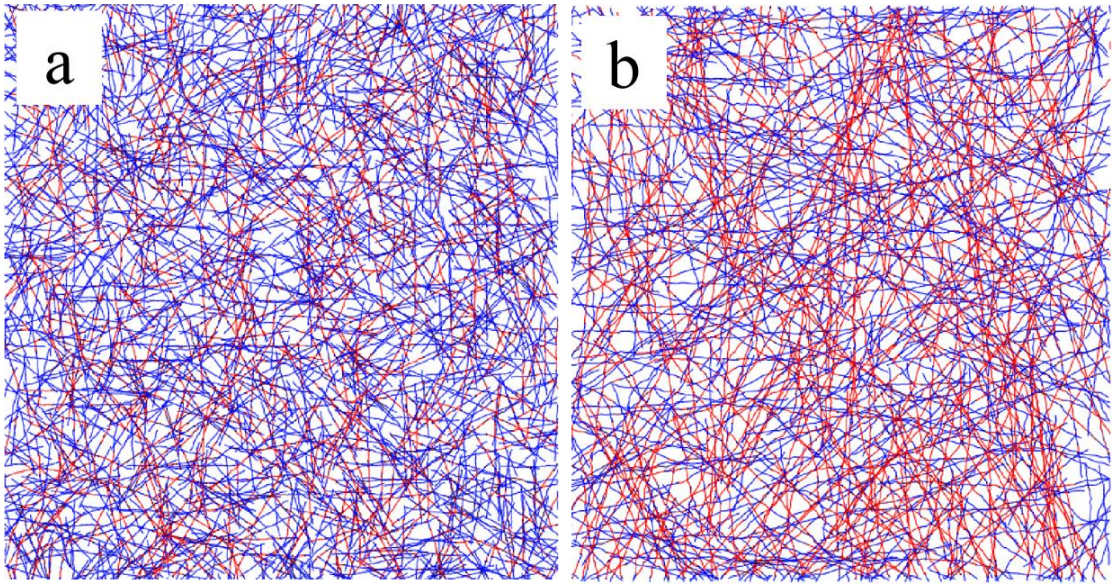

Figure 7.4 The stress state in the models at a strain of 1 % for different fibre lengths: (a) 1 μm and (b) 3 μm. Blue colour indicates low stress while other colours represent fibre areas that carry load.

Figure 7.5 shows that the elastic modulus of the model decreases with the increasing of fibre diameter. It is worth noting that changing the fibre diameters will alter the number of fibres since the volume of fibres in the model remains the same. Therefore, the model made of thicker fibres contain fewer fibres and hence also fewer inter-fibre bonds, which result in a significant decrease in the elastic modulus (Figure 7.5). The elastic modulus of the model is linearly proportional with the number of inter-fibre bonds (Figure 7.6), highlighting the significance of the number of bonds. From Figure 7.6, it can be deduced that the value of elastic modulus approaches zero when the number of bonds is below 1400. This means that below this value the bond density is too low to transfer the load.

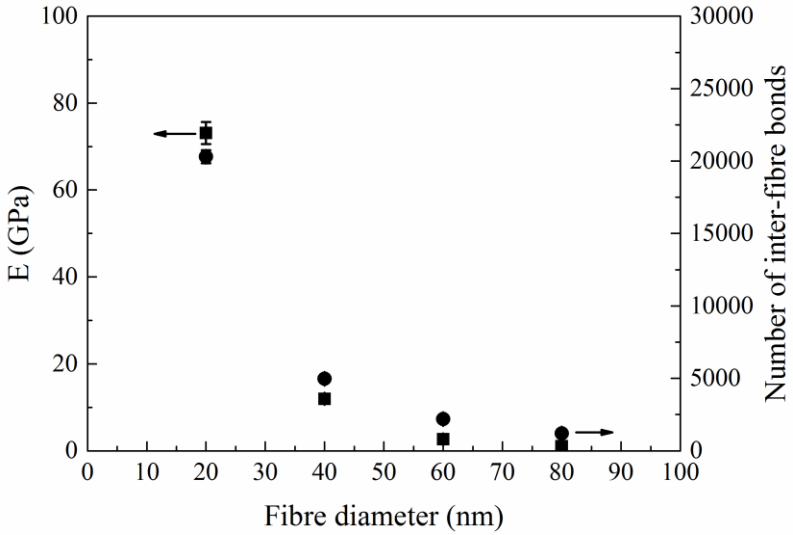

Figure 7.5 The elastic modulus of the model (square) and the number of inter-fibre bonds (circle) decrease with increasing fibre diameter.

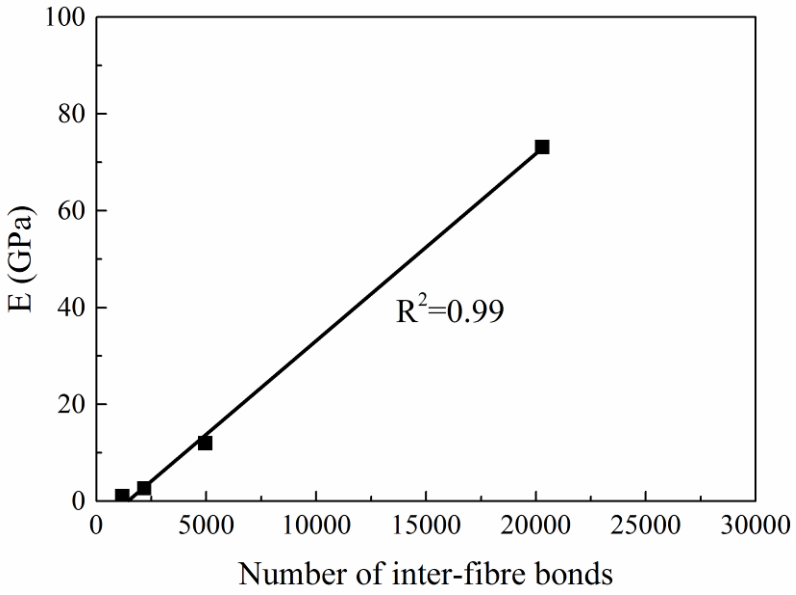

Figure 7.6 The elastic modulus of the model increases with the increasing number of inter-fibre bonds.

In this model, the extent of a fibre to deviate from straight to bend or curved prior to deformation is defined by a waviness factor. Figure 7.7 illustrates the effect of fibre waviness on elastic modulus. Fibres are straight when the waviness parameter equals zero. Those straight fibres impart a higher elastic modulus in the model than bend or curved ones because fibres can only bear load when fibre segments between neighbouring inter-fibre bonds are straight. Therefore, more fibre segments can bear the load at the early stage of loading when fibres are initially straight, which results in an increased elastic modulus. Indeed, it was reported that the elastic modulus of nanopapers dried while being constrained exhibited a 12 % higher modulus than those that were freely dried [126]. In this study it was suggested that fibres exhibited a more extended shape when dried while constrained, hence leading to a higher elastic modulus.

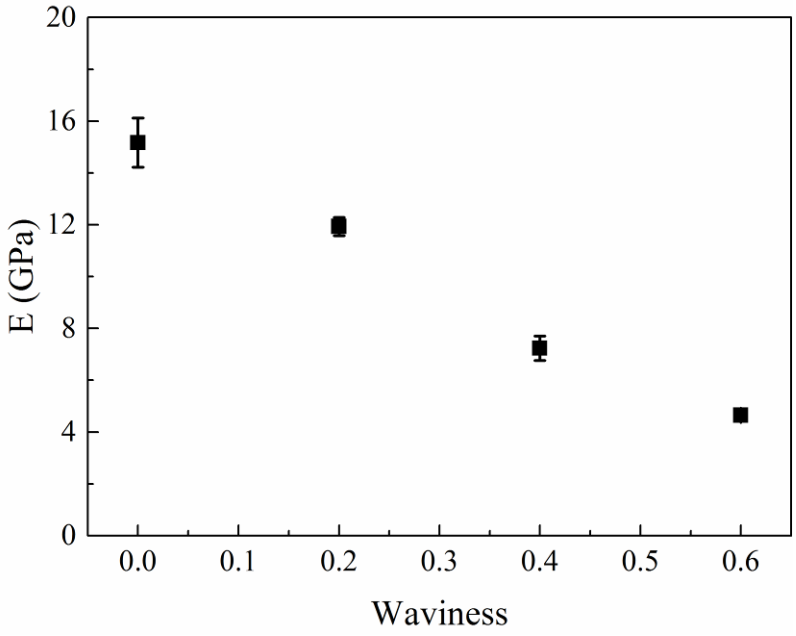

Figure 7.7 The elastic modulus of the model as a function of fibre waviness.

Figure 7.8 shows the effect of elastic modulus of fibres on the elastic modulus of the model. The elastic modulus of the model increases linearly with the elastic modulus of the fibres. This trend is consistent with Cox's model [177] but the values of elastic moduli in the fibrous network models are lower. Cox's model assumes straight, continuous fibres which can bear the load most efficiently in the fibrous network. The bend and shorter fibres in the current model results in fewer load bearing segments and elastic moduli below those predicted by the Cox model. The Krenchel's efficiency factor has been used to relate the effective modulus of single fibres to the elastic modulus of a well compacted two-dimensional (2D) random cellulose nanopaper [57, 178] where the value of the elastic modulus of the nanopaper was 3/8 of the modulus of a single fibre. Figure 7.8 shows that the Krenchel's model still overestimates the elastic modulus, probably giving an upper bound value as this estimation does not consider the effect of fibre length and volume fraction of fibres. The cellulose nanopaper can be considered as 2D in-plane

randomly distributed fibre reinforced composites. The generalized form of the rule-of-mixture (ROM) for fibre reinforced composites is given by [174, 179]:

$$E_c = \eta_l \eta_o E_f V_f + E_m V_m \qquad \text{Equation 7.1}$$

where E_c is the elastic modulus of the composite, η_l is the fibre length distribution factor which ranges from 0 to 1, η_o is the Krenchel's efficiency factor, E_f and E_m are the elastic moduli of fibres and matrix, respectively, V_f and V_m are volume fraction of fibres and matrix, respectively. In this model, the second term in Equation 7.1 can be neglected since cellulose nanopaper is made of nanofibres and E_m can be neglected. The relation between elastic modulus of the cellulose nanopaper and elastic modulus of the fibres is also plotted in Figure 7.8 where η_l is assumed to be 1 meaning continuous fibres. The predicted elastic modulus still overestimates experimental data since the fibres in the nanopaper are short and curved. Hence, not all the fibres can transfer the load under deformation.

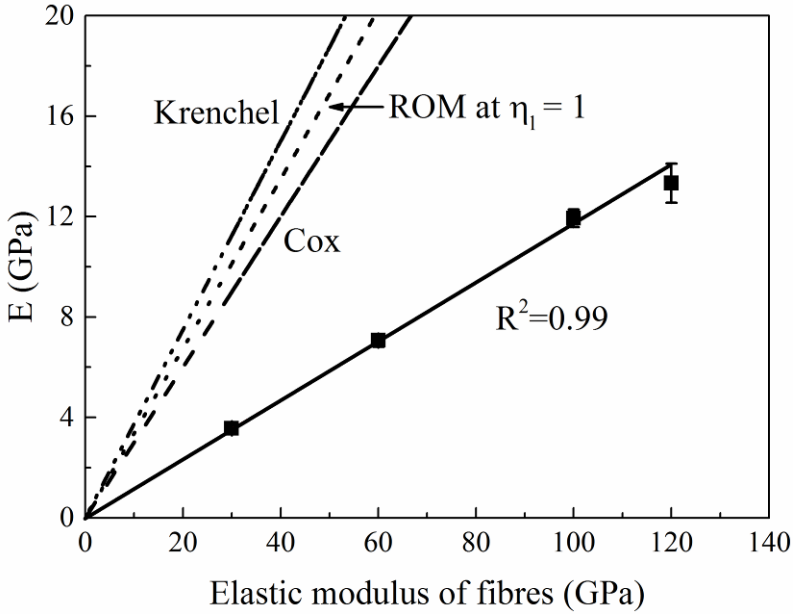

Figure 7.8 The elastic modulus of the model as a function of fibre modulus and the evaluation of the elastic modulus using Cox's, ROM and Krenchel's theories, respectively.

Figure 7.9 shows the effect of relative density of the model on its elastic modulus. It can be seen that the elastic modulus increases linearly with the relative density. The low relative density results in weak connectivity between fibres such that load transfer is worse. Figure 7.10 shows the stress state at a macroscopic strain of 1 % in the models with different relative densities. It can be seen that few sites on the fibres can transfer load in the model of low density. On the contrary, much more fibres transfer the load in the dense model, indicating better stress transfer and higher elastic modulus.

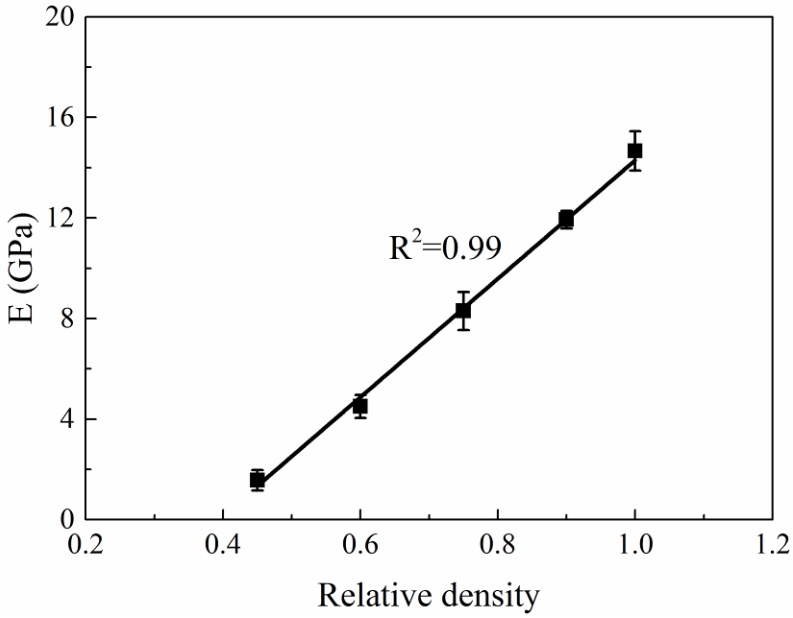

Figure 7.9 The elastic modulus of the model increases with increasing relative density.

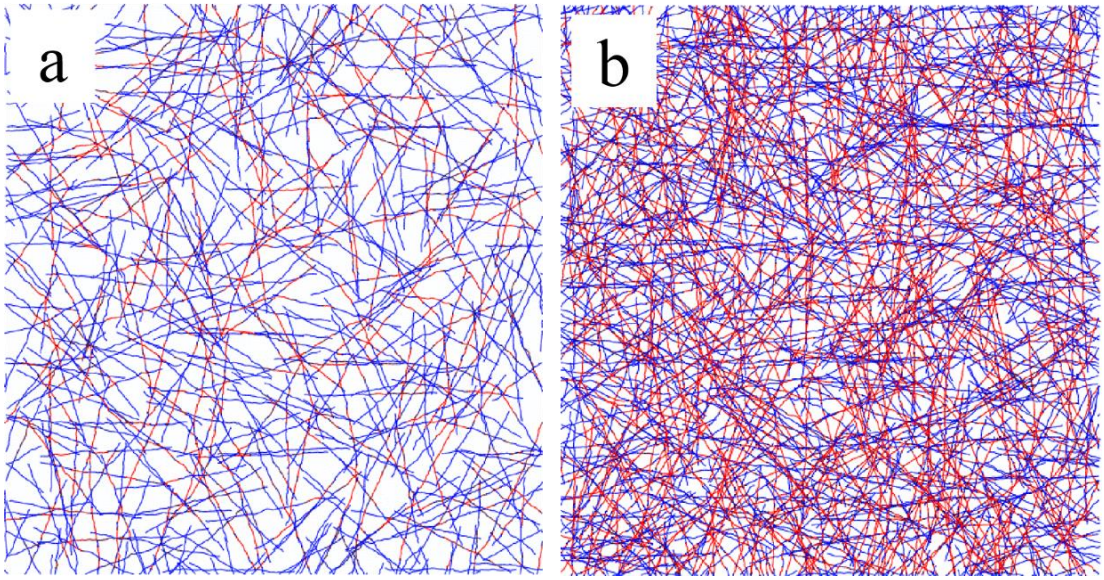

Figure 7.10 The stress state in the models at a global strain of 1 % with different relative densities of: (a) 0.45 and (b) 1.0. Blue colour indicates low stress while other colours indicate fibre regions that carry load.

The bonds between fibres play a significant part in the elastic modulus. In the model, these bonds were assigned at the intersection sites between fibres. The average number

of bonds in the model is 4970, corresponding to a bond density (bond number per unit area) of 78 μm^{-2}. In order to understand the effect of the inter-fibre bonds on the elastic modulus, bonds were randomly deleted and different numbers of residual bonds were obtained. Figure 7.11 shows that the elastic modulus of the model increases linearly with increasing bond density. The load transfer capability is reduced when the number of bonds decreases, which results in lower elastic modulus (Figure 7.12).

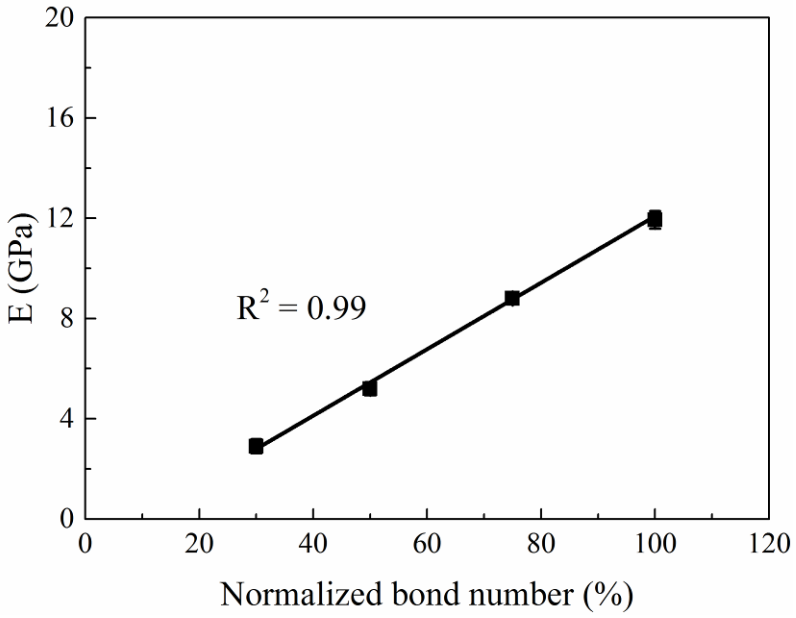

Figure 7.11 The elastic modulus of the model increases with the increasing bond density.

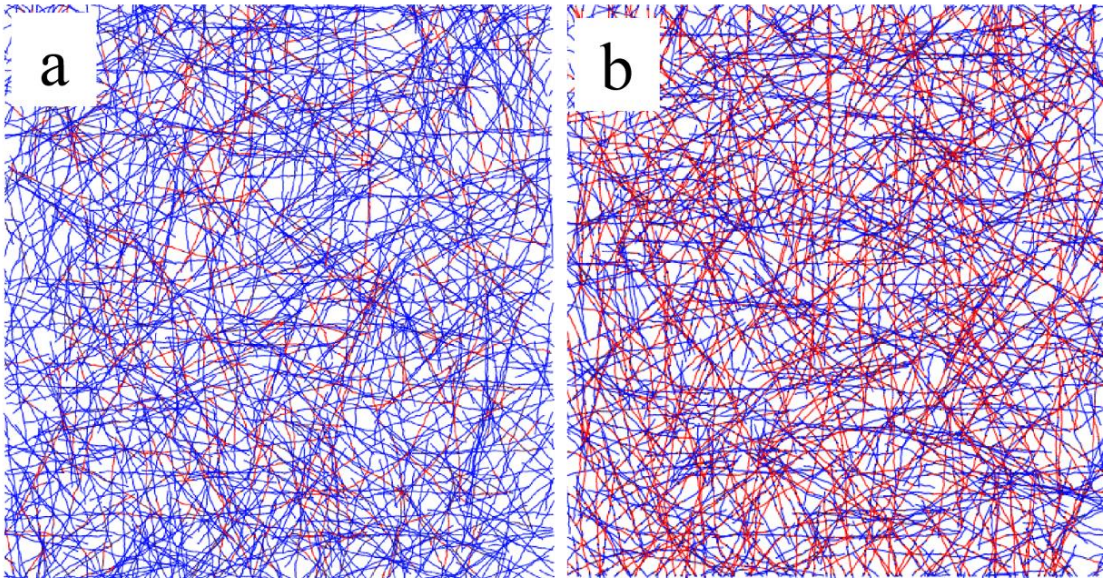

Figure 7.12 The stress state in models at a strain of 1 % with different bond densities: (a) 23 μm^{-2} and (b) 78 μm^{-2}. Blue colour represents low stress while other colours represent fibre fractions that carry load.

7.4 Conclusions

2D fibrous network models were used to simulate the elastic modulus of cellulose nanopaper and investigate the effect of fibre properties and microstructural parameters on the elastic modulus. The predicted elastic modulus of cellulose nanopaper was 12 GPa, which is consistent with experimental data in literature. Model predictions showed that the elastic modulus increased with fibre length due to the formation of more inter-fibre connections along each fibre. The elastic modulus also increased with decreasing fibre diameter due to the creation of a denser structure. Fibres that are initially straight showed a higher elastic since extended fibres facilitate efficient load transfer with more fibre segments effectively bearing the load. The elastic modulus of the model increases proportionally with the elastic modulus of the individual fibres. The microstructure of the cellulose nanopaper also influences the elastic modulus. It was found that the elastic

modulus increases linearly with the relative density of the model as well as inter-fibre bond density.

Chapter 8

Summary and future work

8.1 Summary

Cellulose nanopapers are fibrous networks made of cellulose nanofibres which connect with each other through hydrogen bonding at their intersections. These nanopapers show pronounced mechanical performance as well as unique physical properties. Numerous investigations have been carried out to exploit and/or take advantage of the mechanical properties of nanopapers but fundamental knowledge on the mechanics of nanopapers, including fracture mechanics and inelastic deformation mechanisms are still unclear. This thesis focuses on three aspects of the mechanical behaviour of cellulose nanopapers which are; a) the fracture properties of cellulose nanopapers; b) inelastic deformation mechanism of cellulose nanopapers; and c) structure-property relationships of cellulose nanopapers.

First, the fracture properties of cellulose nanopapers were investigated by performing double-edge-notch-tensile tests on samples with different notch lengths. It was found that the fracture strength of notched cellulose nanopapers was insensitive to the notch length. Then, the notched nanopapers were found to be able to partially relieve the stress concentrations at the notch tip. This phenomenon can be explained by a stress delocalization mechanism where diffused strain concentration zones were observed ahead

of the notch tip. Apart from experimental approaches, simulation methods were also used to study the fracture behaviour of notched cellulose nanopapers. The fracture energy of cellulose nanopaper derived from cohesive zone model is lower than that of ordinary printing paper due to the lack of energy consumed by fibre pull-out mechanism which is facilitated by high fibre lengths. By comparing the fracture process of notched nanopapers with different ligament lengths, it was found that longer ligaments facilitate progressive damage and stable crack propagation during straining.

In the second part of the thesis it was shown that cellulose nanopaper exhibits high tensile toughness not just because of its high strength but mainly due to its large inelastic deformation region which can be observed in the stress-strain curve. Therefore, in order to understand the toughening mechanisms of cellulose nanopaper it is necessary to investigate the mechanisms of inelasticity in these materials. In Chapter 5, the mechanisms of inelastic deformation in cellulose nanopaper were investigated at different hierarchical levels – from nanofibre slippage to molecular deformation. It was found that slippage between cellulose nanofibres is not the primary origin to inelastic deformation as revealed by repeated loading-unloading tests, in-situ Raman tests and 2D WAXD measurements. Instead, the results of rate-dependent tensile testing and temperature dependent dielectric measurements hinted that segmental motion in the cellulose chain in amorphous regions in the cellulose nanofibres is the prime cause for inelasticity, which is facilitated by the breakage of hydrogen bonds between chains.

Thirdly, the structure-property relationships of cellulose nanopapers were extensively studied. The effect of different preparation methods on mechanical properties of cellulose nanopapers was investigated. In most of the researches, thickness were used to calculate

the cross sectional area and hence the stress. However, it was shown that mechanical properties calculated based on film thickness did not reflect the true intrinsic load bearing potential of cellulose nanopapers since these materials exhibit a layered microstructure which includes non-load bearing inter-layer space. This inter-layer space will cause an underestimation of stress in the layers of cellulose nanopapers. In Chapter 6, cellulose nanopapers were prepared using different hot pressing strategies and a suspension casting method. Cellulose nanopaper prepared by a suspension casting method exhibited superior mechanical properties over hot pressed samples due to a lower porosity and its denser structure, which resulted in fewer defects and more fibre-fibre connections. This is speculated to be related to the slow evaporation process during which the capillary force drew the cellulose nanofibres closer together. Compared with SC sample, the water in the wet cake was quickly absorbed by the filter papers during hot pressing, leaving behind cellulose nanofibres that were less closely assembled. Hence, a looser structure with fewer hydrogen bonds was obtained than the SC sample after the wet cake was hot pressed to a nanopaper. The increasing hot compaction pressure leads to an increase in Young's modulus, yield stress and ultimate tensile strength due to the formation of a denser structure. Compaction temperature showed no significant influence on mechanical properties. Furthermore, a linear relationship was found between Young's modulus and porosity. In order to exclude the effect of inter-layer spacing on the stress, values of weight per unit surface area were used instead of film thickness in the calculation of cross-section area and stress, resulting in specific mechanical properties. The variation in specific mechanical properties among nanopapers prepared from different hot pressing strategies was smaller than in the properties based on film thickness indicating that the preparation methods primarily affected the inter-layer space between layers.

The structure-property relationship of cellulose nanopapers was also investigated using simulation methods. In Chapter 7, 2D fibrous network models were built to simulate the elastic modulus of cellulose nanopaper. An elastic modulus of 12 GPa was derived from the model, which is in good agreement with reported experimental data. Next, the influence of the parameters such as fibre length, diameter, waviness and elastic modulus, bonding density as well as the relative density of the model on the elastic modulus was investigated. From this it was concluded that a high elastic modulus can be achieved when the cellulose nanopaper is dense and made of long, thin, straight and strong fibres with a high inter-fibre bonding density.

8.2 Future work

8.2.1 Further studies on the fracture mechanics of cellulose nanopapers

Fracture toughness characterizes the ability of a notched sample to resist fracture. It is interesting to obtain the fracture toughness of cellulose nanopapers using linear elastic fracture mechanics (LEFM) theory. This can be achieved using large samples in order for the damage zone size to become insignificant compared to the characteristic length of the notched samples and deep notches to make sure that only one critical damage zone will propagate until ultimate failure. In this thesis, the notches were cut directly by a surgical scalpel and the notch tip radius were around 50 μm. From literature, it can be found that the value of fracture toughness depends on the sharpness of notch within a certain range of large notch tip radii and converges to a constant value when the notch tip is small enough [180]. Therefore, it is interesting to investigate the notch root radius dependency of fracture toughness. Similarly, the dependence of fracture toughness on length and width of the samples is also worth examining.

As a thin film, the possible failure of cellulose nanopapers can be induced by not only in-plane stretching but also tearing. Therefore, the fracture resistance of cellulose nanopapers under external force in the out-of-plane direction is worth investigating where a testing configuration called trouser tear testing could be useful [181].

8.2.2 Further studies on toughening mechanisms of cellulose nanopapers

In Chapter 5, potential inelastic deformation mechanism of cellulose nanopapers were suggested to be caused by segment motion in amorphous regions in cellulose nanofibres, which is facilitated by the breakage of hydrogen bonds between chains. To examine the conclusions of Chapter 5, tensile test on single cellulose nanofibres needs to be performed to elaborate on the inelastic deformation behaviour in individual nanofibres. The difficulty of performing this type of tests can be attributed to two aspects. First, the in-situ tensile testing has to be carried out in an SEM so that the nanofibres can be identified. The humidity in the SEM chamber needs be controlled and not of high vacuum as the loss of water will result in a brittle fracture mode of natural materials. Secondly, the testing rig should be sensitive enough to detect small forces since a single nanofibre is expect to break under low load.

8.2.3 Further studies on structure-property relationships of orientated cellulose nanopapers

The mechanical potential of cellulose nanofibres can be further exploited by preparing cellulose nanopapers with highly oriented nanofibres. Until now, the preparation of nanopapers with preferred orientation of nanofibres were mostly achieved by cold drawing cellulose wet cakes prior to drying. These wet cakes could only be drawn to a

low ratio (maximum 1.6) which resulted in a relatively low degree of orientation of the nanofibres. This is because the orientation of cellulose nanofibres has been generally determined during the formation of the wet cake when nanofibres have already entangled with each other. Therefore, in order to obtain nanopaper with highly oriented nanofibres, these fibres need to be aligned prior to the formation of wet cakes. Figure 8.1 shows a schematic of a rig which has the potential to align nanofibres during drying. First, a nanocellulose water suspension is fed into the rig from the top. Then, the roller spins rapidly generating high shear stresses between the bottom of the roller and the frame, forcing the nanofibres to align in the spinning direction. At the same time, elevated temperature from the roller facilitates the evaporation of water so that the orientation of the nanofibres could be maintained in the resulting dry nanopaper. The degree of orientation of nanofibres is expected to be controlled by tailoring the values of spinning velocity (v) and distance between roller and frame (d).

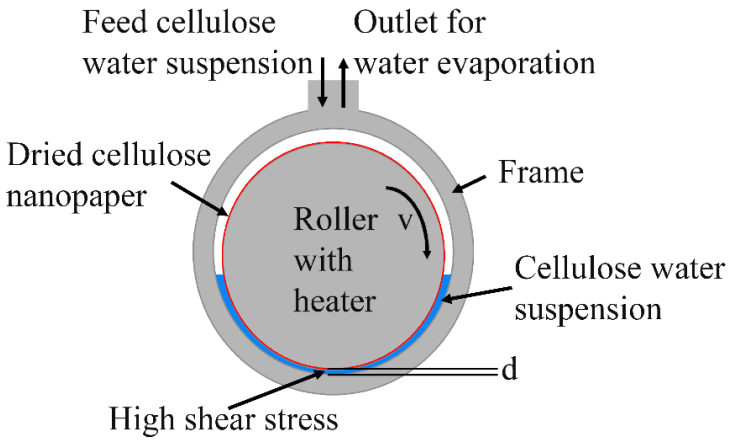

Figure 8.1 Schematic of a rig to produce cellulose nanopapers with a preferred orientation of nanofibres.

8.2.4 Further studies on the modelling of cellulose nanopaper

In the current thesis, only elastic properties of the cellulose nanopapers have been investigated. Future work should focus on the simulation of the whole stress-strain behaviour including inelastic behaviour.

The structure-property relationship of the fibrous networks can be further studied in terms of changing the orientation of the fibres. Moreover it might be of interest to build models having different number of layers and inter-layer spaces to identify the importance of this layered structure on mechanical properties.

References

1. D. Klemm, F. Kramer, S. Moritz, T. Lindstrom, M. Ankerfors, D. Gray, and A. Dorris, *Nanocelluloses: a new family of nature-based materials.* Angewandte Chemie-International Edition, 2011. **50**(24): p. 5438-5466.

2. J. Keckes, I. Burgert, K. Fruhmann, M. Muller, K. Kolln, M. Hamilton, M. Burghammer, S.V. Roth, S. Stanzl-Tschegg, and P. Fratzl, *Cell-wall recovery after irreversible deformation of wood.* Nature Materials, 2003. **2**(12): p. 810-814.

3. L.A. Berglund and T. Peijs, *Cellulose biocomposites — from bulk moldings to nanostructured systems.* MRS bulletin, 2010. **35**(03): p. 201-207.

4. M. Henriksson, L.A. Berglund, P. Isaksson, T. Lindstrom, and T. Nishino, *Cellulose nanopaper structures of high toughness.* Biomacromolecules, 2008. **9**(6): p. 1579-1585.

5. C. Aulin, M. Gällstedt, and T. Lindström, *Oxygen and oil barrier properties of microfibrillated cellulose films and coatings.* Cellulose, 2010. **17**(3): p. 559-574.

6. M. Nogi, S. Iwamoto, A.N. Nakagaito, and H. Yano, *Optically transparent nanofiber paper.* Advanced Materials, 2009. **21**(16): p. 1595-1598.

7. M.-C. Hsieh, C. Kim, M. Nogi, and K. Suganuma, *Electrically conductive lines on cellulose nanopaper for flexible electrical devices.* Nanoscale, 2013. **5**(19): p. 9289-9295.

8. K.L. Spence, R.A. Venditti, O.J. Rojas, Y. Habibi, and J.J. Pawlak, *The effect of chemical composition on microfibrillar cellulose films from wood pulps: water interactions and physical properties for packaging applications.* Cellulose, 2010. **17**(4): p. 835-848.

9. H. Yano, J. Sugiyama, A.N. Nakagaito, M. Nogi, T. Matsuura, M. Hikita, and K. Handa, *Optically transparent composites reinforced with networks of bacterial nanofibers.* Advanced Materials, 2005. **17**(2): p. 153-155.

10. A.J. Benítez, J. Torres-Rendon, M. Poutanen, and A. Walther, *Humidity and multiscale structure govern mechanical properties and deformation modes in films of native cellulose nanofibrils.* Biomacromolecules, 2013. **14**(12): p. 4497-4506.

11. H. Fukuzumi, T. Saito, and A. Isogai, *Influence of TEMPO-oxidized cellulose nanofibril length on film properties.* Carbohydrate Polymers, 2013. **93**(1): p. 172-177.

12. R. Ernest-Saunders, J.J. Pawlak, and J.M. Lee, *Properties of surface acetylated microfibrillated cellulose relative to intra-and inter-fibril bonding.* Cellulose, 2014. **21**(3): p. 1541-1552.

13. H. Sehaqui, Q. Zhou, O. Ikkala, and L.A. Berglund, *Strong and tough cellulose nanopaper with high specific surface area and porosity.* Biomacromolecules, 2011. **12**(10): p. 3638-3644.

14. M. Österberg, J. Vartiainen, J. Lucenius, U. Hippi, J. Seppälä, R. Serimaa, and J. Laine, *A fast method to produce strong NFC films as a platform for barrier and functional materials.* ACS Applied Materials & Interfaces, 2013. **5**(11): p. 4640-4647.

15. H. Sehaqui, A.D. Liu, Q. Zhou, and L.A. Berglund, *Fast preparation procedure for large, flat cellulose and cellulose/inorganic nanopaper structures.* Biomacromolecules, 2010. **11**(9): p. 2195-2198.

16. A.N. Nakagaito, A. Fujimura, T. Sakai, Y. Hama, and H. Yano, *Production of microfibrillated cellulose (MFC)-reinforced polylactic acid (PLA) nanocomposites from sheets obtained by a papermaking-like process.* Composites Science and Technology, 2009. **69**(7-8): p. 1293-1297.

17. J. Lu, T. Wang, and L.T. Drzal, *Preparation and properties of microfibrillated cellulose polyvinyl alcohol composite materials.* Composites: Part A, 2008. **39**(5): p. 738-746.

18. S.J. Eichhorn, A. Dufresne, M. Aranguren, N.E. Marcovich, J.R. Capadona, S.J. Rowan, C. Weder, W. Thielemans, M. Roman, S. Renneckar, W. Gindl, S. Veigel, J. Keckes, H. Yano, K. Abe, M. Nogi, A.N. Nakagaito, A. Mangalam, J. Simonsen, A.S. Benight, A. Bismarck, L.A. Berglund, and T. Peijs, *Review: current international research into cellulose nanofibres and nanocomposites.* Journal of Materials Science, 2010. **45**(1): p. 1-33.

19. D. Klemm, B. Heublein, H.P. Fink, and A. Bohn, *Cellulose: fascinating biopolymer and sustainable raw material.* Angewandte Chemie-International Edition, 2005. **44**(22): p. 3358-3393.

20. M.A.S.A. Samir, F. Alloin, and A. Dufresne, *Review of recent research into cellulosic whiskers, their properties and their application in nanocomposite field.* Biomacromolecules, 2005. **6**(2): p. 612-626.

21. N. Lavoine, I. Desloges, A. Dufresne, and J. Bras, *Microfibrillated cellulose — its barrier properties and applications in cellulosic materials: a review.* Carbohydrate Polymers, 2012. **90**(2): p. 735-764.

22. R.J. Moon, A. Martini, J. Nairn, J. Simonsen, and J. Youngblood, *Cellulose nanomaterials review: structure, properties and nanocomposites.* Chemical Society Reviews, 2011. **40**(7): p. 3941-3994.

23. A. Retegi, N. Gabilondo, C. Pena, R. Zuluaga, C. Castro, P. Ganan, K. de la Caba, and I. Mondragon, *Bacterial cellulose films with controlled microstructure-mechanical property relationships.* Cellulose, 2010. **17**(3): p. 661-669.

24. H. Yamamoto, F. Horii, and H. Odani, *Structural-changes of native cellulose crystals induced by annealing in aqueous alkaline and acidic solutions at high-temperatures.* Macromolecules, 1989. **22**(10): p. 4130-4132.

25. D.L. Vanderhart and R.H. Atalla, *Studies of microstructure in native celluloses using solid-state C-13 NMR.* Macromolecules, 1984. **17**(8): p. 1465-1472.

26. I. Sakurada, Y. Nukushina, and T. Ito, *Experimental determination of the elastic modulus of crystalline regions in oriented polymers.* Journal of Polymer Science, 1962. **57**(165): p. 651-660.

27. J.A. Bencomo-Cisneros, A. Tejeda-Ochoa, J.A. Garcia-Estrada, C.A. Herrera-Ramirez, A. Hurtado-Macias, R. Martinez-Sanchez, and J.M. Herrera-Ramirez, *Characterization of Kevlar-29 fibers by tensile tests and nanoindentation.* Journal of Alloys and Compounds, 2012. **536**: p. S456-S459.

28. S. Elazzouzi-Hafraoui, Y. Nishiyama, J.L. Putaux, L. Heux, F. Dubreuil, and C. Rochas, *The shape and size distribution of crystalline nanoparticles prepared by acid hydrolysis of native cellulose.* Biomacromolecules, 2008. **9**(1): p. 57-65.

29. X.Y. Tan, S.B.A. Hamid, and C.W. Lai, *Preparation of high crystallinity cellulose nanocrystals (CNCs) by ionic liquid solvolysis.* Biomass & Bioenergy, 2015. **81**: p. 584-591.

30. A. Isogai, T. Saito, and H. Fukuzumi, *TEMPO-oxidized cellulose nanofibers.* Nanoscale, 2011. **3**(1): p. 71-85.

31. M. Henriksson, G. Henriksson, L.A. Berglund, and T. Lindstrom, *An environmentally friendly method for enzyme-assisted preparation of microfibrillated cellulose (MFC) nanofibers.* European Polymer Journal, 2007. **43**(8): p. 3434-3441.

32. S.Y. Lee, S.J. Chun, I.A. Kang, and J.Y. Park, *Preparation of cellulose nanofibrils by high-pressure homogenizer and cellulose-based composite films.* Journal of Industrial and Engineering Chemistry, 2009. **15**(1): p. 50-55.

33. C. Tokoh, K. Takabe, M. Fujita, and H. Saiki, *Cellulose synthesized by Acetobacter xylinum in the presence of acetyl glucomannan.* Cellulose, 1998. **5**(4): p. 249-261.

34. N. Terinte, R. Ibbett, and K.C. Schuster, *Overview on native cellulose and microcrystalline cellulose I structure studied by X-ray diffraction (WAXD): comparison between measurement techniques.* Lenzinger Berichte, 2011. **89**: p. 118-131.

35. A. Hideno, K. Abe, H. Uchimura, and H. Yano, *Preparation by combined enzymatic and mechanical treatment and characterization of nanofibrillated cotton fibers.* Cellulose, 2016. **23**(6): p. 3639-3651.

36. K. Watanabe, M. Tabuchi, Y. Morinaga, and F. Yoshinaga, *Structural features and properties of bacterial cellulose produced in agitated culture.* Cellulose, 1998. **5**(3): p. 187-200.

37. H. Kargarzadeh, I. Ahmad, I. Abdullah, A. Dufresne, S.Y. Zainudin, and R.M. Sheltami, *Effects of hydrolysis conditions on the morphology, crystallinity, and thermal stability of cellulose nanocrystals extracted from kenaf bast fibers.* Cellulose, 2012. **19**(3): p. 855-866.

38. Y. Habibi, I. Hoeger, S.S. Kelley, and O.J. Rojas, *Development of Langmuir-Schaeffer cellulose nanocrystal monolayers and their interfacial behaviors.* Langmuir, 2010. **26**(2): p. 990-1001.

39. R.H. Atalla and D.L. Vanderhart, *Native cellulose — a composite of 2 distinct crystalline forms.* Science, 1984. **223**(4633): p. 283-285.

40. L. Kohler and H.C. Spatz, *Micromechanics of plant tissues beyond the linear-elastic range.* Planta, 2002. **215**(1): p. 33-40.

41. J. Barnett and V. Bonham, *Cellulose microfibril angle in the cell wall of wood fibres.* Biological Reviews, 2004. **79**(2): p. 461-472.

42. M.T. Postek, A. Vladar, J. Dagata, N. Farkas, B. Ming, R. Wagner, A. Raman, R.J. Moon, R. Sabo, T.H. Wegner, and J. Beecher, *Development of the metrology and imaging of cellulose nanocrystals.* Measurement Science & Technology, 2011. **22**(2): p. 1-10.

43. D. Fengel, *Ideas on the ultrastructural organization of the cell wall components.* Journal of Polymer Science: Part C, 1971. **36**(1): p. 383-392.

44. C.J. Biermann, *Handbook of pulping and papermaking*. 1996: Academic press.

45. S.F. Turbak AF, Sandberg KR, *Microfibrillated cellulose, a new cellulose product: properties, uses, and commercial potential*, in *J Appl Polym Sci: Appl Polym Symp*. 1983. p. 815–827.

46. C.R. Herrick FW, Hamilton JK, Sandberg KR, *Microfibrillated cellulose: morphology and accessibility*, in *J Appl Polym Sci: Appl Polym Symp*. 1983. p. 797–813.

47. T. Taniguchi and K. Okamura, *New films produced from microfibrillated natural fibres.* Polymer International, 1998. **47**(3): p. 291-294.

48. B. Wang and M. Sain, *Dispersion of soybean stock-based nanofiber in a plastic matrix.* Polymer International, 2007. **56**(4): p. 538-546.

49. S.Q. Wang and Q.Z. Cheng, *A novel process to isolate fibrils from cellulose fibers by high-intensity ultrasonication, part 1: process optimization.* Journal of Applied Polymer Science, 2009. **113**(2): p. 1270-1275.

50. A. Dufresne, *Nanocellulose: from nature to high performance tailored materials*. 2012: Walter de Gruyter.

51. Y.H.P. Zhang, M.E. Himmel, and J.R. Mielenz, *Outlook for cellulase improvement: screening and selection strategies.* Biotechnology Advances, 2006. **24**(5): p. 452-481.

52. T. Saito, Y. Nishiyama, J.L. Putaux, M. Vignon, and A. Isogai, *Homogeneous suspensions of individualized microfibrils from TEMPO-catalyzed oxidation of native cellulose.* Biomacromolecules, 2006. **7**(6): p. 1687-1691.

53. T. Saito, S. Kimura, Y. Nishiyama, and A. Isogai, *Cellulose nanofibers prepared by TEMPO-mediated oxidation of native cellulose.* Biomacromolecules, 2007. **8**(8): p. 2485-2491.

54. R. Shinoda, T. Saito, Y. Okita, and A. Isogai, *Relationship between length and degree of polymerization of TEMPO-oxidized cellulose nanofibrils.* Biomacromolecules, 2012. **13**(3): p. 842-849.

55. T. Saito, M. Hirota, N. Tamura, S. Kimura, H. Fukuzumi, L. Heux, and A. Isogai, *Individualization of nano-sized plant cellulose fibrils by direct surface carboxylation using TEMPO catalyst under neutral conditions.* Biomacromolecules, 2009. **10**(7): p. 1992-1996.

56. L. Wagberg, G. Decher, M. Norgren, T. Lindstrom, M. Ankerfors, and K. Axnas, *The build-up of polyelectrolyte multilayers of microfibrillated cellulose and cationic polyelectrolytes.* Langmuir, 2008. **24**(3): p. 784-795.

57. S. Tanpichai, F. Quero, M. Nogi, H. Yano, R.J. Young, T. Lindstrom, W.W. Sampson, and S.J. Eichhorn, *Effective Young's modulus of bacterial and microfibrillated cellulose fibrils in fibrous networks.* Biomacromolecules, 2012. **13**(5): p. 1340-1349.

58. T. Saito, R. Kuramae, J. Wohlert, L.A. Berglund, and A. Isogai, *An ultrastrong nanofibrillar biomaterial: the strength of single cellulose nanofibrils revealed via sonication-induced fragmentation.* Biomacromolecules, 2013. **14**(1): p. 248-253.

59. A.N. Nakagaito and H. Yano, *The effect of fiber content on the mechanical and thermal expansion properties of biocomposites based on microfibrillated cellulose.* Cellulose, 2008. **15**(4): p. 555-559.

60. M. Henriksson and L.A. Berglund, *Structure and properties of cellulose nanocomposite films containing melamine formaldehyde.* Journal of Applied Polymer Science, 2007. **106**(4): p. 2817-2824.

61. B. Wang and M. Sain, *Isolation of nanofibers from soybean source and their reinforcing capability on synthetic polymers.* Composites Science and Technology, 2007. **67**(11-12): p. 2521-2527.

62. A. Dufresne, D. Dupeyre, and M.R. Vignon, *Cellulose microfibrils from potato tuber cells: processing and characterization of starch-cellulose microfibril composites.* Journal of Applied Polymer Science, 2000. **76**(14): p. 2080-2092.

63. A. Iwatake, M. Nogi, and H. Yano, *Cellulose nanofiber-reinforced polylactic acid.* Composites Science and Technology, 2008. **68**(9): p. 2103-2106.

64. A.J. Brown, *XLIII. — On an acetic ferment which forms cellulose.* Journal of the Chemical Society, Transactions, 1886. **49**: p. 432-439.

65. K. Zaar, *Biogenesis of cellulose by Acetobacter xylinum.* Cytobiologie, 1977. **16**(1): p. 1-15.

66. S. Yamanaka, M. Ishihara, and J. Sugiyama, *Structural modification of bacterial cellulose.* Cellulose, 2000. **7**(3): p. 213-225.

67. M.E. Embuscado, J.N. BeMiller, and J.S. Marks, *Isolation and partial characterization of cellulose produced by Acetobacter xylinum.* Food Hydrocolloids, 1996. **10**(1): p. 75-82.

68. S. Gea, C.T. Reynolds, N. Roohpour, B. Wirjosentono, N. Soykeabkaew, E. Bilotti, and T. Peijs, *Investigation into the structural, morphological, mechanical and thermal behaviour of bacterial cellulose after a two-step purification process.* Bioresource Technology, 2011. **102**(19): p. 9105-9110.

69. G. Guhados, W.K. Wan, and J.L. Hutter, *Measurement of the elastic modulus of single bacterial cellulose fibers using atomic force microscopy.* Langmuir, 2005. **21**(14): p. 6642-6646.

70. N. Heßler and D. Klemm, *Alteration of bacterial nanocellulose structure by in situ modification using polyethylene glycol and carbohydrate additives.* Cellulose, 2009. **16**(5): p. 899-910.

71. P. Gatenholm and D. Klemm, *Bacterial nanocellulose as a renewable material for biomedical applications.* MRS Bulletin, 2010. **35**(3): p. 208-213.

72. H. Sehaqui, N. Ezekiel Mushi, S. Morimune, M. Salajkova, T. Nishino, and L.A. Berglund, *Cellulose nanofiber orientation in nanopaper and nanocomposites by cold drawing.* ACS Applied Materials & Interfaces, 2012. **4**(2): p. 1043-1049.

73. H. Sehaqui, S. Morimune, T. Nishino, and L.A. Berglund, *Stretchable and strong cellulose nanopaper structures based on polymer — coated nanofiber networks: an alternative to nonwoven porous membranes from electrospinning.* Biomacromolecules, 2012. **13**(11): p. 3661-3667.

74. K.-Y. Lee, H. Qian, F.H. Tay, J.J. Blaker, S.G. Kazarian, and A. Bismarck, *Bacterial cellulose as source for activated nanosized carbon for electric double layer capacitors.* Journal of Materials Science, 2013. **48**(1): p. 367-376.

75. M. Iguchi, S. Yamanaka, and A. Budhiono, *Bacterial cellulose — a masterpiece of nature's arts.* Journal of Materials Science, 2000. **35**(2): p. 261-270.

76. K. Syverud and P. Stenius, *Strength and barrier properties of MFC films.* Cellulose, 2009. **16**(1): p. 75-85.

77. J. Huang, H.L. Zhu, Y.C. Chen, C. Preston, K. Rohrbach, J. Cumings, and L.B. Hu, *Highly transparent and flexible nanopaper transistors.* ACS Nano, 2013. **7**(3): p. 2106-2113.

78. H.L. Zhu, S.Z. Zhu, Z. Jia, S. Parvinian, Y.Y. Li, O. Vaaland, L.B. Hu, and T. Li, *Anomalous scaling law of strength and toughness of cellulose nanopaper.* Proceedings of the National Academy of Sciences of the United States of America, 2015. **112**(29): p. 8971-8976.

79. K. Abe and H. Yano, *Comparison of the characteristics of cellulose microfibril aggregates of wood, rice straw and potato tuber.* Cellulose, 2009. **16**(6): p. 1017-1023.

80. H. Fukuzumi, T. Saito, T. Wata, Y. Kumamoto, and A. Isogai, *Transparent and high gas barrier films of cellulose nanofibers prepared by TEMPO-mediated oxidation.* Biomacromolecules, 2009. **10**(1): p. 162-165.

81. M.E. Launey and R.O. Ritchie, *On the fracture toughness of advanced materials.* Advanced Materials, 2009. **21**(20): p. 2103-2110.

82. R.O. Ritchie, *Mechanisms of fatigue-crack propagation in ductile and brittle solids.* International Journal of Fracture, 1999. **100**(1): p. 55-83.

83. R.O. Ritchie, *Mechanisms of fatigue crack-propagation in metals, ceramics and composites — role of crack tip shielding.* Materials Science and Engineering: A 1988. **103**(1): p. 15-28.

84. H.W. Haslach Jr, *The moisture and rate-dependent mechanical properties of paper: a review.* Mechanics of Time-Dependent Materials, 2000. **4**(3): p. 169-210.

85. N.L. Salmén, *Paper: structure and properties*. Vol. The cell wall as a composite structure. 1986, New York: Marcel Dekker.

86. Y.C. Hsieh, H. Yano, M. Nogi, and S.J. Eichhorn, *An estimation of the Young's modulus of bacterial cellulose filaments.* Cellulose, 2008. **15**(4): p. 507-513.

87. C.T. Koh, D. Strange, K. Tonsomboon, and M. Oyen, *Failure mechanisms in fibrous scaffolds.* Acta Biomaterialia, 2013. **9**(7): p. 7326-7334.

88. A. Ridruejo, R. Jubera, C. Gonzalez, and J. LLorca, *Inverse notch sensitivity: cracks can make nonwoven fabrics stronger.* Journal of the Mechanics and Physics of Solids, 2015. **77**: p. 61-69.

89. P. Isaksson and R. Hägglund, *Strain energy distribution in a crack-tip region in random fiber networks.* International Journal of Fracture, 2009. **156**(1): p. 1-9.

90. U. Stachewicz, I. Peker, W. Tu, and A.H. Barber, *Stress delocalization in crack tolerant electrospun nanofiber networks.* ACS Applied Materials & Interfaces, 2011. **3**(6): p. 1991-1996.

91. J. Li, *Investigation of the fracture resistance of paper utilizing a modified linear elastic elastic fracture mechanics model*. 2015, Miami University.

92. A. Hagman and M. Nygårds, *Investigation of sample-size effects on in-plane tensile testing of paperboard.* Nordic Pulp & Paper Research Journal, 2012. **27**(2): p. 295-304.

93. P. Makela, *On the fracture mechanics of paper.* Nordic Pulp & Paper Research Journal, 2002. **17**(3): p. 254-274.

94. T.L. Anderson and T. Anderson, *Fracture mechanics: fundamentals and applications*. 2005: CRC press.

95. M. Janssen, J Zuidema, and R. J. H Wanhill, *Fracture mechanics*. 2nd ed. 2004, London: Spon Press.

96. R. Seth, A. Robertson, M. YIU-WING, and J. Hoffmann, *Plane stress fracture toughness of paper.* TAPPI Journal, 1993. **76**(2): p. 109-116.

97. T. Bárány, T. Czigány, and J. Karger-Kocsis, *Application of the essential work of fracture (EWF) concept for polymers, related blends and composites: a review.* Progress in Polymer Science, 2010. **35**(10): p. 1257-1287.

98. R.S. Seth, *Measurement of in-plane fracture toughness of paper.* 1996 Papermakers Conference, 1996: p. 395-402.

99. W.S.-C. Mai Y-W, Chen X-H., *Polymer blends: formulations and performance*. Vol. 2. 2000, New York: Wiley.

100. B.F. Sorensen, S. Goutianos, and T.K. Jacobsen, *Strength scaling of adhesive joints in polymer-matrix composites.* International Journal of Solids and Structures, 2009. **46**(3-4): p. 741-761.

101. S. Morel, C. Lespine, J.L. Coureau, J. Planas, and N. Dourado, *Bilinear softening parameters and equivalent LEFM R-curve in quasibrittle failure.* International Journal of Solids and Structures, 2010. **47**(6): p. 837-850.

102. S. Li, M.D. Thouless, A.M. Waas, J.A. Schroeder, and P.D. Zavattieri, *Use of a cohesive-zone model to analyze the fracture of a fiber-reinforced polymer-matrix composite.* Composites Science and Technology, 2005. **65**(3-4): p. 537-549.

103. B.F. Sorensen and T.K. Jacobsen, *Determination of cohesive laws by the J integral approach.* Engineering Fracture Mechanics, 2003. **70**(14): p. 1841-1858.

104. S. Goutianos and B.F. Sørensen, *The application of J integral to measure cohesive laws under large-scale yielding.* Engineering Fracture Mechanics, 2016. **155**: p. 145–165.

105. R. Seth and D. Page, *Fracture resistance of paper.* Journal of Materials Science, 1974. **9**(11): p. 1745-1753.

106. J.A.a.L. Begley, J. D., *in "Fracture toughness", ASTM STP 514*. 1972, American Society for Testing and Materials: Philadelphia. p. 1-20.

107. T. Yuhara and M.T. Kortschot, *A simplified determination of the J-Integral for paper.* Journal of Materials Science, 1993. **28**(13): p. 3571-3580.

108. B. Westerlind, L. Carlsson, and Y. Andersson, *Fracture toughness of liner board evaluated by the J-integral.* Journal of Materials Science, 1991. **26**(10): p. 2630-2636.

109. D.M.S. Wanigaratne, W.J. Batchelor, and I.H. Parker, *Comparison of fracture toughness of paper with tensile properties.* 55th Appita Annual Conference, Proceedings, 2001: p. 229-235.

110. A. Tanaka and T. Yamauchi, *Deformation and fracture of paper during the in-plane fracture toughness testing — examination of the essential work of fracture method.* Journal of Materials Science, 2000. **35**(7): p. 1827-1833.

111. Y.Z. Yu and P. Karenlampi, *On crack stability in paper toughness testing.* Journal of Materials Science, 1997. **32**(24): p. 6513-6517.

112. S. Östlund, K. Niskanen, and P. Kärenlampi, *On the prediction of the strength of paper structures with a flaw.* Journal of Pulp and Paper Science, 1999. **25**(10): p. 356-360.

113. P. Makela and S. Ostlund, *Cohesive crack modelling of thin sheet material exhibiting anisotropy, plasticity and large-scale damage evolution.* Engineering Fracture Mechanics, 2012. **79**: p. 50-60.

114. J. Zechner, M. Janko, and O. Kolednik, *Determining the fracture resistance of thin sheet fiber composites — paper as a model material.* Composites Science and Technology, 2013. **74**: p. 43-51.

115. S. Goutianos, R. Arevalo, B.F. Sorensen, and T. Peijs, *Effect of processing conditions on fracture resistance and cohesive laws of binderfree all-cellulose composites.* Applied Composite Materials, 2014. **21**(6): p. 805-825.

116. X.-F. Wu and Y.A. Dzenis, *Elasticity of planar fiber networks.* Journal of Applied Physics, 2005. **98**(9): p. 093501.

117. M. Ramasubramanian and Y. Wang, *A computational micromechanics constitutive model for the unloading behavior of paper.* International Journal of Solids and Structures, 2007. **44**(22): p. 7615-7632.

118. P. Isaksson, *An implicit stress gradient plasticity model for describing mechanical behavior of planar fiber networks on a macroscopic scale.* Engineering Fracture Mechanics, 2010. **77**(8): p. 1240-1252.

119. P. Isaksson and R. Hägglund, *Structural effects on deformation and fracture of random fiber networks and consequences on continuum models.* International Journal of Solids and Structures, 2009. **46**(11): p. 2320-2329.

120. C.T. Koh and M.L. Oyen, *Branching toughens fibrous networks.* Journal of the Mechanical Behavior of Biomedical Materials, 2012. **12**: p. 74-82.

121. C.A. Bronkhorst, *Modelling paper as a two-dimensional elastic-plastic stochastic network.* International Journal of Solids and Structures, 2003. **40**(20): p. 5441-5454.

122. R. Haegglund and P. Isaksson, *On the coupling between macroscopic material degradation and interfiber bond fracture in an idealized fiber network.* International Journal of Solids and Structures, 2008. **45**(3-4): p. 868-878.

123. S. Heyden and P.J. Gustafsson, *Simulation of fracture in a cellulose fibre network.* Journal of Pulp and Paper Science, 1998. **24**(5): p. 160-165.

124. Y. Lee and I. Jasiuk, *Apparent elastic properties of random fiber networks.* Computational Materials Science, 2013. **79**: p. 715-723.

125. A. Kulachenko and T. Uesaka, *Direct simulations of fiber network deformation and failure.* Mechanics of Materials, 2012. **51**: p. 1-14.

126. A. Kulachenko, T. Denoyelle, S. Galland, and S.B. Lindström, *Elastic properties of cellulose nanopaper.* Cellulose, 2012. **19**(3): p. 793-807.

127. E.T. Thostenson, Z. Ren, and T.-W. Chou, *Advances in the science and technology of carbon nanotubes and their composites: a review.* Composites science and technology, 2001. **61**(13): p. 1899-1912.

128. V.P. Veedu, D. Askari, and M.N. Ghasemi-Nejhad, *Chirality dependence of carbon single-walled nanotube material properties: Axial Young's modulus.* Journal of Nanoscience and Nanotechnology, 2006. **6**(7): p. 2159-2166.

129. M. Scarselli, P. Castrucci, and M. De Crescenzi, *Electronic and optoelectronic nano-devices based on carbon nanotubes.* Journal of Physics: Condensed Matter, 2012. **24**(31): p. 313202.

130. S. Cui, I.A. Kinloch, R.J. Young, L. Noé, and M. Monthioux, *The effect of stress transfer within double‐walled carbon nanotubes upon their ability to reinforce composites.* Advanced Materials, 2009. **21**(35): p. 3591-3595.

131. E.W. Wong, P.E. Sheehan, and C.M. Lieber, *Nanobeam mechanics: elasticity, strength, and toughness of nanorods and nanotubes.* Science, 1997. **277**(5334): p. 1971-1975.

132. J.-P. Salvetat, A.J. Kulik, J.-M. Bonard, G.A.D. Briggs, T. Stöckli, K. Méténier, S. Bonnamy, F. Béguin, N.A. Burnham, and L. Forró, *Elastic modulus of ordered and disordered multiwalled carbon nanotubes.* Advanced Materials, 1999. **11**(2): p. 161-165.

133. J.-P. Salvetat, G.A.D. Briggs, J.-M. Bonard, R.R. Bacsa, A.J. Kulik, T. Stöckli, N.A. Burnham, and L. Forró, *Elastic and shear moduli of single-walled carbon nanotube ropes.* Physical Review Letters, 1999. **82**(5): p. 944-947.

134. M.-F. Yu, O. Lourie, M.J. Dyer, K. Moloni, T.F. Kelly, and R.S. Ruoff, *Strength and breaking mechanism of multiwalled carbon nanotubes under tensile load.* Science, 2000. **287**(5453): p. 637-640.

135. M.-F. Yu, B.S. Files, S. Arepalli, and R.S. Ruoff, *Tensile loading of ropes of single wall carbon nanotubes and their mechanical properties.* Physical Review Letters, 2000. **84**(24): p. 5552-5555.

136. W. Ma, L. Song, R. Yang, T. Zhang, Y. Zhao, L. Sun, Y. Ren, D. Liu, L. Liu, and J. Shen, *Directly synthesized strong, highly conducting, transparent single-walled carbon nanotube films.* Nano Letters, 2007. **7**(8): p. 2307-2311.

137. R. Duggal, F. Hussain, and M. Pasquali, *Self‐assembly of single‐walled carbon nanotubes into a sheet by drop drying.* Advanced Materials, 2006. **18**(1): p. 29-34.

138. Q. Liu, T. Fujigaya, H.-M. Cheng, and N. Nakashima, *Free-standing highly conductive transparent ultrathin single-walled carbon nanotube films.* Journal of the American Chemical Society, 2010. **132**(46): p. 16581-16586.

139. X. Zhang, *Hydroentangling: a novel approach to high‐speed fabrication of carbon nanotube membranes.* Advanced Materials, 2008. **20**(21): p. 4140-4144.

140. H.W. Zhu and B.Q. Wei, *Assembly and applications of carbon nanotube thin films.* Journal of Materials Science & Technology, 2008. **24**(4): p. 447-456.

141. J.W. Zhang, D.Z. Jiang, and H.X. Peng, *A pressurized filtration technique for fabricating carbon nanotube buckypaper: structure, mechanical and conductive properties.* Microporous and Mesoporous Materials, 2014. **184**: p. 127-133.

142. J.H. Han, H. Zhang, M.J. Chen, G.R. Wang, and Z. Zhang, *CNT buckypaper/thermoplastic polyurethane composites with enhanced stiffness, strength and toughness.* Composites Science and Technology, 2014. **103**: p. 63-71.

143. P.G. Whitten, G.M. Spinks, and G.G. Wallace, *Mechanical properties of carbon nanotube paper in ionic liquid and aqueous electrolytes.* Carbon, 2005. **43**(9): p. 1891-1896.

144. J.G. Park, J. Smithyman, C.Y. Lin, A. Cooke, A.W. Kismarahardja, S. Li, R. Liang, J.S. Brooks, C. Zhang, and B. Wang, *Effects of surfactants and alignment*

on the physical properties of single-walled carbon nanotube buckypaper. Journal of Applied Physics, 2009. **106**(10): p. 104310.

145. S.M. Zendehbad and G. Yang, *Analysis of bacterial cellulose/ionic liquid MWCNTs via cyclic voltammetry.* Advances in Chemical Engineering and Science, 2016. **6**(01): p. 34-42.

146. E. Skrzetuska, M. Puchalski, and I. Krucińska, *Chemically driven printed textile sensors based on graphene and carbon nanotubes.* Sensors, 2014. **14**(9): p. 16816-16828.

147. J. Blaber, B. Adair, and A. Antoniou, *Ncorr: open-source 2D digital image correlation matlab software.* Experimental Mechanics, 2015. **55**(6): p. 1105-1122.

148. S. Park, J.O. Baker, M.E. Himmel, P.A. Parilla, and D.K. Johnson, *Cellulose crystallinity index: measurement techniques and their impact on interpreting cellulase performance.* Biotechnology for Biofuels, 2010. **3**(1): p. 1-10.

149. P. Bhupathi, L. Jaworski, J. Hwang, D. Tanner, S. Obukhov, Y. Lee, and N. Mulders, *Optical birefringence in uniaxially compressed aerogels.* New Journal of Physics, 2010. **12**(10): p. 103016.

150. B.M.a.W. E, *Principles of optics*. 7th ed. 1999, Cambridge: Cambridge University Press.

151. A. Tanaka and T. Yamauchi, *Examination of the essential work of fracture method for paper.* Tappi International Paper Physics Conference, 1999: p. 171-177.

152. Abaqus version 6.11, Abaqus Inc, 2012.

153. V. Mollon, J. Bonhomme, A.M. Elmarakbi, A. Arguelles, and J. Vina, *Finite element modelling of mode I delamination specimens by means of implicit and explicit solvers.* Polymer Testing, 2012. **31**(3): p. 404-410.

154. Z. Suo, S. Ho, and X. Gong, *Notch ductile-to-brittle transition due to localized inelastic band.* Journal of Engineering Materials and Technology-Transactions of the Asme, 1993. **115**(3): p. 319-326.

155. B.F. Sorensen, *Cohesive law and notch sensitivity of adhesive joints.* Acta Materialia, 2002. **50**(5): p. 1053-1061.

156. N. Gierlinger, M. Schwanninger, A. Reinecke, and I. Burgert, *Molecular changes during tensile deformation of single wood fibers followed by Raman microscopy.* Biomacromolecules, 2006. **7**(7): p. 2077-2081.

157. J.H. Wiley and R.H. Atalla, *Band assignments in the Raman spectra of celluloses.* Carbohydrate Research, 1987. **160**: p. 113-129.

158. F. Quero, M. Nogi, H. Yano, K. Abdulsalami, S.M. Holmes, B.H. Sakakini, and S.J. Eichhorn, *Optimization of the mechanical performance of bacterial cellulose/poly (l-lactic) acid composites.* ACS Applied Materials & Interfaces, 2009. **2**(1): p. 321-330.

159. S. Eichhorn, J. Sirichaisit, and R. Young, *Deformation mechanisms in cellulose fibres, paper and wood.* Journal of Materials Science, 2001. **36**(13): p. 3129-3135.

160. S. Eichhorn, R. Young, and W.-Y. Yeh, *Deformation processes in regenerated cellulose fibers.* Textile Research Journal, 2001. **71**(2): p. 121-129.

161. S.J. Eichhorn, R.J. Young, and G.R. Davies, *Modeling crystal and molecular deformation in regenerated cellulose fibers.* Biomacromolecules, 2005. **6**(1): p. 507-513.

162. A. Mulliken and M. Boyce, *Mechanics of the rate-dependent elastic–plastic deformation of glassy polymers from low to high strain rates.* International Journal of Solids and Structures, 2006. **43**(5): p. 1331-1356.

163. M. Kanters, *Prediction of long-term performance of load-bearing thermoplastics*. 2015, Technische Universiteit Eindhoven.

164. T.A. Engels, S.H. Söntjens, T.H. Smit, and L.E. Govaert, *Time-dependent failure of amorphous polylactides in static loading conditions.* Journal of Materials Science, 2010. **21**(1): p. 89-97.

165. I.M. Ward and J. Sweeney, *Mechanical properties of solid polymers*. 2012: John Wiley & Sons.

166. T.B. Van Erp, C.T. Reynolds, T. Peijs, J.A.W. Van Dommelen, and L.E. Govaert, *Prediction of yield and long-term failure of oriented polypropylene: kinetics and anisotropy.* Journal of Polymer Science: Part B, 2009. **47**(20): p. 2026-2035.

167. C. Chaléat, G. Michel-Amadry, P. Halley, and R. Truss, *Properties of a plasticised starch blend — part 2: influence of strain rate, temperature and*

moisture on the tensile yield behaviour. Carbohydrate Polymers, 2008. **74**(3): p. 366-371.

168. J.Y. Lim, H.J. Donahue, and S.Y. Kim, *Strain rate, temperature, and microstructure-dependent yield stress of poly(ethylene terephthalate).* Macromolecular Chemistry and Physics, 2003. **204**(4): p. 653-660.

169. H.B. Bohidar, *Fundamentals of polymer physics and molecular biophysics*. 2015: Cambridge University Press.

170. S.J. Blanksby and G.B. Ellison, *Bond dissociation energies of organic molecules.* Accounts of Chemical Research, 2003. **36**(4): p. 255-263.

171. A. Rachocki, E. Markiewicz, and J. Tritt-Goc, *Dielectric relaxation in cellulose and its derivatives.* Acta Physica Polonica A, 2005. **108**: p. 137-145.

172. G. Jafarpour, E. Dantras, A. Boudet, and C. Lacabanne, *Study of dielectric relaxations in cellulose by combined DDS and TSC.* Journal of Non-Crystalline Solids, 2007. **353**(44): p. 4108-4115.

173. F. Roig, E. Dantras, J. Dandurand, and C. Lacabanne, *Influence of hydrogen bonds on glass transition and dielectric relaxations of cellulose.* Journal of Physics D: Applied Physics, 2011. **44**(4): p. 045403.

174. A.S. Virk, W. Hall, and J. Summerscales, *Modulus and strength prediction for natural fibre composites.* Materials Science and Technology, 2012. **28**(7): p. 864-871.

175. R. Arévalo and T. Peijs, *Binderless all-cellulose fibreboard from microfibrillated lignocellulosic natural fibres.* Composites: Part A, 2016. **83**: p. 38-46.

176. F. Bobaru, *Influence of van der Waals forces on increasing the strength and toughness in dynamic fracture of nanofibre networks: a peridynamic approach.* Modelling and Simulation in Materials Science and Engineering, 2007. **15**(5): p. 397-417.

177. H. Cox, *The elasticity and strength of paper and other fibrous materials.* British Journal of Applied Physics, 1952. **3**(3): p. 72.

178. A. Šturcová, G.R. Davies, and S.J. Eichhorn, *Elastic modulus and stress-transfer properties of tunicate cellulose whiskers.* Biomacromolecules, 2005. **6**(2): p. 1055-1061.

179. J. Summerscales, W. Hall, and A.S. Virk, *A fibre diameter distribution factor (FDDF) for natural fibre composites.* Journal of Materials Science, 2011. **46**(17): p. 5876-5880.

180. K.Y. Volokh and P. Trapper, *Fracture toughness from the standpoint of softening hyperelasticity.* Journal of the Mechanics and Physics of Solids, 2008. **56**(7): p. 2459-2472.

181. A.C. Chang, T. Inge, L. Tau, A. Hiltner, and E. Baer, *Tear strength of ductile polyolefin films.* Polymer Engineering and Science, 2002. **42**(11): p. 2202-2212.

List of publications

R. Mao, S. Goutianos, W. Tu, G. Yang, L.A. Berglund, T. Peijs, *Fracture properties of cellulose nanopaper*, To be submitted.

R. Mao, N. Meng, W. Tu, L.A. Berglund, T. Peijs, *Toughening mechanism in cellulose nanopaper*, To be submitted.

R. Mao, S. Goutianos, W. Tu, G. Yang, L.A. Berglund, T. Peijs, *Modelling the elastic properties of nanocellulose fibrous networks*, To be submitted.

N. Meng, R. Mao, W. Tu, X. Zhu, R.M. Wilson, E. Billoti, M.J. Reece, *Processing and characterization of freestanding highly oriented ferroelectric polymer films with remarkably low coercive field and high remnant polarization*. Polymer, 2016. **100**: p. 69-76.

M. Gai, J. Frueh, V.L. Kudryavtseva, R. Mao, M.V. Kiryukhin, G.B. Sukhorukov, *Patterned microstructure fabrication: polyelectrolyte complexes vs polyelectrolyte multilayers*, Scientific Reports, 2016. **6**: p. 37000.